INDUCTION MOTOR CURRENT SIGNATURE ANALYSIS FOR SPEED DETECTION USING SPECTRAL ESTIMATION TECHNIQUES

by

Manjinder Singh Gill

Submitted
in partial fulfillment of the requirements
for the degree of

MASTER OF APPLIED SCIENCE

Major Subject: Electrical and Computer Engineering

at

DALHOUSIE UNIVERSITY

Halifax, Nova Scotia November, 2005

DALHOUSIE UNIVERSITY

To comply with the Canadian Privacy Act the National Library of Canada has requested that the following pages be removed from this copy of the thesis:

Preliminary Pages
- Examiners Signature Page
- Dalhousie Library Copyright Agreement

Appendices
- Copyright Releases (if applicable)

Dedication

To my wife Raman Gill and
daughter Nimrat Gill
for their immense moral support

Table of Contents

List of Tables

List of Figures

List of Abbreviations

ADC: Analog-to-Digital Converter

AR: Auto-Regressive

ARMA: Auto-Regressive and Moving Average

CBM: Condition-Based Monitoring

Ch: Channel

COM: Common

CSD: Cone-Shaped Distribution

DAQ: Data Acquisition

DFT: Discrete Fourier Transform

FFT: Fast Fourier Transform

FHP: Fractional Horse Power

GUI: Graphical User Interface

Hz: Hertz

JTFA: Joint Time-Frequency Analysis

kHz: Kilo Hertz

MCSA: Motor Current Signature Analysis

MMF: Magneto-Motive Force

MP: Matrix-Pencil

MUSIC: Multiple Signal Classifiers

NI: National Instruments

N-m: Newton Meter

PCAR: Principle Component Auto-Regressive

RCA: Root-Cause Analysis

rpm: Revolution per Minute

RSH: Rotor Slot Harmonics

SRSA: Super Resolution Spectral Analysis

STFT: Short-Time Fourier Transform

SVD: Singular Value Decomposition

USB: Universal Serial Bus

WVD: Wigner-Ville Distribution

Acknowledgements

I am thankful to Dr. Timothy Little for his valuable guidance and to the advisory committee members Dr. M.E. El-Hawary and Dr. William J. Phillips. I would also like to thank my parents and in-laws for their support and encouragement.

Abstract

In this research work, real-time performance of various spectral estimation techniques have been investigated to detect speed of an induction motor from rotor slot harmonics using motor current signature analysis. It has been demonstrated that novel methods Matrix-Pencil and Principle Component Auto-Regressive (PCAR) can be applied in real-time for speed detection. Steady-state and dynamic performance of Matrix-Pencil, PCAR, FFT, and Covariance methods were compared. The experimental results obtained indicate that, using PCAR and Matrix-Pencil methods, it is possible to achieve 0.5 Hz resolution, accuracy ±1 to ±2 rpm and settling-time of about 0.25 to 0.3 seconds for fewer data sets. The results showed that PCAR or Matrix-Pencil method leads to speed detection inaccuracies, predominant at light loads, after certain small data samples number. The trade-offs between samples number, accuracy and order number, for both PCAR and Matrix-Pencil methods, are more predominant for smaller data-sets at light loads.

Chapter 1: Introduction

1.1 Introduction to condition-based monitoring and motor current signature analysis

Three-phase induction motors are the most widely used motors and are critical component in various industries [46]. In the context of reliable safe operation and preventive maintenance of an induction motor, root-cause analysis (RCA), reliability-based maintenance (RBM) and condition-based maintenance (CBM) strategies have become integral parts of a modern maintenance management system.

In order to monitor the health of an induction motor, various sensors are needed to measure stator voltages and currents, air-gap flux densities, rotor position, speed, output torque, temperature, vibration etc [10-12].These sensors, in addition to an initial high cost, require mounting, wiring and maintenance. The installation cost of these sensors on small to medium range horsepower induction motors is not justified. Further, maintenance of these sensors requires physical access to the motor and their reliability largely depends on the environmental conditions of the installed motor [10-12].

Induction motor faults are broadly categorized as bearing related faults, stator related faults, rotor related faults and others as shown in Figure 1.1 below [10]:

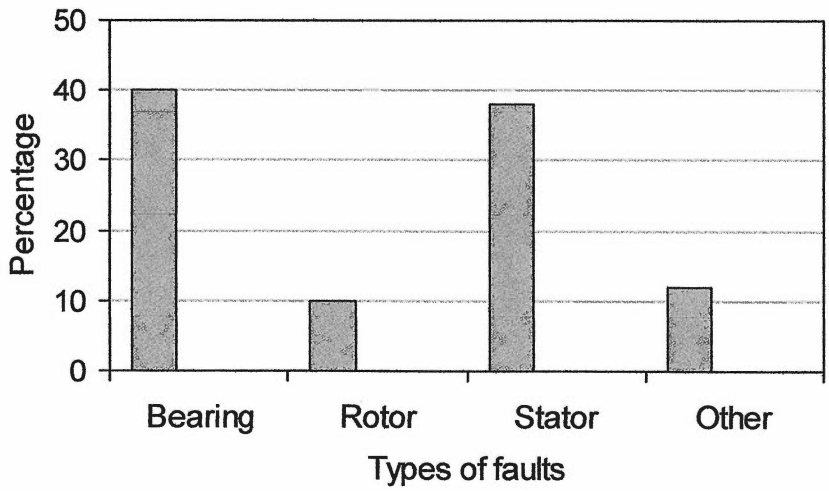

Figure 1.1: Types of induction motor faults.

However, the presence of any of the above fault conditions in an induction motor affects the way rotor and stator flux interacts and, thus, creates an internal magnetic imbalance which is reflected in the stator line current spectral signature [11]. Different abnormal conditions result in frequency components being induced in the stator line current at frequencies as given below [9-12]:

i. Broken rotor bars: $f_{sb} = f_1(1 \pm 2s)$ Hz. (1.1)

ii. Air-gap eccentricity: $f_{ec} = f_1\left\{(R \pm n_d)\left(\frac{1-s}{p}\right) \pm n_{\omega s}\right\}$ Hz. (1.2)

iii. Stator winding faults: $f_{st} = f_1\left\{\frac{n}{p}(1-s) \pm k\right\}$ Hz. (1.3)

iv. Bearing faults: $f_{bng} = \left|f_s \pm m f_{i,o}\right|$ Hz. (1.4)

$$f_{i,o} = \frac{N}{2} f_r\left[1 \pm \frac{b_d}{p_d}\cos\beta\right] \text{Hz.} \quad (1.5)$$

Where,

f_{sb} = Twice slip frequency side - band due to broken rotor bars.
f_{ec} = Frequency component due to air - gap eccentricity.
f_{st} = Frequency component due to shorted turns.
f_{bng} = Frequency component due to bearing faults.
$f_{i,o}$ = Vibration frequency component due to bearing dimensions.
f_1 = Supply frequency, Hz.
s = Slip.
p = Pole pairs.
n = 1,2,3,.....
k = 1,3,5,.....
R = Number of rotor slots.
$n_{\omega s}$ = 1,3,5,7,.....
$n_d = \pm 1$
β = Contact angle of the balls on the races.
N = Number of rotor slots.
f_r = Mechanical rotor speed in hertz.
b_d = Ball diameter
p_d = Bearing pitch diameter.
m = 1, 2, 3, ...

As noted in equations 1.1 to 1.5, speed is important in condition-based monitoring that needs to be measured accurately [13]. There are various other applications that include speed holding, speed matching, electronic gearboxes, speed regulation and speed control, in which accurate speed measurements are also required.

Motor current signature analysis (MCSA) is an analysis technique of stator line current spectrum that is being used as a noninvasive on-line CBM tool. It allows monitoring the health of an induction motor remotely from a motor control centre without requiring access to the motor. Figure 1.2 shows a block diagram of a typical MCSA scheme [12].

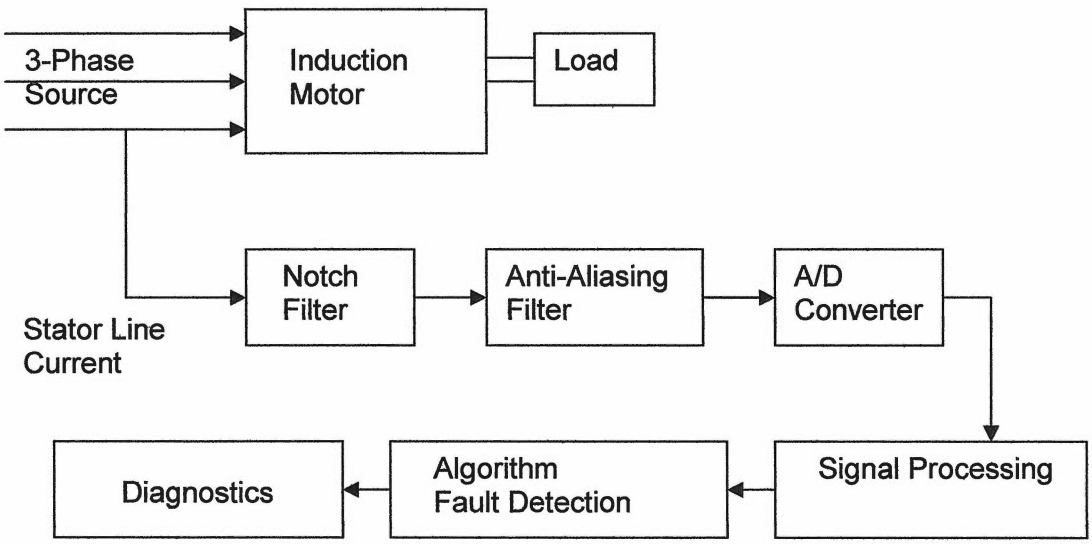

Figure 1.2: Simplified block diagram of MCSA technique.

1.2 Speed sensor-less operation of an induction motor

The use of conventional speed transducers reduces system robustness [32-35]. In a speed sensor-less system, state variables are derived from the motor terminal quantities in state observers and estimators. The performance reliability of these techniques relies heavily on the accuracy of machine model and motor parameter variations that lead to an increase in the speed measurement error at full-load [32-35].

Rotor slot harmonics (RSH) present in the stator line current provide a sensor-less speed measurement, utilizing spectral estimation techniques, which are independent of motor parameter variation [32-35]. There are numerous spectral estimation methods such as classical Fast Fourier Transform (FFT), Instantaneous Power FFT, Bispectrum, High-

Resolution Spectral Analysis, Joint-Time Frequency Analysis, Kalman Filter, Neural Networks etc. that are being studied and can be applied [11]. The key issues in any method are accuracy, resolution and dynamic behavior under changing load conditions. These issues become more critical in the small or fractional horse power (F.H.P.) induction motor. In the small or F.H.P. induction motor, a RSH of small magnitude is induced into the stator line current thus, signal-to-noise ratio (SNR) is low [7].

In order to minimize the noise before sampling and to detect speed of the F.H.P. induction motor with accuracy, it is recommended to use high precision A/D converter with no or minimized extra analog circuitry [7].

1.3 Research objective

In recognition of the facts listed earlier, the research has been conducted aiming to investigate and analyze the performance of various MCSA based spectral estimation methods, in terms of accuracy, resolution and dynamic behavior with regards to different data record lengths and sampling frequencies for sensor-less speed detection of the F.H.P. induction motor in real-time.

The outline of the thesis is as follows:

i. Research background.
ii. Theoretical background – RSH and spectral estimation methods.
iii. Experimental set-up and data acquisition – off-line and on-line.
iv. Real-time lab-view application and simulations.
v. Experimental real-time results and discussions – off-line and on-line.
vi. Conclusions and further work.

Chapter 2: Background

2.1 Rotor Slot Harmonics

The stator line current spectrum of an induction motor contains various harmonics, due to airgap magneto-motive force (MMF) spatial distribution and air-gap permanence variation, which are broadly termed as stator and rotor magnetomotive force harmonics, stator and rotor slot permeance harmonics, airgap eccentricity permeance harmonics, and permeance harmonics introduced by saturation [31, 32]. The frequency and amplitude of these harmonics are exploited to use them as a condition-based monitoring tool, for sensor-less speed detection and for sensor-less vector control using MCSA technique [3, 10-12, 45].

When the stator of a symmetrical three-phase induction motor is fed from symmetrical three-phase voltages, an air-gap field is established. These flux-density waves induce voltages in the rotor bars and in turn produce rotor MMF waves. The interaction of these MMF waves and the non-uniform air-gap permeance waves generates a new set of flux-density waves which in turn induces new harmonic frequencies in the stator voltages and currents termed as rotor slot harmonics (RSH) [45]. The RSH frequencies depend on rotor speed. The amplitude of RSH is a function of the load, number of rotor slots, slot size and skew [45].

By Ampere's law, the air-gap magnetic induction expression, which is the product of an air- gap magnetic conductance and the magnetic potential difference between the rotor and stator, is given by [30]:

$$B(\theta,t) = \Lambda(\theta,t).F(\theta,t) \tag{2.1}$$

The expression for the new set of flux density waves is given by [32]:

$$\begin{aligned} B(\theta,t) = {} & B_1 \cos(\omega_0 t - P\theta) + B_{r1} \cos[(\frac{Z}{P}\omega_r + \omega_0)t - (P+Z)\theta + \psi_{r1}] \\ & + B_{r2} \cos[(\frac{Z}{P}\omega_r - \omega_0)t - (P-Z)\theta + \psi_{r2}] \end{aligned} \tag{2.2}$$

Where,

θ = mechanical angle

t = time

ω_0 = supply angular frequency

P = number of pole pairs

ω_r = rotor angular velocity

ψ_{r1}, ψ_{r2} = phase angles

Z = Number of rotor slots

The above expression is mathematically equivalent to two oppositely traveling waves and induces corresponding harmonic frequencies in the stator line current [32]. The current in one phase is given by the expression [32]:

$$i_a(t) = \sum_{v=0}^{2} A_V \cos(\omega_v t - \psi_v) \tag{2.3}$$

The angular frequencies, due to forward (+ve sign) and reverse (-ve sign) traveling waves, of RSH are expressed as [32]:

$$\omega_{sh} = \frac{Z}{P}\omega_r \pm \omega_0 \tag{2.4}$$

The expression 2.4 for a non-sinusoidal supply is given by [32]:

$$\omega_{sh} = \frac{Z}{P}\omega_r \pm \alpha\omega_0 \tag{2.5}$$

Where, α = time harmonic order.

2.1.1 Speed Detection from RSH

The synchronous speed of an induction motor is given by [32]:

$$n_s = \frac{60 f_0}{P} \tag{2.6}$$

Where, n_s = synchronous speed in rpm.

f_0 = fundamental frequency in Hz.

P = Number of pole-pairs.

Frequency of rotor current, $f_r = sf_0$ (2.7)

Where, s = slip and is given by $\frac{n_s - n}{n_s}$ (2.8)

Combining equations 2.7 and 2.8,

Rotor rotational frequency, $f_{r0} = (1-s)f_0$ (2.9)

From equations 2.5 and 2.9,

Speed in rpm, $n = \frac{60}{Z}(f_{sh} \pm f_0)$ (2.10)

Where,

n = speed in rpm

Z = number of rotor slots

f_{sh} = rotor slot harmonic frequency in Hz.

f_0 = fundamental frequency in Hz.

Thus, using equation 2.11, rotor speed in rpm can be detected from RSH utilizing MCSA technique [32].

2.2 Research Background

The conventional speed transducers such as encoders and tachogenerators require mounting, wiring and maintenance and thus reduce system robustness. In early 1960's an attempt was made to replace the conventional speed transducers. In 1964, measuring axial leakage flux using a search coil was used by Jordan to detect speed from motor operation [33]. Speed information was also identified in motor current and voltages and in 1975 an analog slip calculator was developed by Abbondanti and Brennen using motor terminal quantities [33]. In 1979, Ishida et al. developed a new means of speed detection using rotor slot harmonics present in the stator voltages [33]. In 1985, Beck and Naunin measured rotor frequency using phase angle between voltage and current of the motor stator. Later in 1987 and 1989 attempts were made to improve these techniques in detecting speed by injecting a signal of constant frequency and by using phase locked loop which required modifying the machine [33]. In 1990, Williams et al. proposed a scheme to detect speed from rotor slot harmonics present in the stator line current [33]. Rotor slot harmonics present in the stator line current provide a means of detecting speed remotely from the motor control center in a non-invasive and non-intrusive manner. Since then research has been active and various spectral estimation techniques have been applied and examined to detect speed from RSH using MCSA technique. The spectral estimation techniques used in detecting speed from RSH can be broadly divided into categories namely; classical FFT, Parametric and statistical techniques.

In the early 1990's, most of the research focused on using FFT methods and to improve its accuracy and resolution by windowing and interpolation. However the outcome of the research was that the frequency resolution of the FFT can only be improved by increasing the data record length [35]. The FFT remained suitable for steady-state operation where longer data-records are available and there are no sudden changes in the load or speed [35].

In 1992, Ferrah, Bradley, Asher, and Woolfson [32-35] investigated the performance of FFT and various parametric methods to design a fast response speed detector. Their work included Goertzel Algorithm (GAL), Maximum Entropy Method (MEM), and Auto-Regressive (AR) techniques using least-mean square (LMS) algorithm. These methods were tested on a 4-pole, 50 Hz, 37 kilowatt induction motor.

In 1994, Blasco [31] tested the dynamic performance of FFT method by interpolation using batch and recursive algorithm on a 4 kilowatt induction motor in a vector controlled drive. In that same year Beguenane [30] showed how steady-state speed detection from RSH using FFT can be used in the identification of the rotor time constant of a 1.8 kilowatt induction motor. In his work, the stator current was amplified and low-pass filtered and then high-pass filtered and current harmonic was sensed by phase-locked loop (PLL) circuit. The output of PLL and high-pass filter was summed before digitizing the stator current. Also in 1994, Hurst, Habetler, Griva, and Profumo [26, 27, 29] proposed an application of speed detection from RSH using FFT in tuning the parameters of a speed observer in field oriented control of a 7.5 kilowatt induction motor. In their work, they applied decimation technique in order to improve the resolution and accuracy of FFT method and also proposed an initialization routine in an algorithm so that it is not dependent on knowledge of machine specific parameters, such as number of rotor slots. Most research was focused on FFT methods for speed detection from RSH and its application in speed control.

In the mid 90's root-cause analysis (RCA), reliability-based maintenance (RBM), and condition-based monitoring (CBM) became integral parts of preventive maintenance strategies of electrical drives. Research was conducted to investigate and develop noninvasive and non-intrusive on-line sensor-less RCA, RBM and CBM tools. More focus was placed on utilizing MCSA technique as it allows remote monitoring of an

induction motor [10]. Due to the non-stationarity of the current spectrum focus of the research turned to non-traditional spectrum estimation methods [23]. In 1996, Pillay and Xu [25] developed a real-time application in LabView for sensor-less speed detection by FFT method using MCSA

In 1997, Hurst and Habetler [23] presented a detailed comparison of parametric and non-parametric spectral estimation techniques for sensor-less speed detection of a 7.5 kilowatt induction motor. In their work they compare the performances of non-parametric methods such as periodogram and Blackman-Tukey methods and parametric methods such as auto-regressive (AR) and multiple signal classifier (MUSIC) methods and outlined the tradeoffs in accuracy, robustness and computation time [23].

In 1998, Restrepo et al. [18] studied the cross-term effects of Wigner-Ville Distribution (WVD), one of the joint time-frequency analysis methods, on detectability of slot harmonics. In this work, mathematical model of the motor was implemented in Matlab and analysis was not performed in real-time.

In 2002, Aller et al. [8] proposed an algorithm for sensor-less speed detection of 3.7 kilowatt induction motor using information from analytic wavelet transform by extracting ridges. Its performance was compared with short-time Fourier transform method under steady-state and dynamic conditions. Nutt et al. [7] outlined the problems with sensor-less speed detection from RSH in small or fractional horse power motors, due to small size of rotor slots that leads to small amplitude of RSH and thus low signal-to-noise ratio. They recommended using minimum or no analog circuitry prior to data-acquisition and to use high-precision data-acquisition instead in order to improve the detectability of RSH. They proposed a fast orthogonal search (FOS) algorithm using fewer current samples to detect speed of the F.H.P. induction motor and compared its performance with that of FFT method. It was shown in their work that frequency a resolution of 1 Hz. can be achieved with FOS algorithm from fewer data-records.

From the preceding literature review, it is observed that most of the research work in this area is either primarily focused on improving the FFT performance or applying high resolution or joint-time frequency spectral estimation techniques on larger motors or lacked the experimental results. The key issues, in all the literature reviewed, in detecting speed of an induction motor from RSH are accuracy, resolution and dynamic

performance under varying load conditions of various spectral estimation techniques. Due to these facts the present research is conducted. In this research experiment, stator line current is acquired using high-precision USB-2.0 data-acquisition module with built in signal-conditioning and isolation and thus, avoiding any extra analog circuitry [7] for signal-conditioning and to analyze the performance of spectral estimation techniques without using any analog anti-aliasing filter. For this reason, an algorithm from A. Ferrah et al. work [32-35] is selected due to its suitability to reject noise outside the frequency band of interest and simplicity. Ferrah et al. proposed this algorithm with FFT method to detect speed of a 35 kilowatt induction motor. In this research, the same algorithm is further extended to apply various spectral estimation techniques to detect speed of the F.H.P. induction motor and is implemented in real-time using LabView7.1 in a PC-Based environment. This work is a further extension to the knowledgebase in this field with a significant contribution as outlined below:

a. Analysis of various spectral estimation techniques in terms of accuracy, resolution, and dynamic behavior under varying load conditions with regard to different data-record lengths at different sampling frequencies for sensor-less speed detection of the F.H.P. induction motor, in real-time, using minimum external analog circuitry.
b. Performance analysis of novel spectral estimation method Matrix-Pencil, in terms of speed detection, in real-time.
c. Real-time PC-based application development, using LabView 7.1 software and its signal processing tool-set, that allows investigating the dynamic performance of applied spectral estimation techniques in one application, in real-time.

Chapter 3: Spectral Estimation Methods

3.1 Fast Fourier Transform

The Fourier transform maps time domain functions into the frequency domain. The Fourier transform of a time function x (t) is given by [41, 47, 48]:

$$X(f) = F\{x(t)\} = \int_{-\infty}^{+\infty} x(t)e^{-j2\Pi ft}\,dt \qquad (3.1)$$

where, X (f) is the Fourier transform.

The discrete Fourier transform (DFT) maps discrete-time sequences into discrete-frequency transformations. The expression for DFT is given by [41, 47, 48]:

$$X_k = \sum_{i=0}^{n-1} x_i e^{-j2\Pi ik/n} \text{ for k} = 0,1,2,.....,\text{n} - 1 \qquad (3.2)$$

where, x is the input sequence,

X is its DFT, and

n is the number of samples.

The DFT requires approximately n^2 complex operations. An algorithm used to solve the DFT in a computationally efficient way is known as fast Fourier transforms (FFT). It requires $n\log_2$ (n) operations [47, 48].

The frequency resolution of the FFT depends on the length of the data-record. For a fixed sampling frequency fs, the frequency resolution, in Hz. is [41, 47, 48]:

$\Delta f = \frac{f_s}{N}$, where, N is the number of samples. (3.3)

The FFT output is of complex form and is given by:

$$X(m) = X_{real}(m) + jX_{imag}(m) \qquad (3.4)$$

The magnitude of FFT is given by:

$$X_{mag}(m) = |X(m)| = \sqrt{X_{real}(m)^2 + X_{imag}(m)^2} \qquad (3.5)$$

The Power, P(s) is [47, 48] = $|X(m)|^2$ (3.6)

3.2 Model-Based Methods

As discussed in section 3.1, the frequency resolution of the FFT depends on the

number of samples characterized by $\Delta f = \frac{f_s}{N}$ i.e. more samples for a given sampling frequency result in a better frequency resolution. In many practical applications it may not be always possible to have a larger number of samples due to lack of data or to ensure that the spectral characteristics of a signal is preserved and do not change over time [37,41]. In these types of applications, model-based methods are better in performance than FFT methods [37]. In model-based methods, assuming that the signal is modeled as required, after computing the coefficients, missing data can be predicted from the finite data set that improves the frequency resolution with a fewer numbers of data samples [23, 35, 37].

Nonparametric methods estimate power spectral density from the signal itself. One such method is periodogram, which is the magnitude squared of the FFT, as explained in the section 3.1. Parametric methods use a linear process driven by white noise to estimate the power spectrum. The output of this model is compared with the input to find a best match with feedback adjustments on the parameters. The model types differ by the nature of their transfer function [48]. The common model types are: autoregressive (AR), moving average (MA) and autoregressive moving-average (ARMA) models [35, 48]. The transfer function of an AR model has a polynomial in the denominator and is also referred as all-pole model. The transfer function of moving average has a polynomial in the numerator and is also referred to as all-zero model. ARMA model has polynomial both in numerator and denominator and is also referred to as pole-zero model. The algorithms for MA and ARMA involve more computation and may converge to the wrong solution [48]. There are various techniques for estimating the AR modal coefficients and power spectrum.

Eigen-analysis spectral methods are particularly effective for sinusoidal, exponential, or narrow-band processes [48]. They provide better resolution and frequency estimation at high noise levels [48]. The eigenvector approach divides the data into two orthogonal subspaces: a signal subspace and noise subspace [23, 48]. The Eigen-decomposition produces Eigen-values of decreasing order. The size of the Eigen-values can determine the signal subspace. The noise subspace is spanned by the minimum eigenvector [23, 48]. Principal component analysis belongs to statistics branch known as multivariate analysis [48]. In multivariate analysis, multiple variables are represented by a single vector:

$$x = [x_1(t), x_2(t), x_3(t).....x_m(t)]^T$$

Where, T stands for transposed and t = 1.....N. There are m variables of x representing N observations of time samples [48]. The objective of multivariate analysis is to find transformations of the multivariate data to reduce the dimensions of the data set. The techniques in multivariate analysis differ in the way transformations are applied with a common goal to reduce the dimensionality of the data. A technique to reduce the covariance matrix into a diagonal matrix by multiplication with an orthonormal matrix is [48] $U^TSU = D$ where S is a square covariance matrix, D is a diagonal matrix, and U is an orthonormal matrix. This rotation produces a new covariance matrix, D with zero covariance. The diagonal elements of D are the variances of a new data. These variances can be used to determine principle components. The Eigen-values or roots are solved by the determinant $\det |S - \lambda I| = 0$, where I is the identity matrix. This technique is computationally intensive for longer data-sets [48]. Another technique uses singular value decomposition of data matrix. When singular value decomposition is used, the Eigen-values are ordered by size from which significant modes can be determined and dimensionality of the data set can be reduced [48]. This technique is computationally efficient [28].

3.2.1 Autoregressive and Moving-average (ARMA) models

ARMA model of data samples x[n] is given by [23, 35-37, 48]:

$$x[n] = -\sum_{k=1}^{p} a_k x[n-k] + \sum_{n=0}^{q} b_m w[m-n] \quad 0 \le n \le N \tag{3.7}$$

Where, b_0=1 and w[n] is white noise with zero mean and variance σ^2.

For a_k=0 for all k in equation 3.7, the equation reduces to:

$$x[n] = \sum_{m=0}^{q} b_m w[n-m] \qquad for\ 0 \le n < N \tag{3.8}$$

Equation 3.8 is called moving-average (MA) model [35-37, 48].

For b_m=0 for m>0, the ARMA model in equation 3.7 becomes

$$x[n] = -\sum_{k=1}^{p} a_k x[n-k] + w[n] \qquad \text{for } 0 \le n < N \tag{3.9}$$

This is called auto-regressive (AR) model [35-37, 48].

From the above equation, future data is predicted with error w[n], from past but known data. The predicted data is given by [35-37, 48]:

$$\hat{x}[n] = -\sum_{k=1}^{p} a_k x[n-k] \qquad p \le n < N$$

or (3.10)

$$\begin{bmatrix} x[p-1] & x[p-2] & \ldots & x[0] \\ x[p] & x[p-1] & \ldots & x[1] \\ . & & & \\ . & & & \\ x[N-2] & x[N-1] & \ldots & x[N-p+1] \end{bmatrix} \begin{bmatrix} a_1 \\ a_2 \\ . \\ . \\ a_p \end{bmatrix} = -\begin{bmatrix} \hat{x}[p] \\ \hat{x}[p+1] \\ . \\ . \\ \hat{x}[N-1] \end{bmatrix}$$

The above equation is known as forward prediction [35-37, 48].

The backward prediction is given by the following expression [35-37, 48]:

$$\hat{x}[n] = -\sum_{k=1}^{p} a_k^{*} x[n+k] \qquad 0 \le n < N \tag{3.11}$$

or

$$\begin{bmatrix} x[1] & x[2] & \ldots & x[p] \\ x[2] & x[3] & \ldots & x[p+1] \\ . & & & \\ . & & & \\ x[N-p] & x[N-p+1] & \ldots & x[N-1] \end{bmatrix} \begin{bmatrix} a_1^{*} \\ a_2^{*} \\ . \\ . \\ a_p^{*} \end{bmatrix} = \begin{bmatrix} \hat{x}[0] \\ \hat{x}[1] \\ . \\ . \\ \hat{x}[N-p-1] \end{bmatrix}$$

For an AR model, the power spectrum is obtained by taking the reciprocal of the FFT of the computer coefficients a_k and is given by the expression [35-37, 48]:

$$P(f) = \frac{\sigma^2}{\left| 1 + \sum_{k=1}^{p} a_k e^{-2\Pi f k} \right|^2} \tag{3.12}$$

3.2.2 Covariance Method

The mean of a data set X is: $\overline{X} = \dfrac{\sum_{i=1}^{n} X_i}{n}$.

The two data sets having the same mean may be quite different in how the data is spread [48]. The Standard Deviation, average distance from the mean of the data set to a point, is a measure of spread of the data.

The Standard Deviation: $s = \sqrt{\frac{\sum_{i=1}^{n}(X_i - \bar{X})^2}{(n-1)}}$.

Variance, the standard deviation squared, is another measure of the spread of data in a data set and is given by: $s^2 = \frac{\sum_{i=1}^{n}(X_i - \bar{X})^2}{(n-1)}$.

Standard deviation and variance are useful only for functions of one dimension. Covariance is measured between two dimensions [48]. It is a measure to find out how much the dimensions vary with respect to each other from the mean. Covariance between one dimension and itself is variance. The covariance between two functions is given by [48]:

$$Cov = \sigma_{x,y} = \sum_{k=1}^{M}[y(k) - \bar{y}][x(k) - \bar{x}]/(n-1)$$

The rows in a multivariate data matrix are the waveform time samples and the columns are different observations of a signal [48]. The diagonals in covariance matrix are the variance of the columns of the data matrix and off-diagonals are the covariance between columns. The Covariance matrix is given by [48]:

$$S = \begin{bmatrix} \sigma_{1,1} & \sigma_{1,2} & ..... & \sigma_{1,N} \\ \sigma_{2,1} & \sigma_{2,2} & ..... & \sigma_{2,N} \\ . & . & . & . \\ . & . & . & . \\ \sigma_{N,1} & \sigma_{N,2} & ..... & \sigma_{N,N} \end{bmatrix}$$

The covariance matrix is square and is symmetrical about the main diagonal.

The covariance method for AR spectral estimation is based on minimizing the forward prediction error in the least squares manner [37]. It computes the coefficient such that the error between sampled data x[n] and predicted data $\hat{x}[n]$ is minimized as following [37]:

$$\min_{a_k} \sum_{n=p}^{N-1} \left| x[n] - \hat{x}[n] \right|^2$$

For N samples of x[n], Covariance method minimizes the error between x[n] and $\hat{x}[n]$ for N-p points where, $p \leq n < N$. Therefore, it is sensitive to noise [35-37].

3.2.3 Principle Component Auto-Regressive (PCAR) Method

In the PCAR method, a linear system is expressed as follows [37]:

$$\begin{bmatrix} X_f \\ X_b \end{bmatrix} \vec{a} = -\begin{bmatrix} \vec{x}_f \\ \vec{x}_b \end{bmatrix} \tag{3.13}$$

Where, $\vec{a}$ is a data vector and is given by the following expression [37]:

$$\vec{a} = [a_1\ a_2 \ldots\ldots a_p]^T$$

$\vec{x}_f$ and $\vec{x}_b$ are the right sides of the forward and backward prediction. X_f and X_b are the left sides of the forward and backward prediction.

The optimal coefficients are obtained using following expression [37]:

$$\vec{a} = \sum_{i=1}^{L} \frac{1}{\lambda_i} \vec{v}_i \vec{v}_i^{\,T} X^T \vec{x} \tag{3.14}$$

Where,

$$X = \begin{bmatrix} X_f \\ X_b \end{bmatrix} \quad \text{and} \quad \vec{x} = \begin{bmatrix} \vec{x}_f \\ \vec{x}_b \end{bmatrix}$$

λ_i = L largest eigenvalues of the matrix X.

$\vec{v}$ = L corresponding eigenvectors.

L represents number of complex sinusoids.

The PCAR method uses both forward and backward prediction, therefore, it has more data points to average and is less sensitive to noise as compared to the Covariance method [37].

3.2.4 Matrix-Pencil (M.P.) Method

The Matrix-Pencil method is a relatively new method and is being used in areas such as ultrasonic field, electromagnetic, acoustic, wireless transmission propagation, wire-less adhoc sensor network and in computer aided control system [28]. It estimates complex resonant frequencies and gives a discrete spectrum [28].

The M.P. method approximates the signal by weighted sum of complex exponentials. Any harmonics can be retrieved from the following equation [28]:

$$x[k] = \sum_{l=1}^{L} a_l e^{jk\omega_l} + n[k] \text{ , where, k=0, 1....N-1} \qquad (3.15)$$

Where, x [k] and n[k] are the measured samples and noise samples, a_l and ω_l are unknown amplitudes and frequencies. The Hankel matrix X, where off-diagonal entries are equal, is constructed from the measured samples. The two L rank matrices Y1 and Y2 can be constructed from X by deleting first and last d rows. Choosing d >1 improves resolution and yields smaller variance estimates [48]. By combining Y1 and Y2, the data matrix [Y] can be given as [28]:

$$[Y] = \begin{bmatrix} y(0) & y(1) & .... & y(L) \\ y(1) & y(2) & .... & y(L+1) \\ . & . & . & . \\ . & . & . & . \\ y(N-L-1) & Y(N-L) & .... & y(N-1) \end{bmatrix}_{(N-L)x(L+1)} \qquad (3.16)$$

Where, L is the pencil parameter and is chosen between N/3 to N/2. For these values variance is minimum [28]. Singular value decomposition of the matrix [Y] is:

$[Y] = [U]\,[D]\,[V]^H$

Where, [U] and [V] are unitary matrices containing eigenvectors of $[Y][Y]^H$ and $[Y]^H[Y]$ respectively. [D] is a diagonal matrix containing singular values of [Y]:

$[U]^H[Y][V] = [D]$. From the ratio of singular values to the largest one, the choice of significant modes M is done. Next, matrix [V'], containing M dominant right-singular vectors, is constructed:

$[V'] = [v_1, v_2 \ldots\ldots\ldots\ldots v_M]$

The right-singular vectors from M+1 to L, corresponding to the small singular values are discarded [28].

$[Y1] = [U][D'][V_1']^H$ and $[Y2] = [U][D'][V_2']^H$

Where, $[V_1']$ and $[V_2']$ are obtained from deleting the last row and first row of [V'] respectively. [D'] is obtained from M columns of [D] corresponding to the M dominant singular values [28]. The roots (desired frequencies) may be found as the generalized Eigen values of the matrix pencil pair from $[Y1]^{-1}[Y2] - \lambda I$.

3.3 Joint Time-Frequency Analysis (JTFA) Methods

In the FFT and model-based methods, a signal is analyzed in the frequency domain only. JTFA methods allow analyzing the signal both in time and frequency domain simultaneously [16, 17, 37]. JTFA methods are more useful for applications where it is important to observe a change of power spectrum over time. It gives the instantaneous spectrum [16, 17, 37]. The simplest approach to obtain frequency as a function of time is to divide the data series in overlapping blocks by using a window and then apply the Fourier transform to each block. This technique is known as short-time Fourier transform (STFT) [16, 17, 37]. The frequency and time resolution depends upon the size of window. A small window gives better time resolution and a wide window gives better frequency resolution which is more commonly termed as window effect [16, 17, 37]. According to Heisenberg uncertainty principle, an optimal joint time-frequency resolution can be achieved by using a Gaussian window. To over-come the window effect, a Wigner-Ville Distribution (WVD) method was developed. It gives better frequency resolution but it has the disadvantage of cross-term interference [16, 17, 37]. To overcome cross-term interference, the Gabor spectrogram or Adaptive spectrogram can be used. For any of the above methods, there are always trade-offs between resolution and computing time or complexity [37].

3.3.1 Short-time Fourier Transform (STFT)

In STFT, time-frequency information is spread in atoms known as Gabor atoms that are obtained by translating a window g in time and frequency as given below [16, 37]:

$$g_{u,\xi} = g(t-u)e^{i\xi t}$$

STFT correlates a signal x (t) with window as:

$$S_f(u,\xi) = \int_{-\infty}^{+\infty} x(t)g(t-u)e^{i\xi t}$$

The discrete representation of STFT-based spectrogram is given by the following expression [37]:

$$S[m\Delta M, n] = \left| \sum_{i=0} x[i]g[i-m\Delta M]e^{-j2\Pi ni/N} \right|^2$$

Where, N denotes the number of frequency bins and ΔM denotes the time sampling interval.

3.3.2 Gabor Spectrogram

In the Gabor expansion method, the signal x[i] is represented by a weighted sum of time-shifted and frequency-modulated function h[i] and is expressed as [16, 17, 37]:

$$x[i] = \sum_{m}\sum_{n=0}^{N-1} C_{m,n} h[i - m\Delta M] e^{j2\Pi ni/N}$$

Where, $C_{m,n}$ are Gabor coefficients and are computed by the STFT as shown below [16, 17, 37]:

$$C_{m,n} = STFT[m\Delta M, n] = \sum_{i=0} x[i]\gamma^{*}[i - m\Delta M] e^{-j2\Pi ni/N}$$

Where, N denotes the number of frequency bins and ΔM denotes a sampling interval. The function γ[i] is dual function of h[i]. The Gabor spectrogram is given by the following equation [16, 17, 37]:

$$GS_{D}[i,k] = \sum_{|m-m'|+|n-n'|\leq D} C_{m,n} C_{m',n'} WVD_{h,h'}[i,k]$$

Where, $WVD_{h,h'}[i,k]$ denotes the cross-WVD of two frequency-modulated Gaussian function [37]. Wigner-Ville distribution (WVD) is given by [37]:

$$\text{WVD [i, k]} = \sum_{m=-L/2}^{L/2} R[i,m] e^{-j2\pi km/L}$$

Where, R [i, m] = z [i+m] z^{*}[i-m] and z[i] is the analytical form of the signal x[i].

3.3.3 Cone-Shaped Distribution (CSD)

Applying 2D filtering to the Wigner-Ville distribution to reduce the cross-term interference yields the equation given below [16, 17, 37]:

$$C[i,k] = \sum_{m=-L/2}^{L/2} \sum_{n} \phi[n,m] R[i-n,m] e^{-j2\pi km/L}$$

Where, $\phi[n,m]$ denotes the kernel function. In CSD, the kernel function is defined by [16, 17, 37]:

$$\phi[i,m] = \begin{cases} e^{-\frac{\alpha m^2}{c}} & \text{for i} < |\text{m}| \\ 0, \text{ otherwise} \end{cases}$$

Where, c is a constant and by adjusting α, trade-off between cross-term interference and time-frequency resolution can be achieved [37].

3.3.4 Adaptive Spectrogram

The adaptive transform represents the signal x[i] as a weighted sum of adaptive Gaussian function and is given by the expression [16, 17, 37]:

$$x[i] = \sum_{k=0}^{D-1} A_k h_k[i]$$

Where, $h_k[i]$ is the adaptive Gaussian function $h_k[i]$ and is given by the expression [16, 17, 37]:

$$h_k[i] = (\alpha_k \Pi)^{-0.25} \exp\left\{ -\frac{[i-i_k]^2}{2\alpha_k} + j(2\Pi\theta_k[i-i_k]) \right\}$$

The adaptive spectrogram is given by the equation [16, 17, 37]:

$$AS[i,n] = 2\sum_{k=0}^{D-1} |A_k|^2 \exp\left\{ -\frac{[i-i_k]^2}{\alpha_k} - \alpha_k[n-\theta_k] \right\}$$

The analytical details of the expressions for the above methods and their derivations are given in [16], [17], [23], [28], [35-37], [41], [47] and [48].

Chapter 4: Experimental-Setup and PC-Based Implementation

4.1 RSH Calculations and Speed Measurements

The identification of the speed-related slot harmonics, described in the previous chapter, was carried out using an experimental test rig. The rig consists of a Lab-Volt three phase power supply, supplying a three-phase wound rotor induction motor coupled to an electrodynamometer used for loading the motor. The induction motor is a 208volts, 4-pole, 60Hz, three-phase, 175 watt wound rotor machine. There are 24 rotor slots. For experiment, its stator was connected in wye and its rotor terminals were shorted.

Table 4.1: F.H.P Induction Motor Specifications.

Power	175 watts
Voltage	208 volts
Current	1.3 amps.
Speed	1800 rpm
Frequency	60 Hz
Stator	3 phase, wye-connected, 4-poles
Rotor	Wound rotor, 24 slots, terminals shorted.

The speed was measured at different loads using digital tachometer, and rotor slot harmonics were calculated using the expression $n = {}^{60}/_{Z}(f_{sh} \pm f_0)$ [32, 33]. The speed measurements and rotor slot harmonic calculations are tabulated below in table 4.2. From the above calculations, two rotor slot harmonics are identified. For analysis and spectral estimation only the first harmonic will be considered. The other RSH is caused by the reverse rotating field due to asymmetry and voltage unbalance and there is uncertainty of its strength [45]. For the 24-rotor slot, 4-pole test machine, the first speed-related slot harmonic (RSH1) is found to be confined to an interval [$9f_0$ $11f_0$], where f_0 is the fundamental frequency component at 60 Hz. As the load increases, the slot harmonic frequencies decrease with the increasing load.

Table 4.2: Measured speed and calculated RSH at different loads.

S.No.	Load Torque (N-m)	Measured Speed (rpm)	Slip (%)	Calculated RSH1 (Hz.)	Calculated RSH2 (Hz.)
1.	1.2	1543	14.3	557.2	677.2
2.	1.0	1586	11.9	574.4	694.4
3.	0.8	1628	9.6	591.2	711.2
4.	0.6	1667	7.4	606.8	726.8
5.	0.4	1700	5.8	620	740
6.	0.2	1730	3.9	632	752
7.	0.1	1746	3	638.4	758.4
8.	0.06	1752	2.6	640.8	760.8

4.2 Off-Line Identification of RSH

The stator line current was captured on a Hewlett Packard oscilloscope using a 2 ohm shunt resistor. Communication between the host computer and oscilloscope was carried via RS-232 interface using HP BenchLink XL 54600 scope toolbar. Real-time data records were collected at 1752, 1746, 1730, 1700, 1667, 1628, 1586 and 1543 rpm and at a load level of about 1.2 Nm. full load decreasing gradually, in 8 steps, to near zero-load level. The speed at different load levels was measured by using a digital tachometer. The current is sampled at sample interval of 500 ms. with data record length of 2000 samples at a sampling frequency $f_s = N/T = 2000/0.5 = 4$ kHz. The discrete values of time and amplitude were stored in excel files which were retrieved into Matlab software for offline processing and identification of RSH. The Hanning window was applied in time domain before taking the 2048-point FFT of the discretized current signal to reduce spectral leakage [32]. Figure 4.1 shows a picture of experimental set-up for off-line. Figure 4.2 shows a typical stator line current signal at 60 Hz before and after hanning window is applied in time domain. Figure 4.3 shows a frequency spectrum of stator line current at load torque of 1.2, 0.4, and 0.06 Nm respectively.

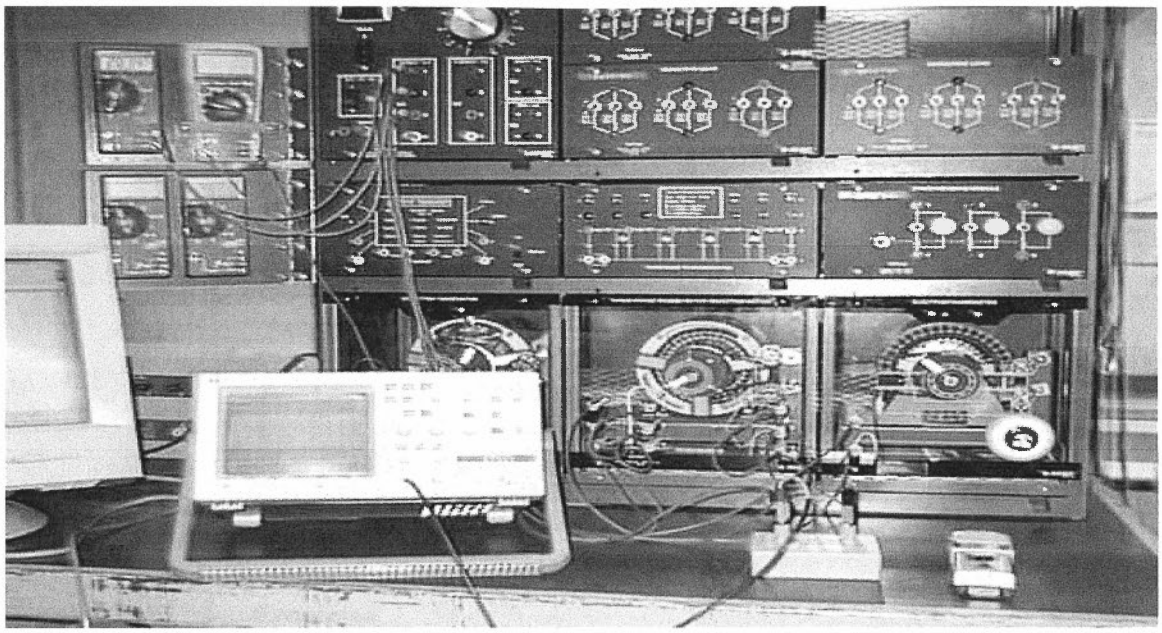

Figure 4.1: Experimental-Setup for identification of RSH and off-line processing.

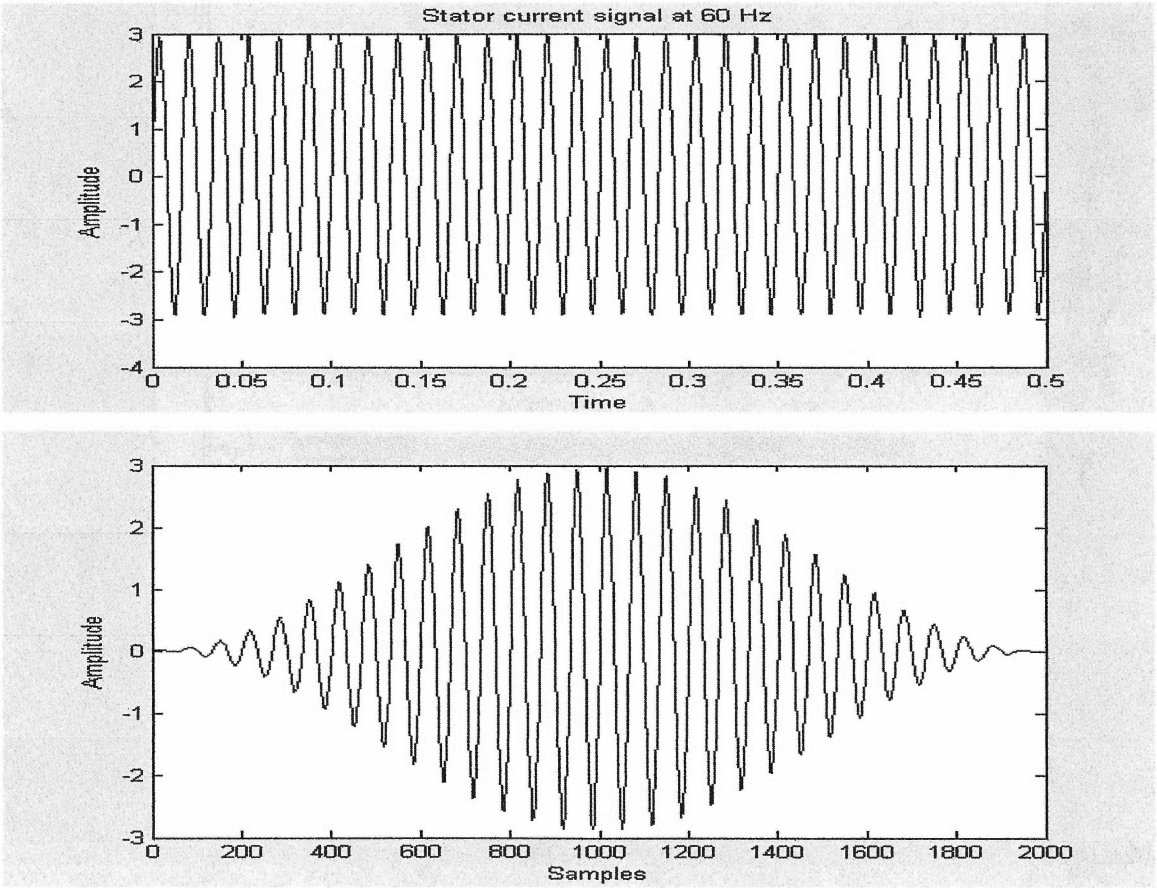

Figure 4.2: Stator line current signal before and after hanning window is applied.

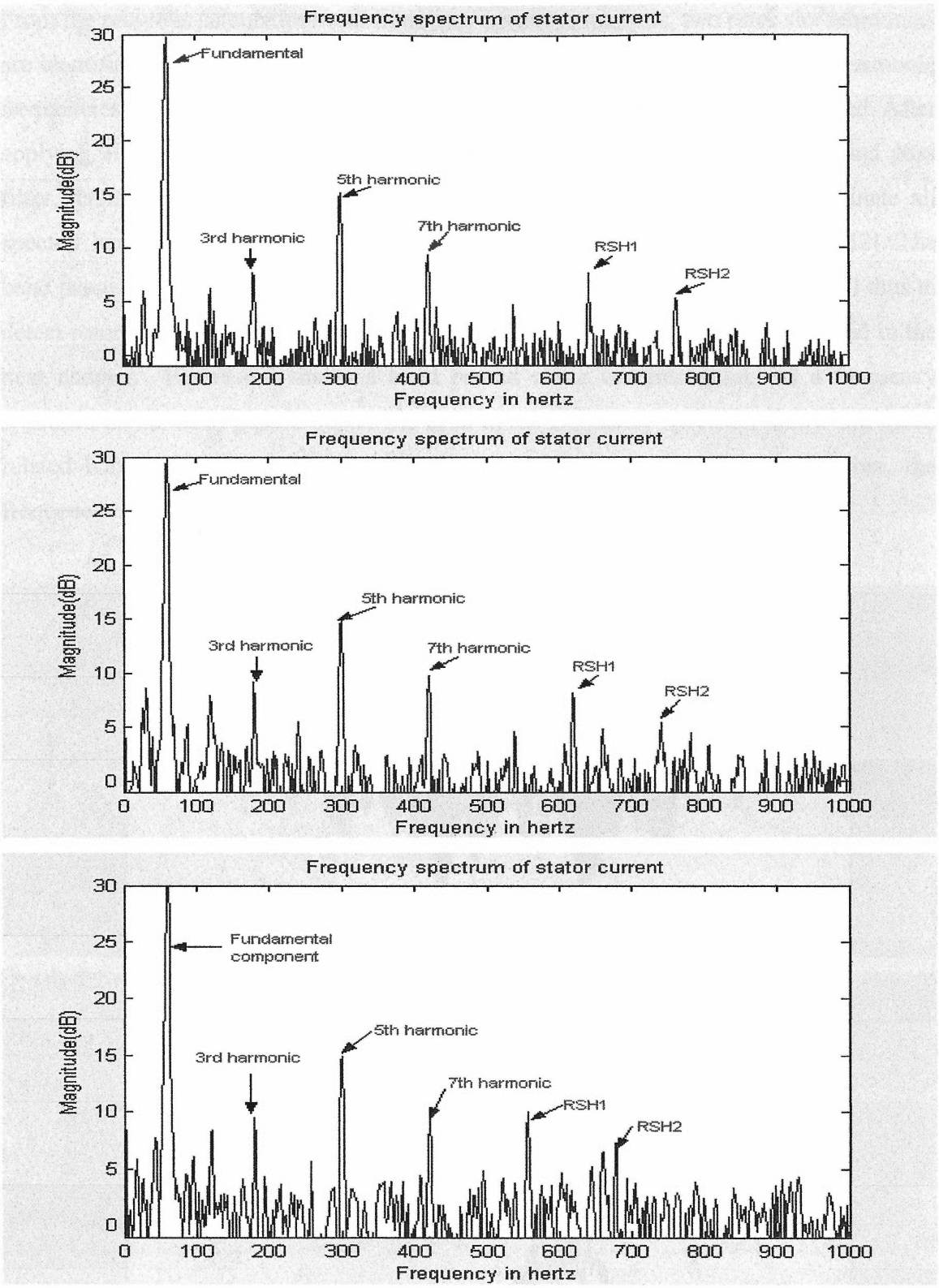

Figure 4.3: FFT of stator line current at load torque of 1.2, 0.4 and 0.06 Nm. respectively.

From the previous calculations and frequency spectrum analysis, two rotor slot harmonics are identified. From Figure 4.3 it is observed that as the load increases, the slot harmonic frequencies decrease with the rotor speed and its amplitude increases with the load. After applying Hanning window to the stator current, the 8-th order Butterworth band pass filter, having a band pass interval of [550Hz 650Hz], is then applied to eliminate all spectral harmonics outside the range containing the expected slot harmonics [32]. The band passed signal is then used in simulations to estimate rotor slot harmonics and thus to detect rotor speed by using different frequency estimation techniques as explained in the next chapter. Figure 4.4 shows a band passed stator current signal and a frequency spectrum of the band passed signal. As seen in the frequency spectrum below the speed related harmonic has a maximum peak in the given frequency band. Therefore, the frequency corresponding to the maximum peak is the rotor slot harmonic [32-35].

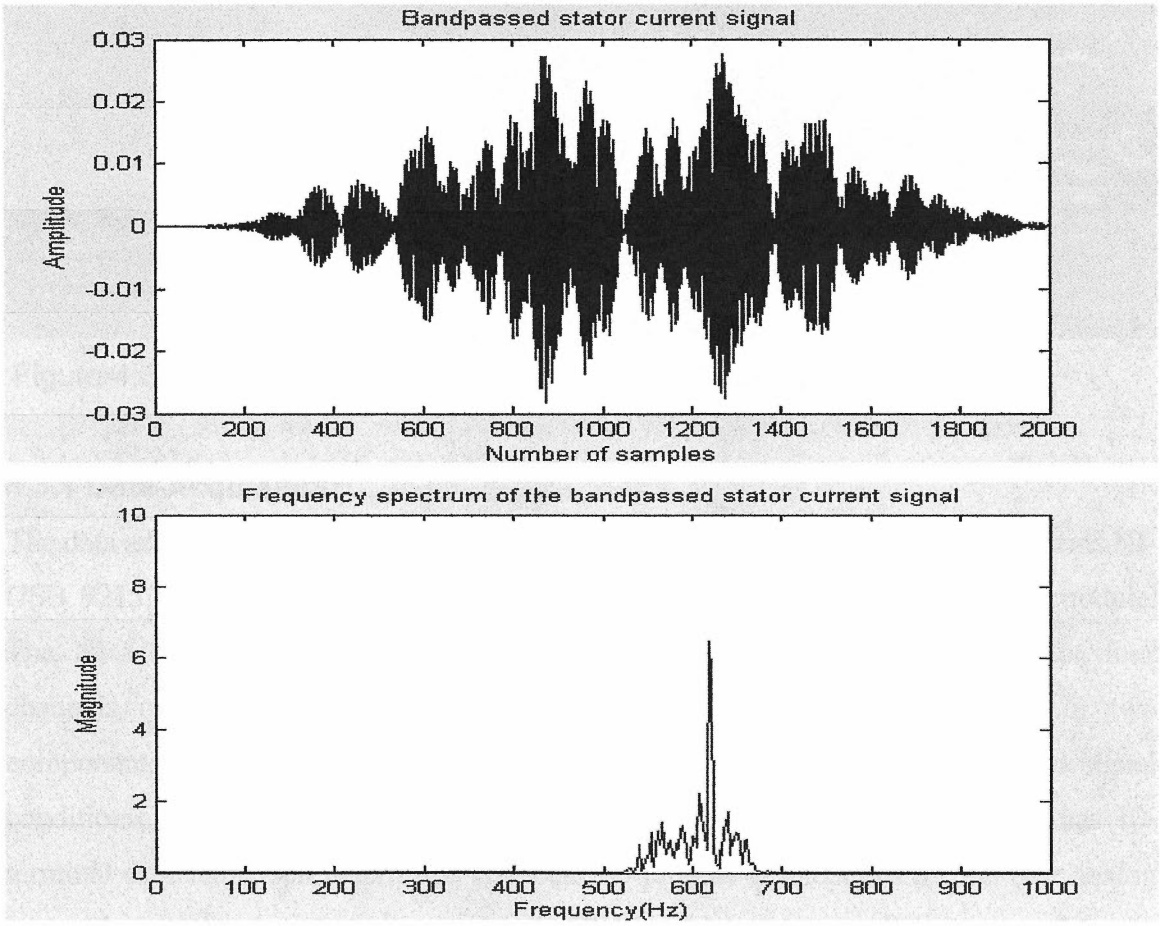

Figure 4.4: Band-pass filtered stator line current signal and it's FFT.

4.3 Experimental Set-up for On-line Speed Detection

The experimental set-up for on-line speed detection consisted of a Lab-Volt three phase variable power supply supplying a three-phase wound rotor induction motor coupled to an electrodynamometer, as explained in section 4.1. Figure 4.5 shows a picture of on-line experimental set-up.

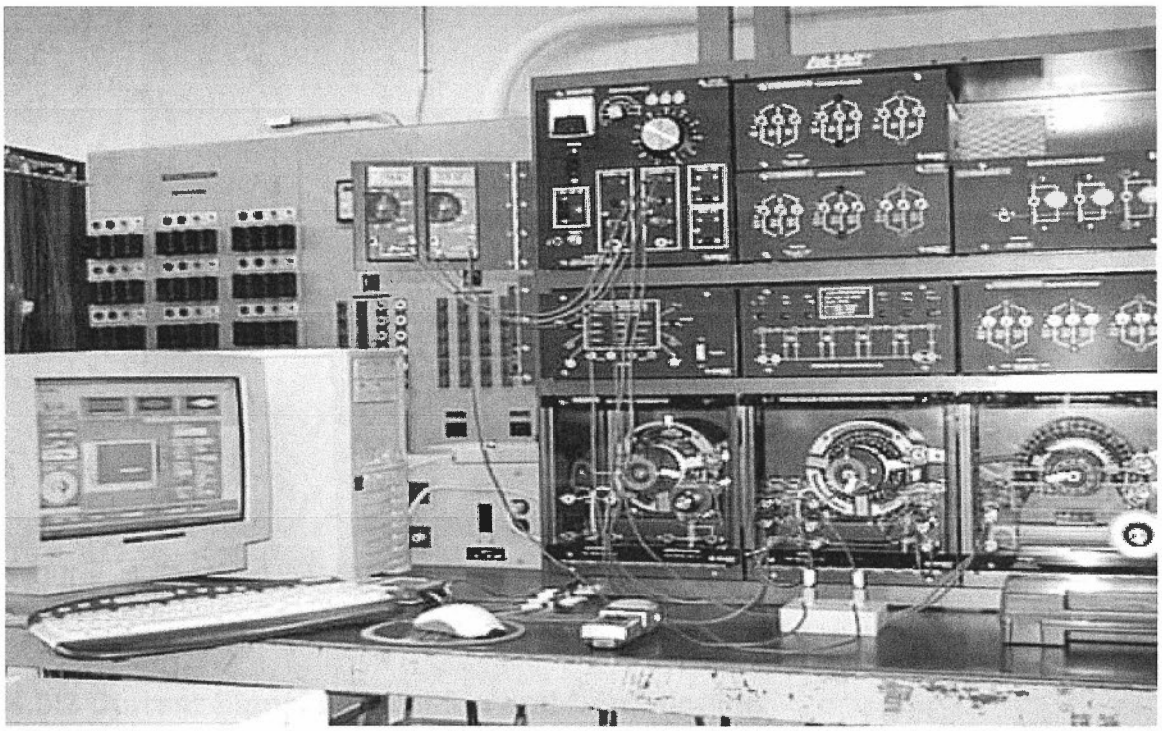

Figure 4.5: Experimental set-up for on-line speed detection.

4.3.1 Data-Acquisition

The data acquisition system used in the experimental set-up was National Instruments NI-USB 9215, 4-channel, ± 10V DC, 16-bit simultaneous sampling analog input module. The NI USB-9215 data acquisition module provides a USB-2.0 interface for four channels of 16-bit simultaneous sampling analog inputs [38]. It consists of two components a Crio-9215 module and a USB-9161 carrier and has an integrated signal conditioning. The driver software for this module is NI-DAQmx Base [38]. It has 10-terminal detachable screw-terminal connector to provide connections for the four analog input channels and a common terminal, COM, which is internally connected to the isolated ground reference of the module [38]. The common ground is isolated from the

chassis and the host computer. Each channel has built in over-voltage protection. Before the signal is sampled by a 16-bit ADC, it is buffered and conditioned by the instrumentation amplifier [38]. Each channel has independent track and hold amplifiers [38]. Figure 4.6 shows a picture of the NI USB-9215 data acquisition module as connected in the on-line experiment.

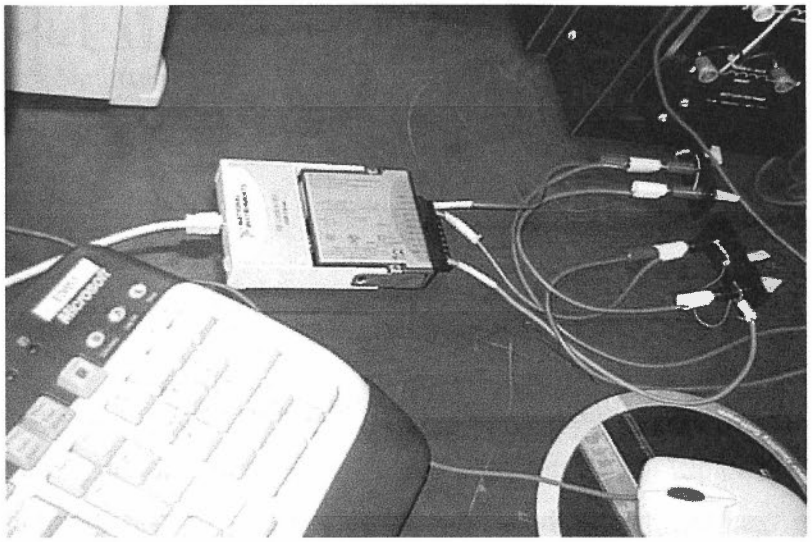

Figure 4.6: NI USB-9215 data acquisition module as connected in the experiment.

4.3.2 Current Signal Acquisition and Conditioning

The signal of interest for this experiment is the motor stator line current. The signal conditioning device must convert this to voltage. Regardless of the type of sensor or transducer, the general signal conditioning requirements are amplification, attenuation, filtering, isolation, multiplexing, simultaneous sampling, digital signal conditioning etc. [38]. Any real-world signal contains frequency components greater than the Nyquist frequency aliased to the signal. This introduces an error in the measurement. To prevent this either a sampling frequency is set to 5 to 10 times the maximum frequency component in the signal or analog low-pass filter, which is essentially an anti-aliasing filter, is used before analog-to-digital (ADC) converter [36,38]. Due to these facts, a typical MCSA scheme used in most of the references cited is shown below in Figure 4.7. Essentially, in a MCSA scheme the stator line current is notch filtered to remove

fundamental component, scaled and then is supplied to an analog anti-aliased filter before it is fed to the ADC [9-13].

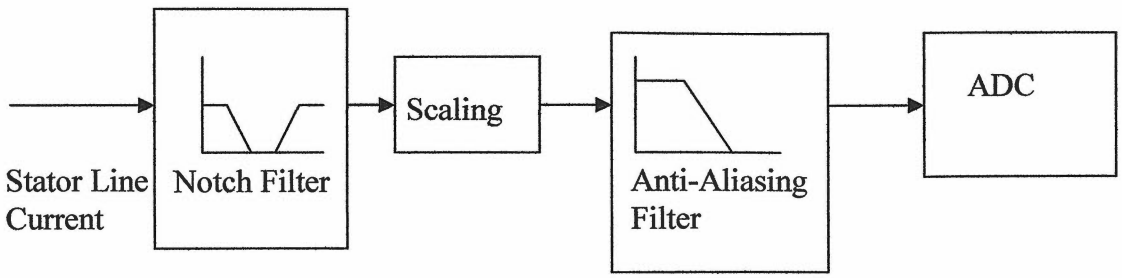

Figure 4.7: Conventional data-acquisition of stator line current.

Since, the objective of the research is to use minimum or no analog circuitry for the F.H.P. induction motor, due to the reasons as explained in chapter 1 and chapter 2, the high-precision 16-bit NI USB-9215 DAQ module which has integrated signal conditioning and isolation, as explained in section 4.3.1 of this chapter, is selected for this experiment. To convert a current signal to a voltage signal a 2 ohm shunt resistor is used. The voltage drop across the resistor for a motor of this rating is 2 volts at full-load. It is recommended to amplify the signal to meet the dynamic range of DAQ module which is ±10V for the selected DAQ module [39, 40]. It can be accomplished either by using high value of resistance or by using an analog amplifier to amplify the signal. As the increase in resistance value will increase the thermal noise and use of analog amplifier will amplify the noise also [39, 40]. Therefore, 2 ohm shunt resistor is used. Also, to reduce analog circuitry [6], no notch filter or anti-aliasing filter is used before a signal is fed to ADC. Figure 4.8 shows the DAQ scheme used in the experiment. Since, neither of the output from a shunt resistor is referenced to a system ground, input to the DAQ module is a floating differential signal. As practical devices have limited capability to reject common-mode voltage [38], therefore, to keep the signal with-in the common-mode range, both the +ve and –ve leads of the signal are connected to an isolated COM terminal through one mega ohm resistors [38] as shown in the Figure 4.8.

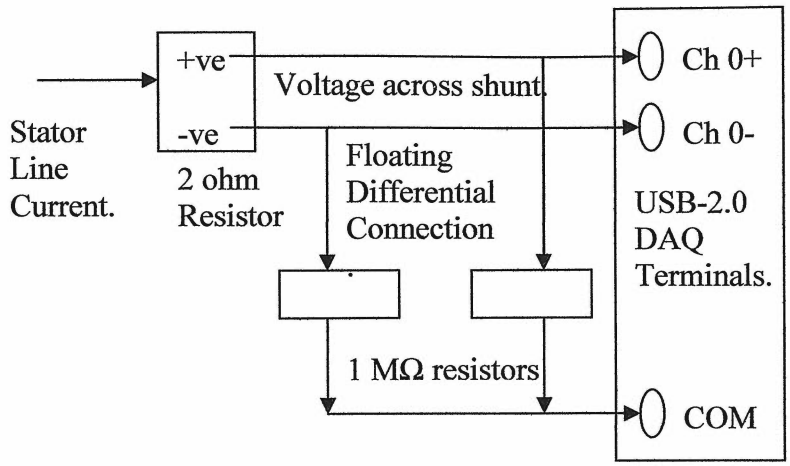

Figure 4.8: DAQ scheme for the on-line experimental set-up.

4.4 Block Diagram: Sensor-Less Speed Detection

Figure 4.9 shows a simplified block diagram for both off-line and on-line sensor-less speed detection utilizing MCSA technique [32-35]:

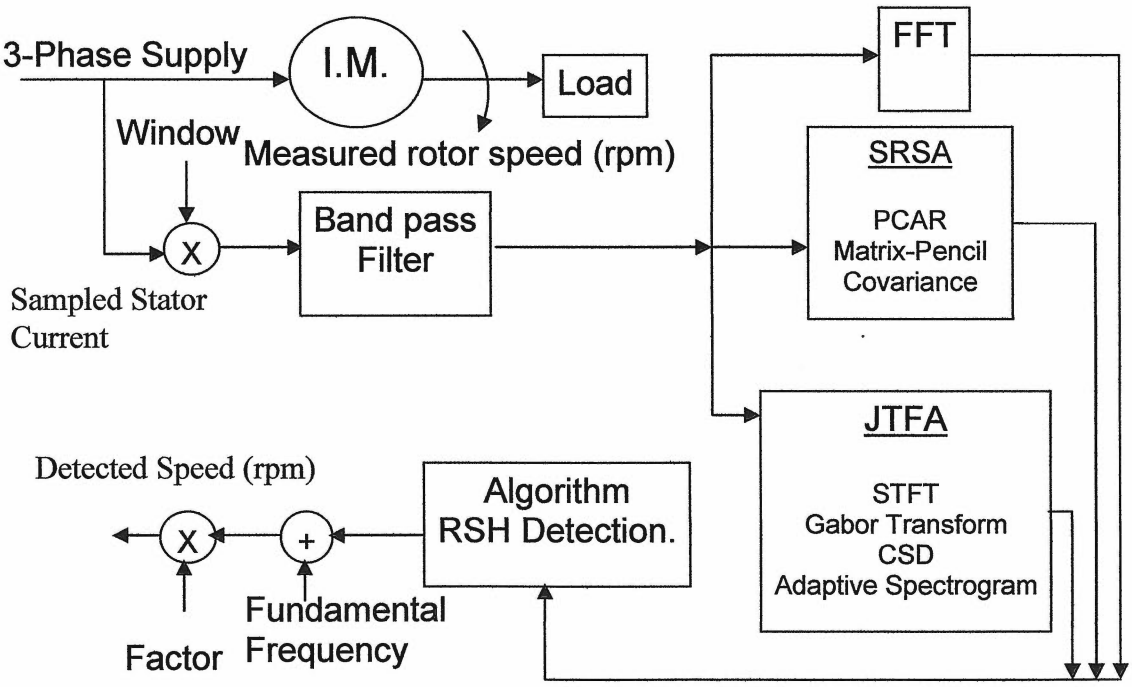

Figure 4.9: Simplified block-diagram for sensor-less speed detection algorithm.

4.5 PC-Based Implementation

The sensor-less speed detection algorithm described above was implemented in real-time using LabView 7.1 software and its advanced signal processing toolset for both off-line and on-line speed detection with the following assumptions:

i. Only harmonics due to slotting and saturation are considered. Winding and distribution factors are neglected.
ii. Inverter harmonics are neglected.
iii. Fundamental frequency is fixed at 60 Hz.
iv. Motor is operating under its rated slip range and number of rotor slots is known.

LabView is an application development software which uses a graphical programming language, also known as G programming to write codes known as block diagrams. It has all the logic features and capabilities of any other programming language such as C or Matlab [25]. But, in LabView, the application is developed by using built in VIs known as icons or blocks. LabView has a graphical user interface which is known as the front panel, in which various controls, indicators, knobs, dials, graphs and many other features can be incorporated with ease to make the application user friendly and to display useful results for analysis. LabView also has various built in libraries, VIs for data-acquisition, signal processing, statistics, waveform generation and monitoring, analysis, mathematics, logical etc. to name a few. LabView software is specifically useful for applications which require data-acquisition or instrument control and to develop real-time applications [25, 36]. The application files developed in LabView are saved with a VI extension, also known as virtual instrument. The real-time application developed using LabView for this research allows investigating dynamic behavior of all the applied spectral estimation techniques in one application. The graphical user interface (GUI) of the application allows controlling various parameters in run-time to study its effect on the performance in real-time. The PC on which this application is run in real-time is PentiumIV with 512MB RAM.

4.5.1 Off-line LabView Implementation

The data-records are collected as explained in section 4.2. The data text files are retrieved in LabView using "ReadFromSpreadsheetFile.vi". The time and amplitude values of

stator line current are stored in two sub-set arrays. The output of the sub-set arrays is read in a "For Loop" and within the "For Loop" Hanning window and Butterworth band-pass filter sub-routine is applied in the time domain to the stator line current signal. The stacked ring-type case-structures are used to implement spectral estimation sub-routines. The output of the Butterworth band-pass filter is passed to the case structures to obtain the spectrum. The peak of the spectrum is obtained by using "Max-MinArray.vi". The equation from section 4.1 to detect the speed value is solved using "FormulaNode.vi". The output of the formula node is passed to the indicators in the front panel. Figures 4.10-4.12 shows the partial view of the block-diagram as explained above.

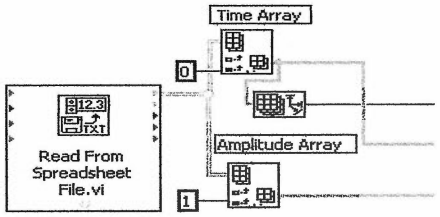

Figure 4.10: Partial view of block-diagram to read data files.

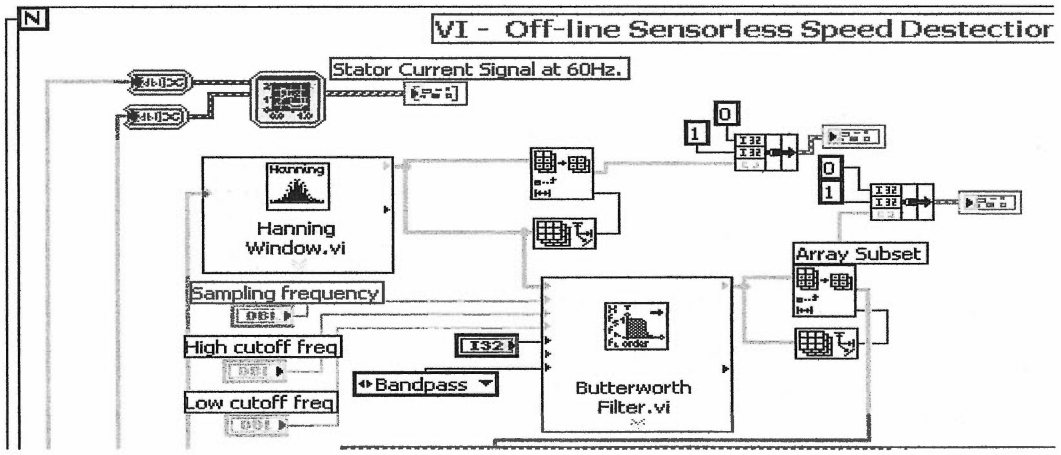

Figure 4.11: Partial view of block-diagram showing window and band-pass filter sub-routines within main "For-Loop".

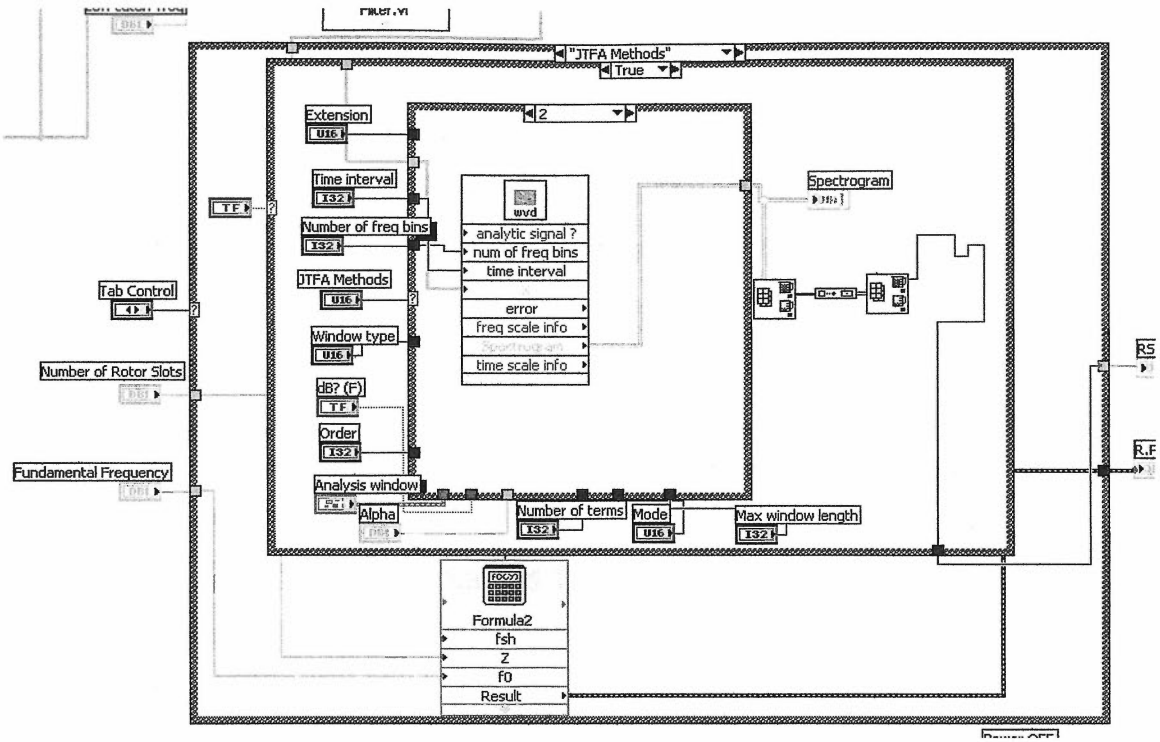

Figure 4.12: Partial view of block-diagram showing nested ring-type case-structures to implement spectral estimation sub-routines with in the "For-Loop".

4.5.2 On-Line LabView Implementation

To analyze the results as the current signal is being acquired and to prevent data from being overwritten, the circular buffer technique is employed in data-acquisition VI by using DAQmx Base VIs. The current data from the buffer is read in a main "While-Loop". Within the main "While-Loop" the block diagram is developed in a similar manner as explained in section 4.5.1. The NI USB-9215 DAQ module uses DAQmx Base driver software. Channels and tasks are two important concepts in NI-DAQmx Base [36, 38]. A physical channel is one which is used to make measurements. The virtual channels are used to encapsulate physical channels with specific information to format the data. A task represents a measurement to be performed. A task is a collection of one or more channels, timing, triggering and other properties [36, 38]. The sub-routines used for continuous data-acquisition are "DAQmx Base Create Task.vi", which creates a task, "DAQmx Base Create Virtual Channel.vi" which creates a virtual channel and add tasks to the virtual channel, "DAQmx Base Timing.vi" which configures the sampling rate and creates a buffer when needed and sets the continuous or finite samples acquisition mode,

"DAQmx Base Start Task.vi" which starts the task to begin the measurements, "DAQmx Base Read.vi" which reads the task and specifies the number of samples to read for each channel, "DAQmx Base Stop Task.vi" which stops the task and brings it back to the state before start task, "DAQmx Clear Task.vi" which clears the task and releases any resources reserved by the task, and "Config Input Buffer.vi", which is used to overwrite the default buffer size. The data-acquisition VI acquires continuous data using the DAQ device internal clock. The application reads the first half of the data from the buffer while the second half of the buffer is written with new data. The channels in NI-DAQmx Base are identified as ai0, ai1, ai2, ai3, and so on. Channel 0 is used to acquire the current signal and the naming convention is used as Dev1/ai0, i.e. device name and a slash followed by channel identifier. Figure 4.13 shows a partial view of the on-line block diagram for data-acquisition. The rest of the on-line block diagram is essentially the same as for off-line except that in on-line application block diagram the "For-Loop" is replaced by "While-Loop".

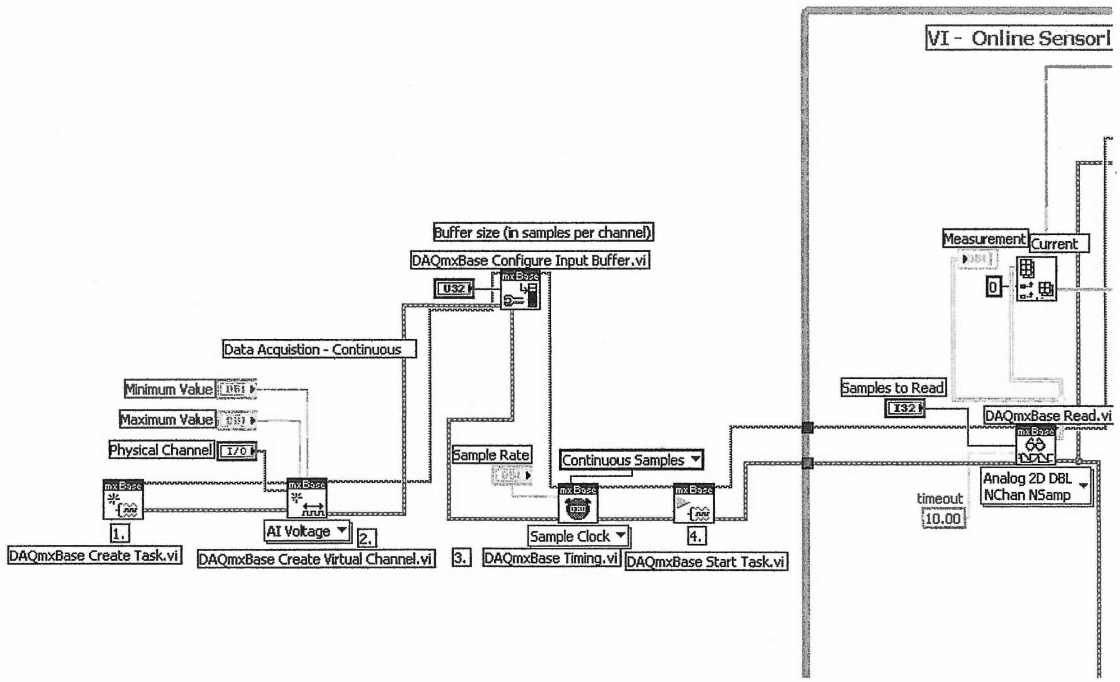

Figure 4.13: Partial view of the on-line block diagram showing continuous data-acquisition VI.

4.5.3 LabView Application Front-Panel

The front-panel for both off-line and on-line application has an interactive user interface. It enables the user to input the values of fundamental frequency, number of poles, number of rotor slots specific to an induction motor. It displays the plots of the measurement from a current transducer. It also displays windowed and band-pass filtered signal. The GUI interface of this application allows a user to select the type of spectral estimation method desired and displays the corresponding spectrum. It has dial and numeric indicators that display rotor speed and RSH frequency. It enables the user to see changes in the above parameters in real-time as the load is being varied. In addition to that, it has control for buffer size, sampling rate, and number of samples to read. It also has control for band-pass filter to select filter order and band-pass frequencies. The GUI of the application has controls for parameters specific to the spectral estimation technique that enables the user to vary different parameters to study the effect on performance in real-time. This application allows investigating the dynamic behavior of the applied techniques in real-time. Figure 4.14 shows a view of the front-panel common to both off-line and on-line application.

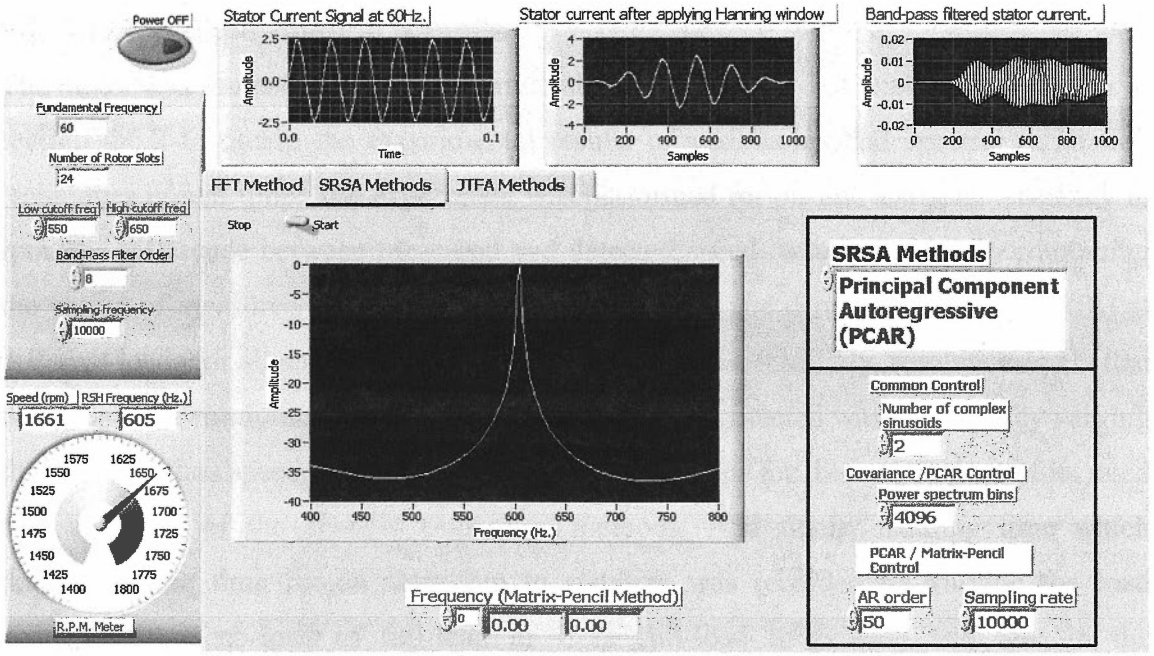

Figure 4.14: Front-panel view common to both off-line and on-line application.

Chapter 5: Experimental Results and Discussion

5.1 Off-Line Simulations and Results

The motor was run at different loads to acquire stator line current 30 cycle data-records at a sampling frequency of 4 kHz. and 6 cycle data-records at a sampling frequency of 10 kHz. at load torque of 0.06, 0.1, 0.2, 0.4, 0.6, 0.8, 1.0, and 1.2 Nm, in real-time, for off-line speed detection. Figure 5.1 to Figure 5.7 show spectra of band-passed signals using various spectrum estimation techniques at a light load of 0.06 Nm and full load of 1.2 Nm. At light load, the calculated RSH is equal to 641Hz. and the full load calculated RSH is 557 Hz. In a similar manner, spectra were obtained at all the above values of load. Figures 5.8 to 5.10 show results and plots of measured speed vs. off-line detected speed in rpm at different levels of load for FFT, Model-Based methods and JTFA methods respectively for 30 cycle data at a sampling frequency of 4 kHz. Figure 5.11 shows results and a plot of measured speed vs. off-line detected speed in rpm at various load levels for model-based methods for 6 cycle data at a sampling frequency of 10 kHz.

5.2 On-Line Experimental Results

The motor was run and a stator line current signal was acquired as explained in chapter 4, section 4.5.2 to obtain the experimental results of various applied spectral estimation techniques in real-time. The experiment was performed for on-line analysis. Accuracy in rpm, the difference between measured and detected speed, was measured by comparing the values of measured speed with a digital tachometer and detected speed from RSH at different loads for all applied spectral estimation methods. Similarly, resolution in Hz that determines the minimum change in speed which can be detected was observed by varying the load and thus speed, very gradually in very short steps for the entire range of its rated slip, for each of the spectral estimation methods. And finally, settling time which determines the time for an algorithm to stabilize was recorded by varying the load suddenly from no-load to full-load or from full-load to no-load and also in the intermediate ranges for each of the spectral estimation methods. All the above readings were taken for different numbers of cycles at various sampling frequencies to determine

which technique works best under what conditions.

The number of cycles, at various sampling frequencies, is determined and governed by the following relation:

$$\text{Number of cycles} = \frac{\text{Number of samples}}{\text{Samples per second}} \times 60, \text{ where } 60 = \text{fundamental frequency.}$$

The table 5.1 shows the numbers of data-samples required to get the desired number of cycles for each sampling frequency, as used in this experiment.

Table 5.1: Number of data-samples required to get the desired number of cycles at different sampling frequencies.

Sampling Frequency / Number of cycles	2 kHz.	4 kHz.	8 kHz.
6 cycles	200	400	800
9 cycles	300	500	1200
15 cycles	500	1000	2000
30 cycles	1000	2000	4000
60 cycles	2000	4000	8000
120 cycles	4000	8000	16,000

The on-line experimental results and plots are shown in Figure 5.12 to 5.21 in terms of accuracy, resolution and settling time with regard to different data record lengths at various sampling frequencies. As seen from off-line results in Figure 5.10, JTFA methods performed poorly in terms of accuracy with accuracy error in the range of 35 to 45 rpm, therefore, only some results in terms of resolution and an estimated settling time were obtained for JTFA methods to overview the performance.

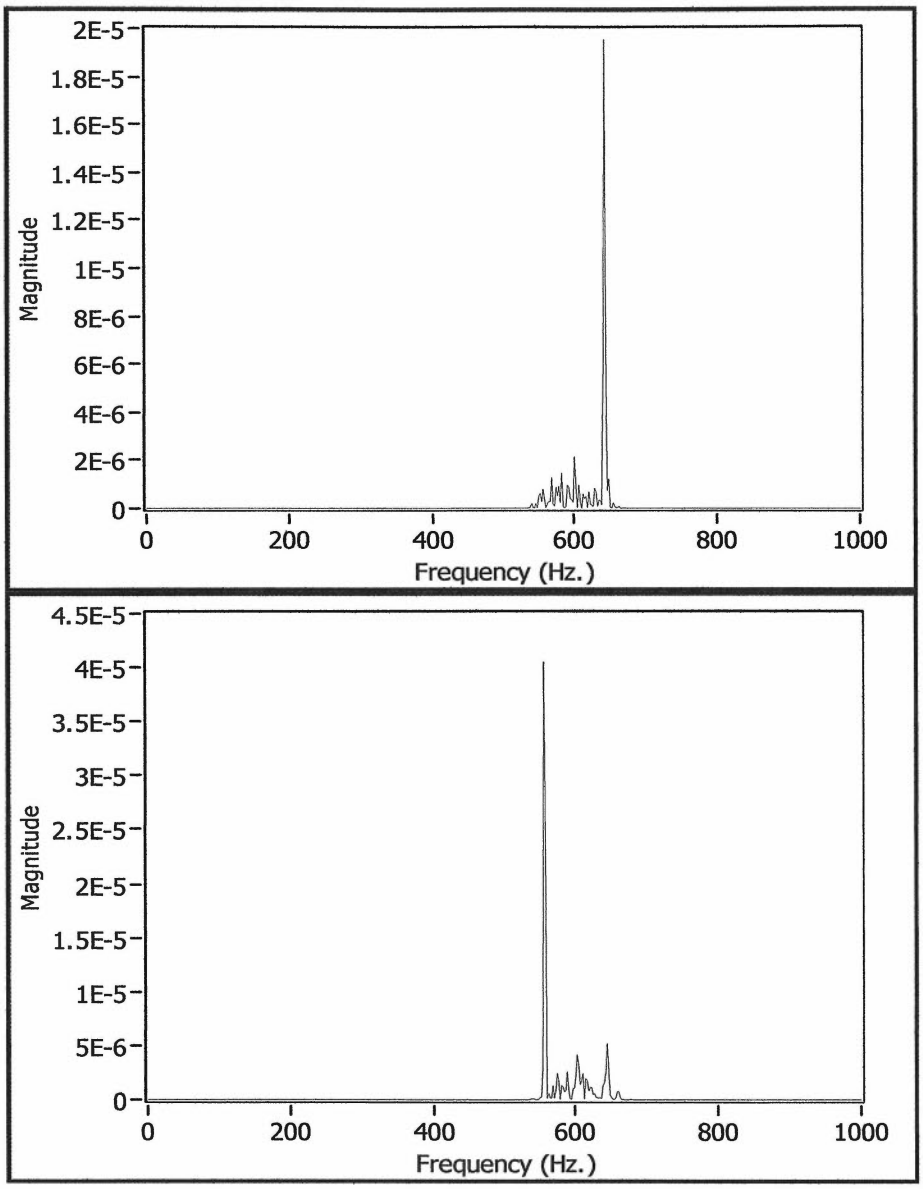

Figure 5.1: FFT spectrum of band-passed current signal at a light load torque of 0.06 Nm (top) and a full load torque of 1.2Nm (bottom).

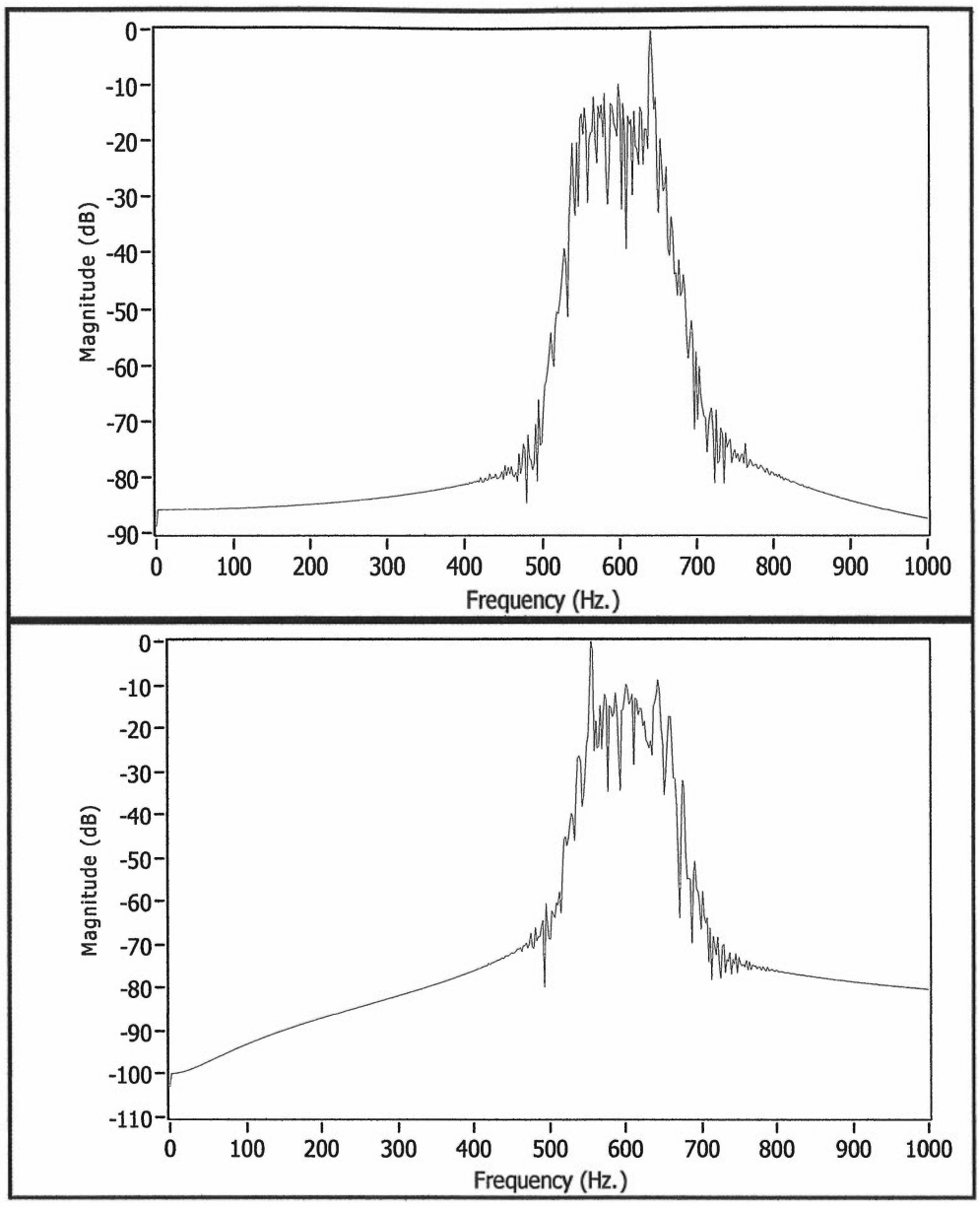

Figure 5.2: Covariance spectrum of band-passed current signal at a light load torque of 0.06 Nm (top) and a full load torque of 1.2Nm (bottom).

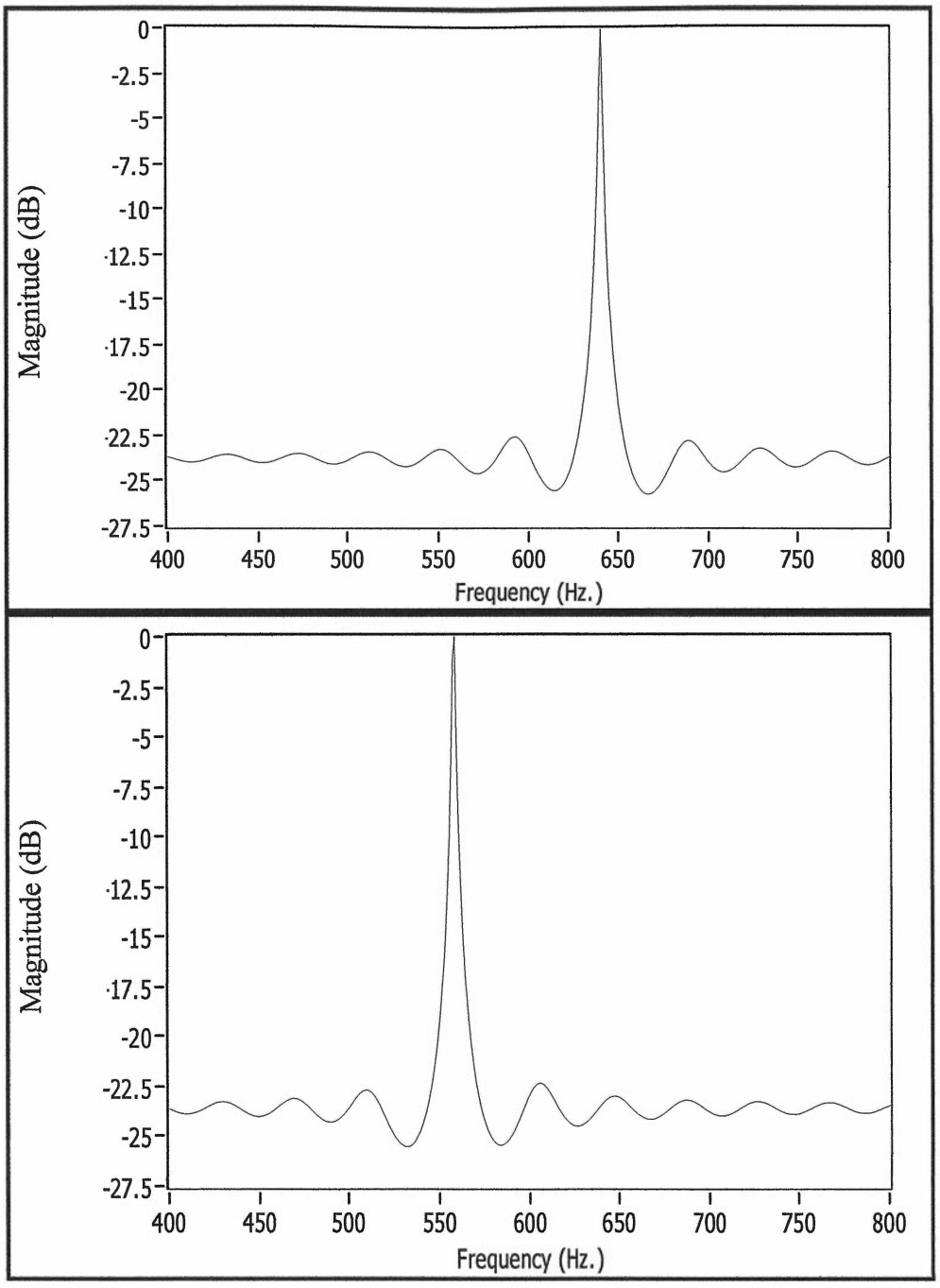

Figure 5.3: PCAR spectrum of band-passed current signal at a light load torque of 0.06 Nm (top) and a full load torque of 1.2Nm (bottom).

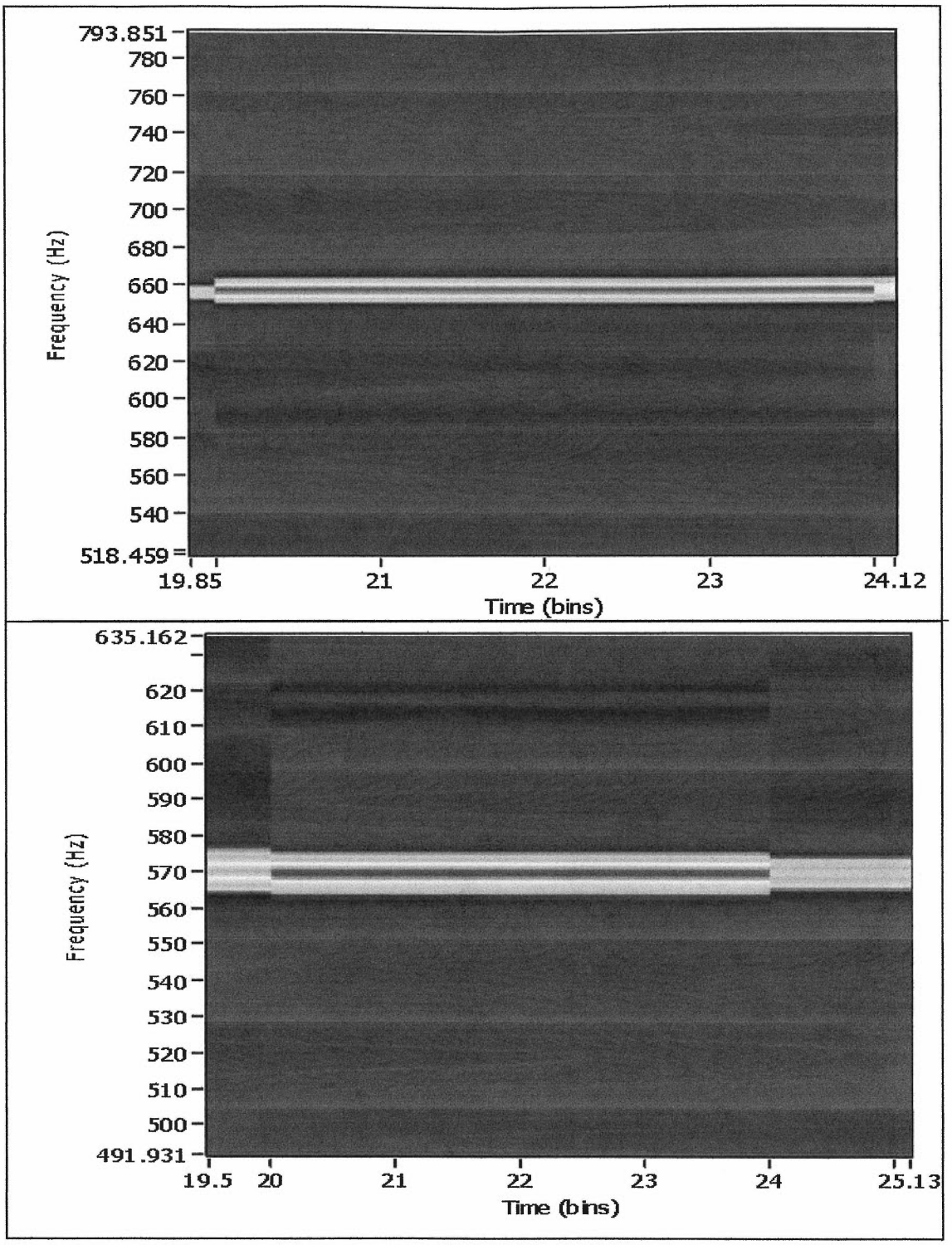

Figure 5.4: STFT spectrogram of band-passed current signal at a light load torque of 0.06 Nm (top) and a full load torque of 1.2Nm (bottom).

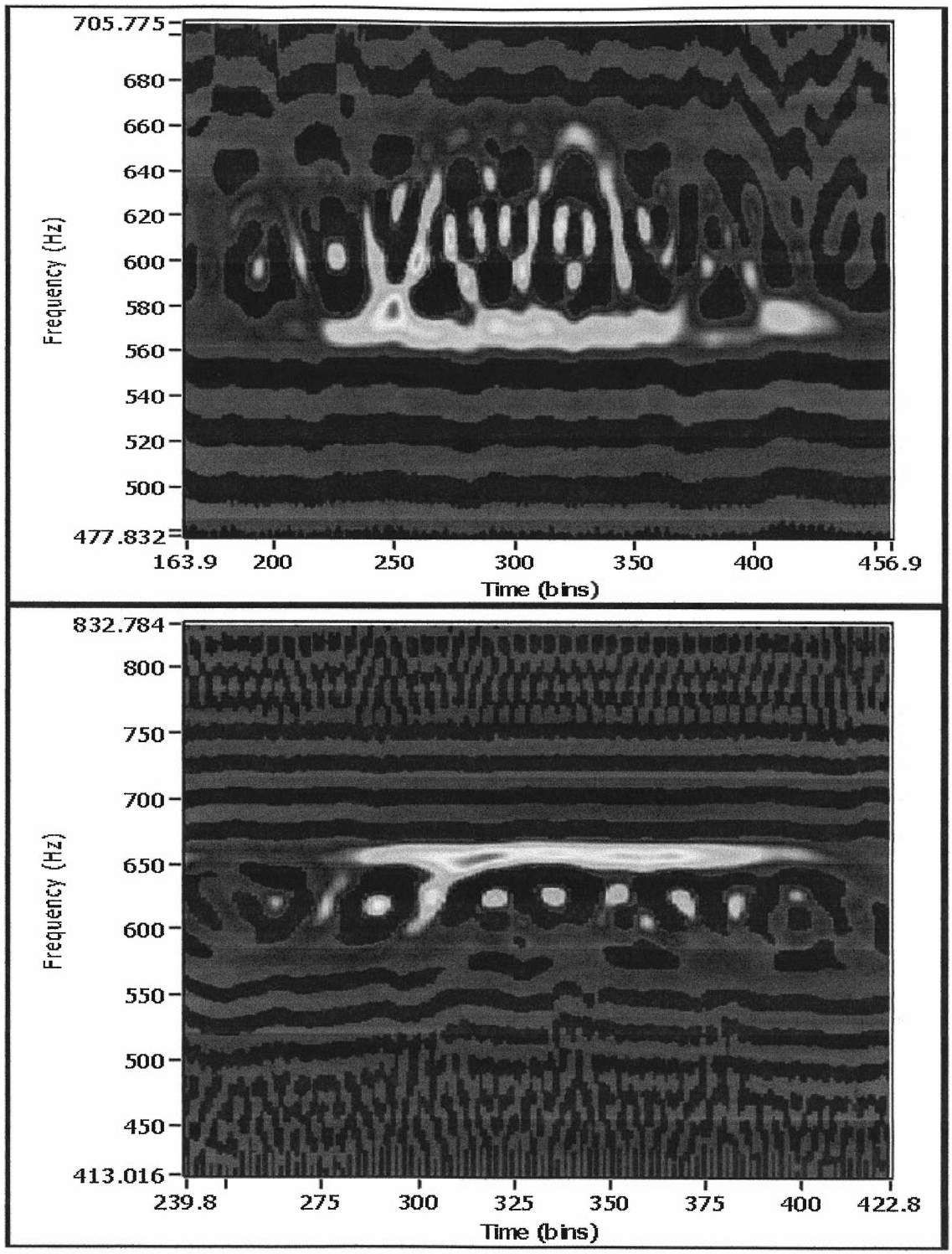

Figure 5.5: Gabor spectrogram of band-passed current signal at a light load torque of 0.06 Nm (top) and a full load torque of 1.2Nm (bottom).

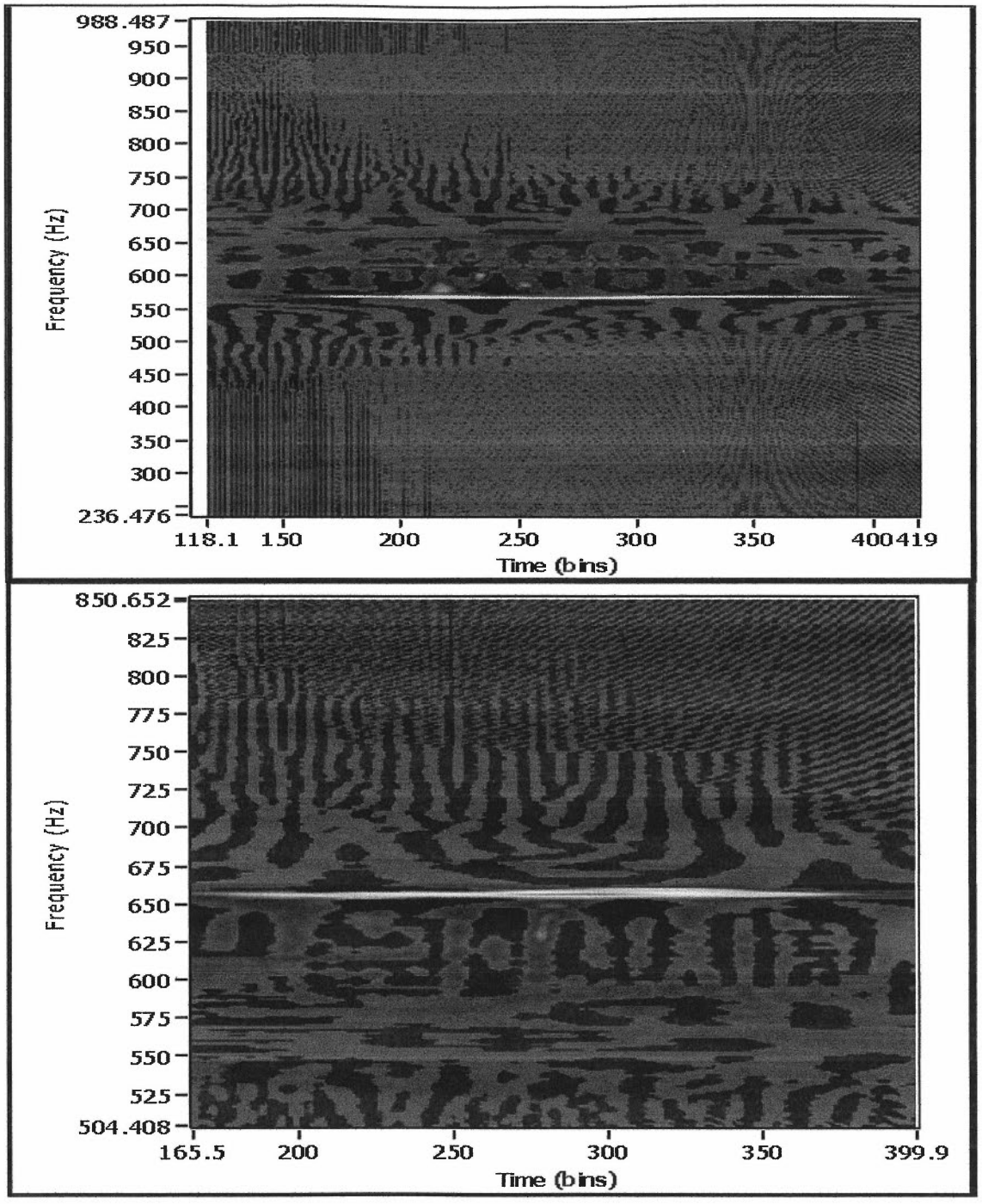

Figure 5.6: CSD spectrogram of band-passed current signal at a light load torque of 0.06 Nm (top) and a full load torque of 1.2Nm (bottom).

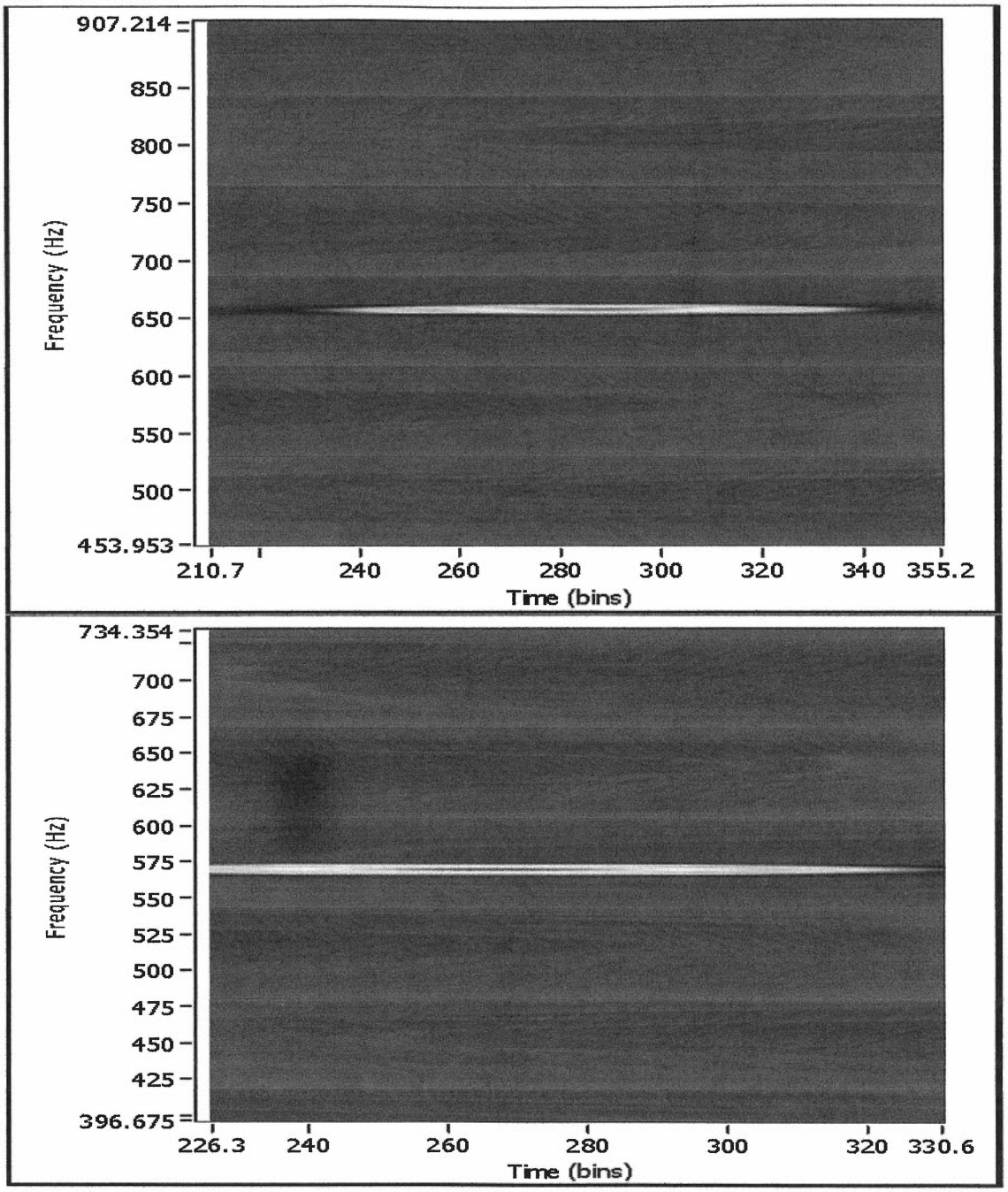

Figure 5.7: Adaptive spectrogram of band-passed current signal at a light load torque of 0.06 Nm (top) and a full load torque of 1.2Nm (bottom).

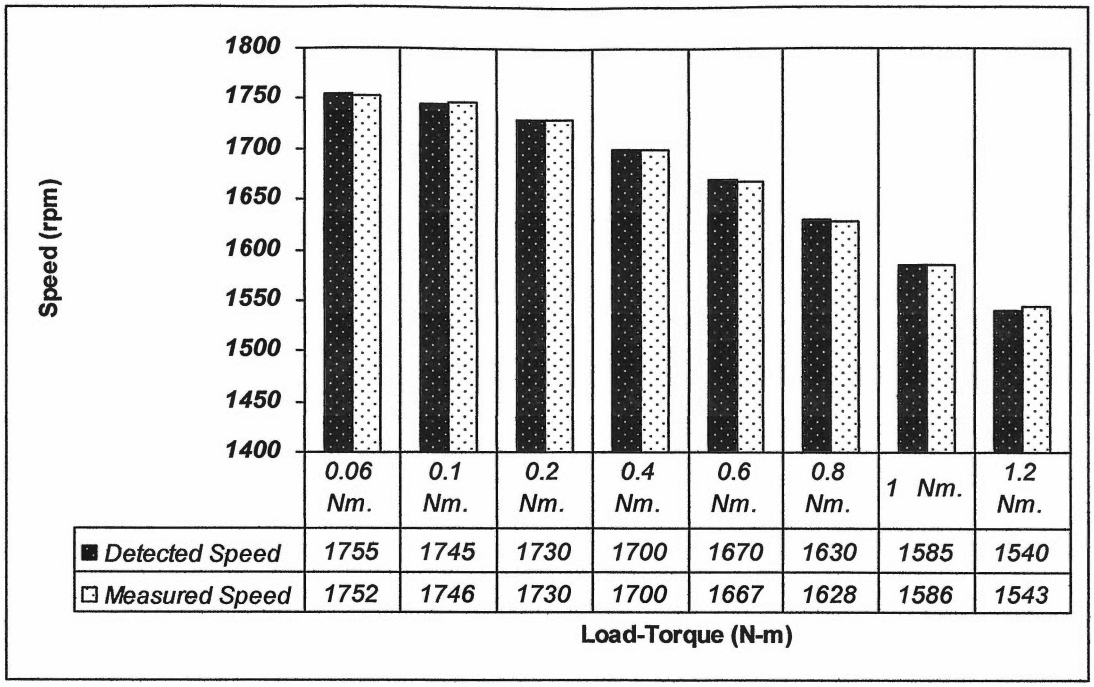

	0.06 Nm.	0.1 Nm.	0.2 Nm.	0.4 Nm.	0.6 Nm.	0.8 Nm.	1 Nm.	1.2 Nm.
Detected Speed	1755	1745	1730	1700	1670	1630	1585	1540
Measured Speed	1752	1746	1730	1700	1667	1628	1586	1543

Figure 5.8: Results and plot of measured speed and off-line detected speed in rpm vs. load torque in Nm. – FFT method, 30 cycle data, and sampling frequency 4 kHz.

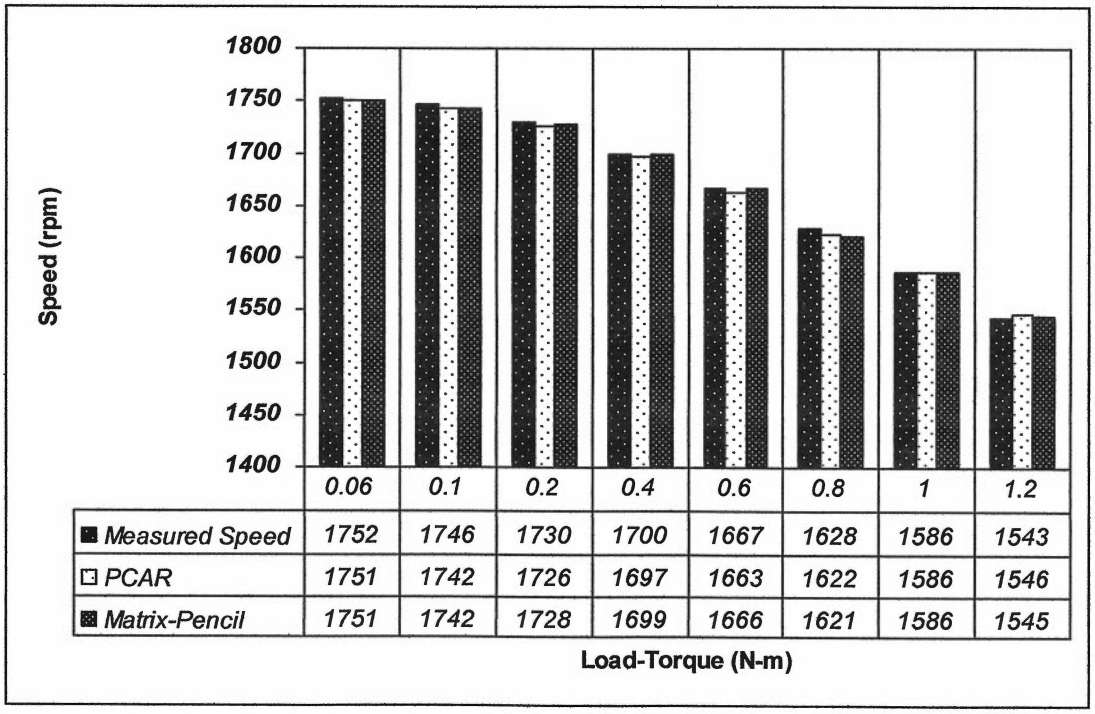

	0.06	0.1	0.2	0.4	0.6	0.8	1	1.2
Measured Speed	1752	1746	1730	1700	1667	1628	1586	1543
PCAR	1751	1742	1726	1697	1663	1622	1586	1546
Matrix-Pencil	1751	1742	1728	1699	1666	1621	1586	1545

Figure 5.9: Results and plot of measured speed and off-line detected speed in rpm vs. load torque in Nm. – model-based methods, 6 cycle data, and sampling frequency 10 kHz.

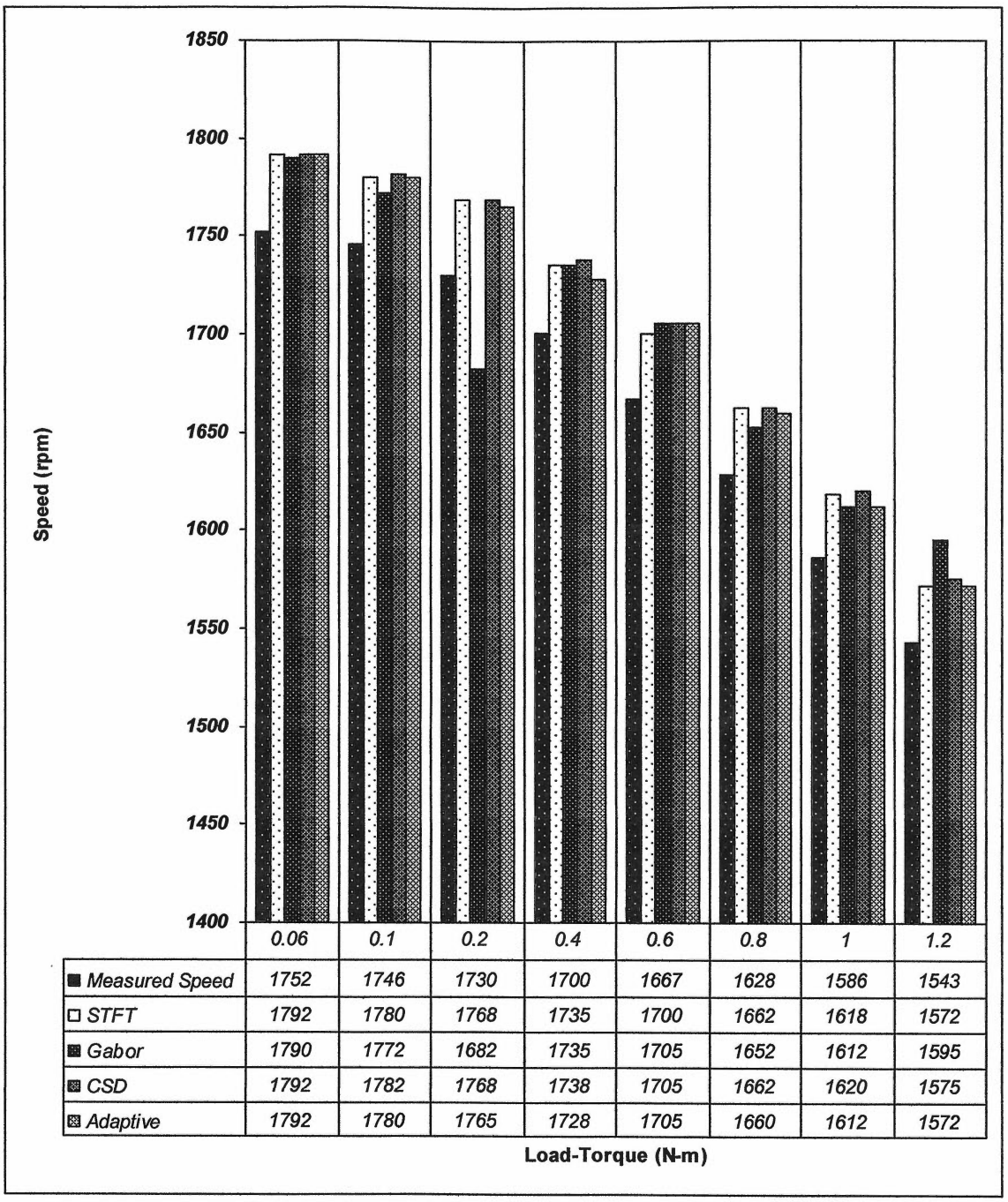

	0.06	0.1	0.2	0.4	0.6	0.8	1	1.2
Measured Speed	1752	1746	1730	1700	1667	1628	1586	1543
STFT	1792	1780	1768	1735	1700	1662	1618	1572
Gabor	1790	1772	1682	1735	1705	1652	1612	1595
CSD	1792	1782	1768	1738	1705	1662	1620	1575
Adaptive	1792	1780	1765	1728	1705	1660	1612	1572

Load-Torque (N-m)

Figure 5.10: Results and plot of measured speed and off-line detected speed in rpm vs. load torque in Nm. – JTFA methods, 30 cycle data, and sampling frequency 4 kHz.

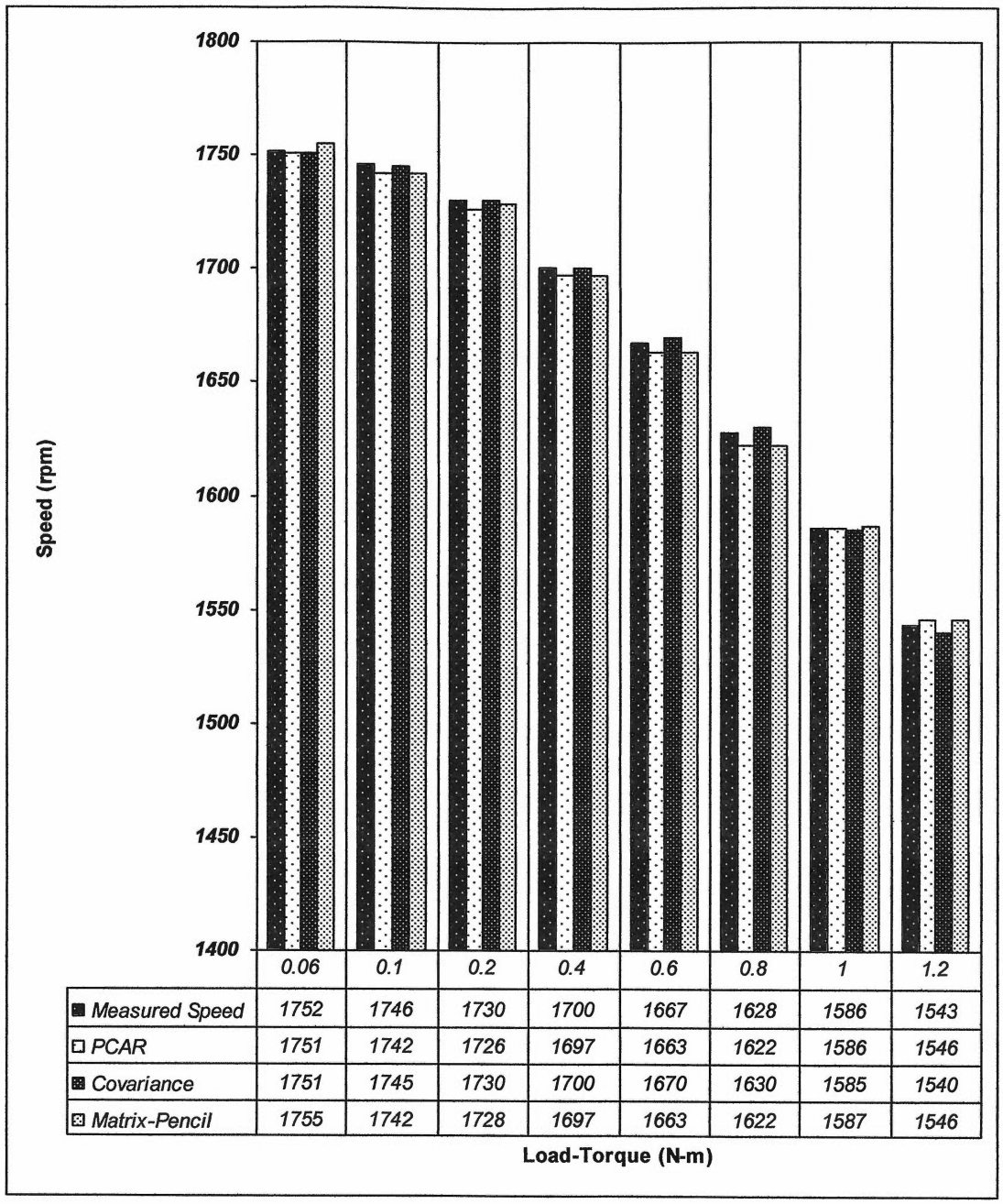

	0.06	0.1	0.2	0.4	0.6	0.8	1	1.2
Measured Speed	1752	1746	1730	1700	1667	1628	1586	1543
PCAR	1751	1742	1726	1697	1663	1622	1586	1546
Covariance	1751	1745	1730	1700	1670	1630	1585	1540
Matrix-Pencil	1755	1742	1728	1697	1663	1622	1587	1546

Figure 5.11: Results and plot of measured speed and off-line detected speed in rpm vs. load torque in Nm. – model-based methods, 30 cycle data, and sampling frequency 4 kHz.

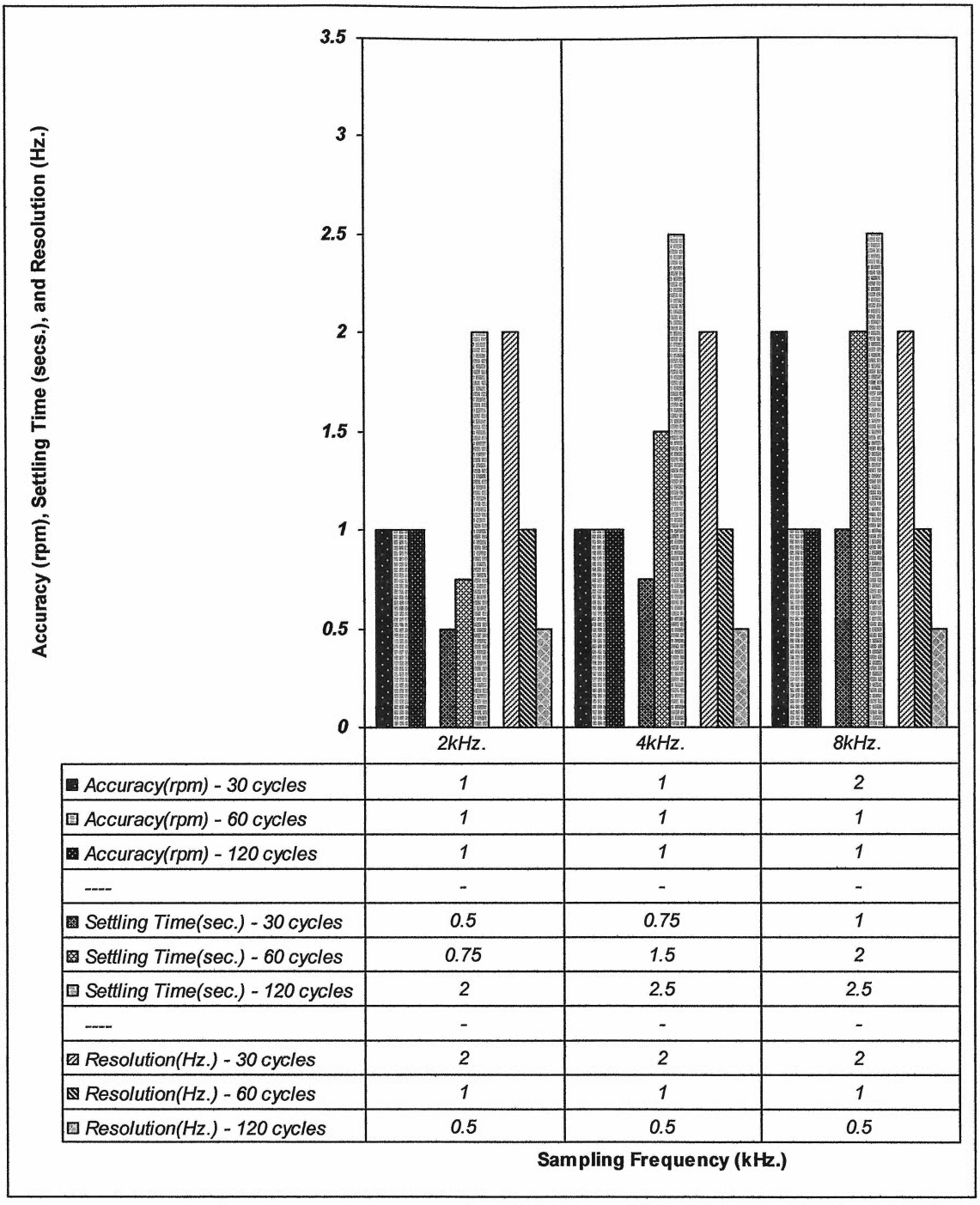

	2kHz.	4kHz.	8kHz.
Accuracy(rpm) - 30 cycles	1	1	2
Accuracy(rpm) - 60 cycles	1	1	1
Accuracy(rpm) - 120 cycles	1	1	1
----	-	-	-
Settling Time(sec.) - 30 cycles	0.5	0.75	1
Settling Time(sec.) - 60 cycles	0.75	1.5	2
Settling Time(sec.) - 120 cycles	2	2.5	2.5
----	-	-	-
Resolution(Hz.) - 30 cycles	2	2	2
Resolution(Hz.) - 60 cycles	1	1	1
Resolution(Hz.) - 120 cycles	0.5	0.5	0.5

Figure 5.12: On-line results and plots of error in rpm, settling time in seconds, and resolution in Hz for 30, 60, and 120 cycles of current data at sampling frequencies of 2, 4, and 8kHz. – FFT method.

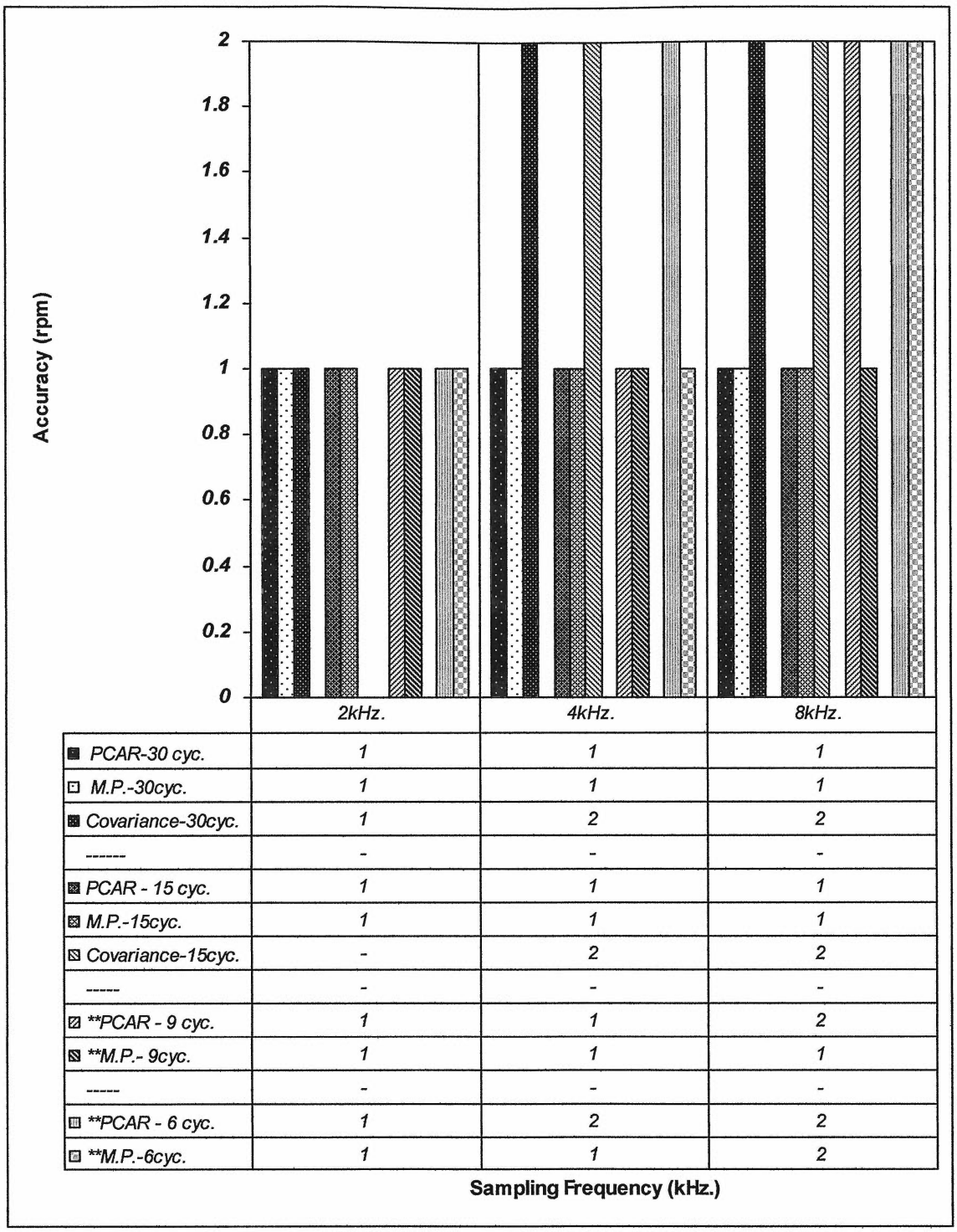

	2kHz.	4kHz.	8kHz.
PCAR-30 cyc.	1	1	1
M.P.-30cyc.	1	1	1
Covariance-30cyc.	1	2	2
-------	-	-	-
PCAR - 15 cyc.	1	1	1
M.P.-15cyc.	1	1	1
Covariance-15cyc.	-	2	2
-----	-	-	-
**PCAR - 9 cyc.	1	1	2
**M.P.- 9cyc.	1	1	1
-----	-	-	-
**PCAR - 6 cyc.	1	2	2
**M.P.-6cyc.	1	1	2

** This data is from medium-load to full-load: Refer to section 5.3.2 for details.

Figure 5.13: On-line results and plots of error in rpm for 30, 15, 9 and 6 cycles of current data at sampling frequencies of 2, 4, and 8 kHz. – Model-Based methods (PCAR, M.P. and Covariance).

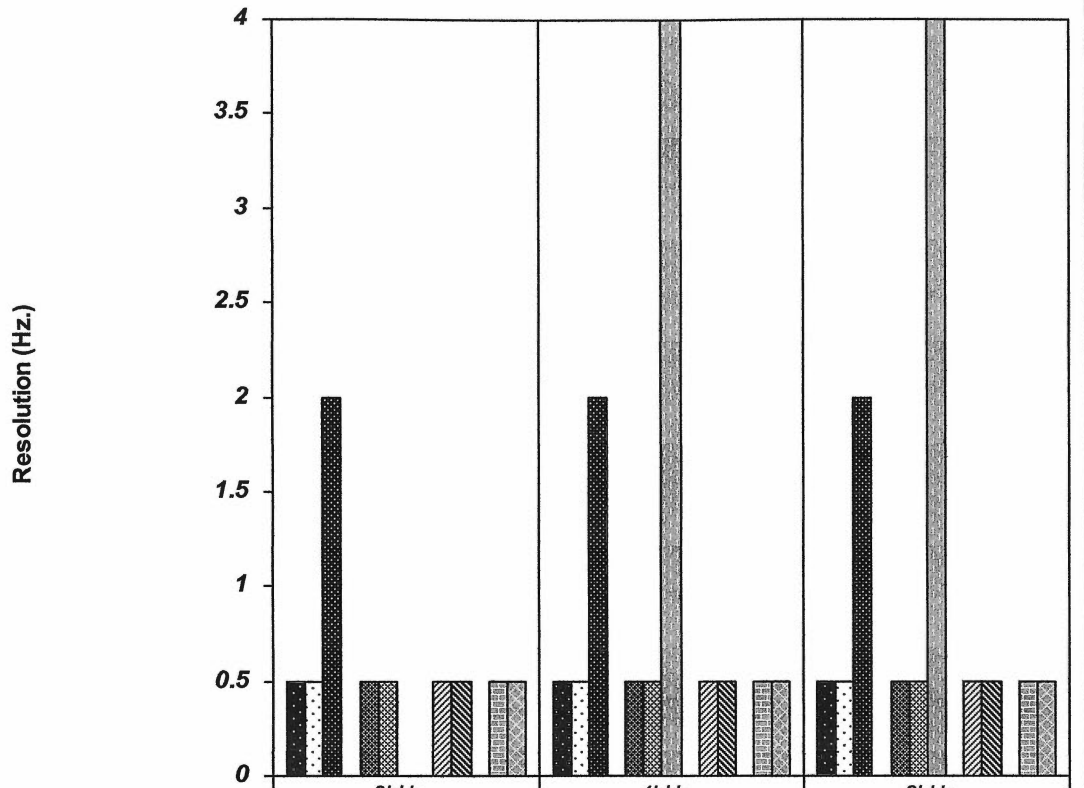

	2kHz.	4kHz.	8kHz.
PCAR-30 cyc.	0.5	0.5	0.5
M.P.-30cyc.	0.5	0.5	0.5
Covariance-30cyc.	2	2	2
-----	-	-	-
PCAR-15 cyc.	0.5	0.5	0.5
M.P.-15cyc.	0.5	0.5	0.5
Covariance-15cyc.	-	4	4
-------	-	-	-
**PCAR-9cyc.	0.5	0.5	0.5
**M.P.-9cyc.	0.5	0.5	0.5
-------	-	-	-
**PCAR-6 cyc.	0.5	0.5	0.5
**M.P.-6cyc.	0.5	0.5	0.5

** This data is from medium-load to full-load: Refer to section 5.3.2 for details.

Figure 5.14: On-line results and plots of resolution in Hz. for 30, 15, 9 and 6 cycles of current data at sampling frequencies of 2, 4, and 8 kHz. – Model-Based methods (PCAR, M.P. and Covariance).

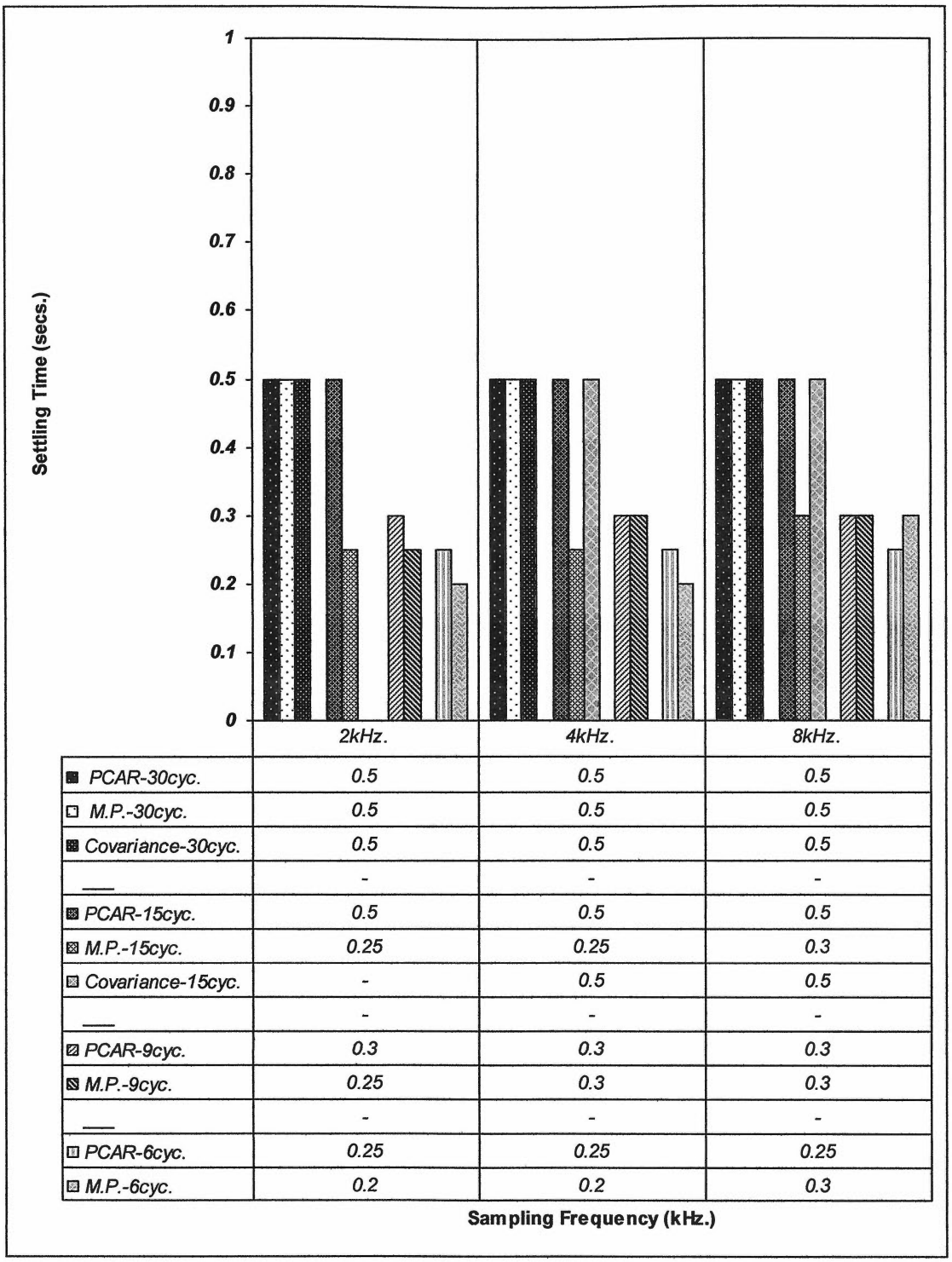

	2kHz.	4kHz.	8kHz.
PCAR-30cyc.	0.5	0.5	0.5
M.P.-30cyc.	0.5	0.5	0.5
Covariance-30cyc.	0.5	0.5	0.5
___	-	-	-
PCAR-15cyc.	0.5	0.5	0.5
M.P.-15cyc.	0.25	0.25	0.3
Covariance-15cyc.	-	0.5	0.5
___	-	-	-
PCAR-9cyc.	0.3	0.3	0.3
M.P.-9cyc.	0.25	0.3	0.3
___	-	-	-
PCAR-6cyc.	0.25	0.25	0.25
M.P.-6cyc.	0.2	0.2	0.3

Figure 5.15: On-line results and plots of settling-time in seconds for 30, 15, 9, and 6 cycles of current data at sampling frequencies of 2, 4, and 8 kHz. – Model-Based methods (PCAR, M.P. and Covariance).

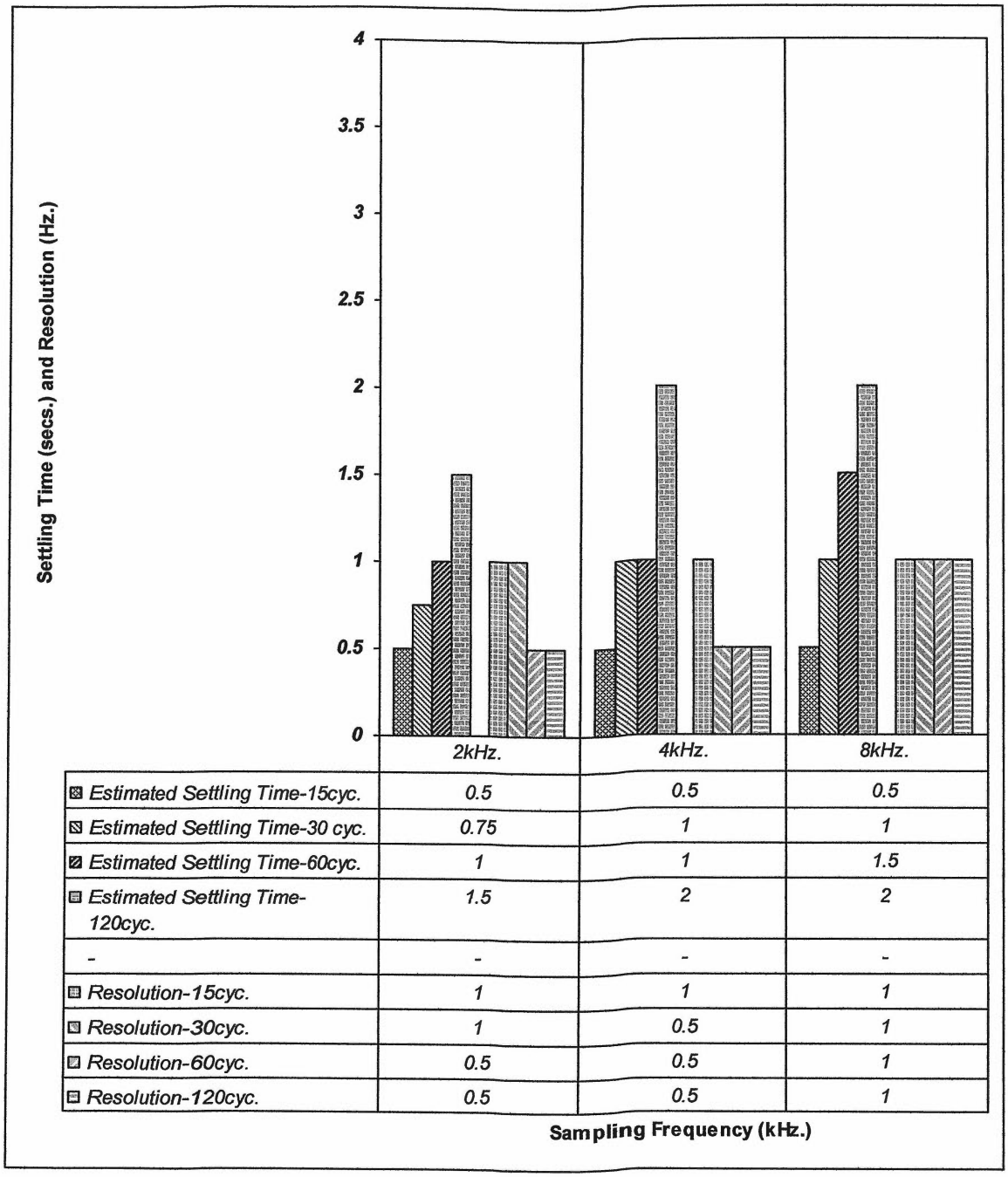

	2kHz.	4kHz.	8kHz.
Estimated Settling Time-15cyc.	0.5	0.5	0.5
Estimated Settling Time-30 cyc.	0.75	1	1
Estimated Settling Time-60cyc.	1	1	1.5
Estimated Settling Time-120cyc.	1.5	2	2
-	-	-	-
Resolution-15cyc.	1	1	1
Resolution-30cyc.	1	0.5	1
Resolution-60cyc.	0.5	0.5	1
Resolution-120cyc.	0.5	0.5	1

Figure 5.16: On-line results and plots of settling-time in seconds and resolution in Hz. for 15, 30, 60 and 120 cycles of current data at sampling frequencies of 2, 4 and 8 kHz. – STFT method, window length = 200.

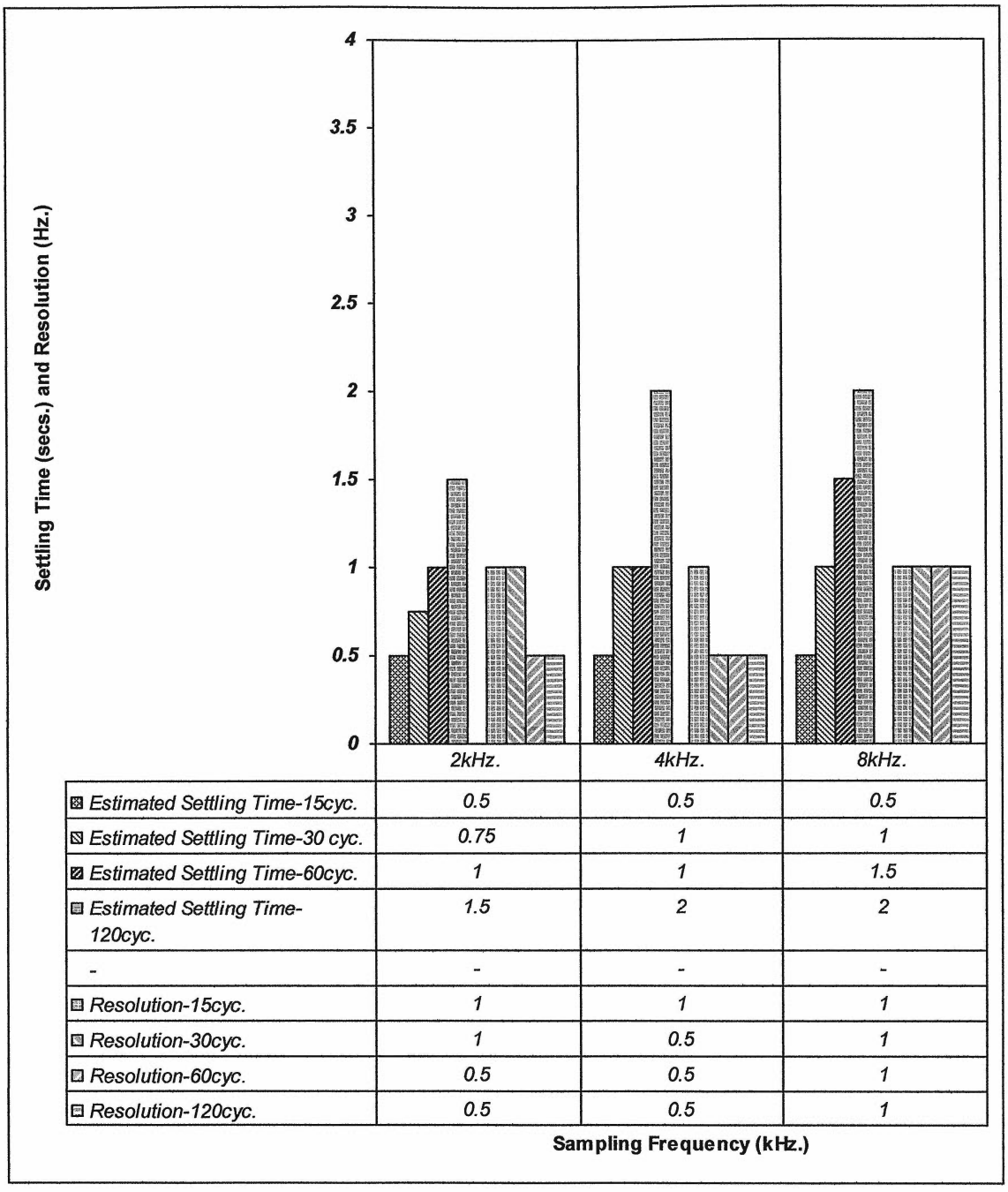

	2kHz.	4kHz.	8kHz.
Estimated Settling Time-15cyc.	0.5	0.5	0.5
Estimated Settling Time-30 cyc.	0.75	1	1
Estimated Settling Time-60cyc.	1	1	1.5
Estimated Settling Time-120cyc.	1.5	2	2
-	-	-	-
Resolution-15cyc.	1	1	1
Resolution-30cyc.	1	0.5	1
Resolution-60cyc.	0.5	0.5	1
Resolution-120cyc.	0.5	0.5	1

Figure 5.16: On-line results and plots of settling-time in seconds and resolution in Hz. for 15, 30, 60 and 120 cycles of current data at sampling frequencies of 2, 4 and 8 kHz. – STFT method, window length = 200.

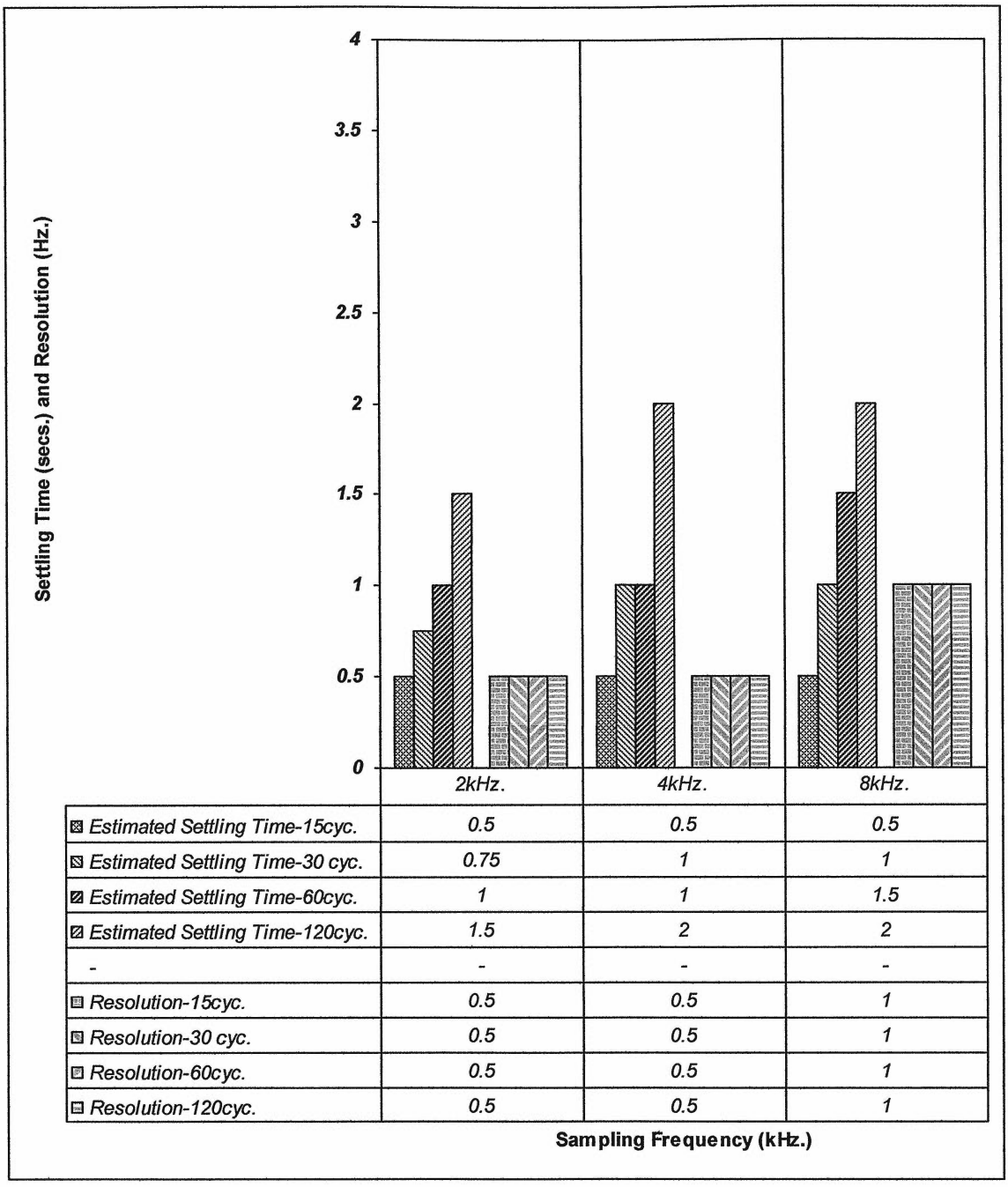

	2kHz.	4kHz.	8kHz.
Estimated Settling Time-15cyc.	0.5	0.5	0.5
Estimated Settling Time-30 cyc.	0.75	1	1
Estimated Settling Time-60cyc.	1	1	1.5
Estimated Settling Time-120cyc.	1.5	2	2
-	-	-	-
Resolution-15cyc.	0.5	0.5	1
Resolution-30 cyc.	0.5	0.5	1
Resolution-60cyc.	0.5	0.5	1
Resolution-120cyc.	0.5	0.5	1

Figure 5.17: On-line results and plots of settling-time in seconds and resolution in Hz. for 15, 30, 60 and 120 cycles of current data at sampling frequencies of 2, 4 and 8 kHz. – STFT method, window length = 800.

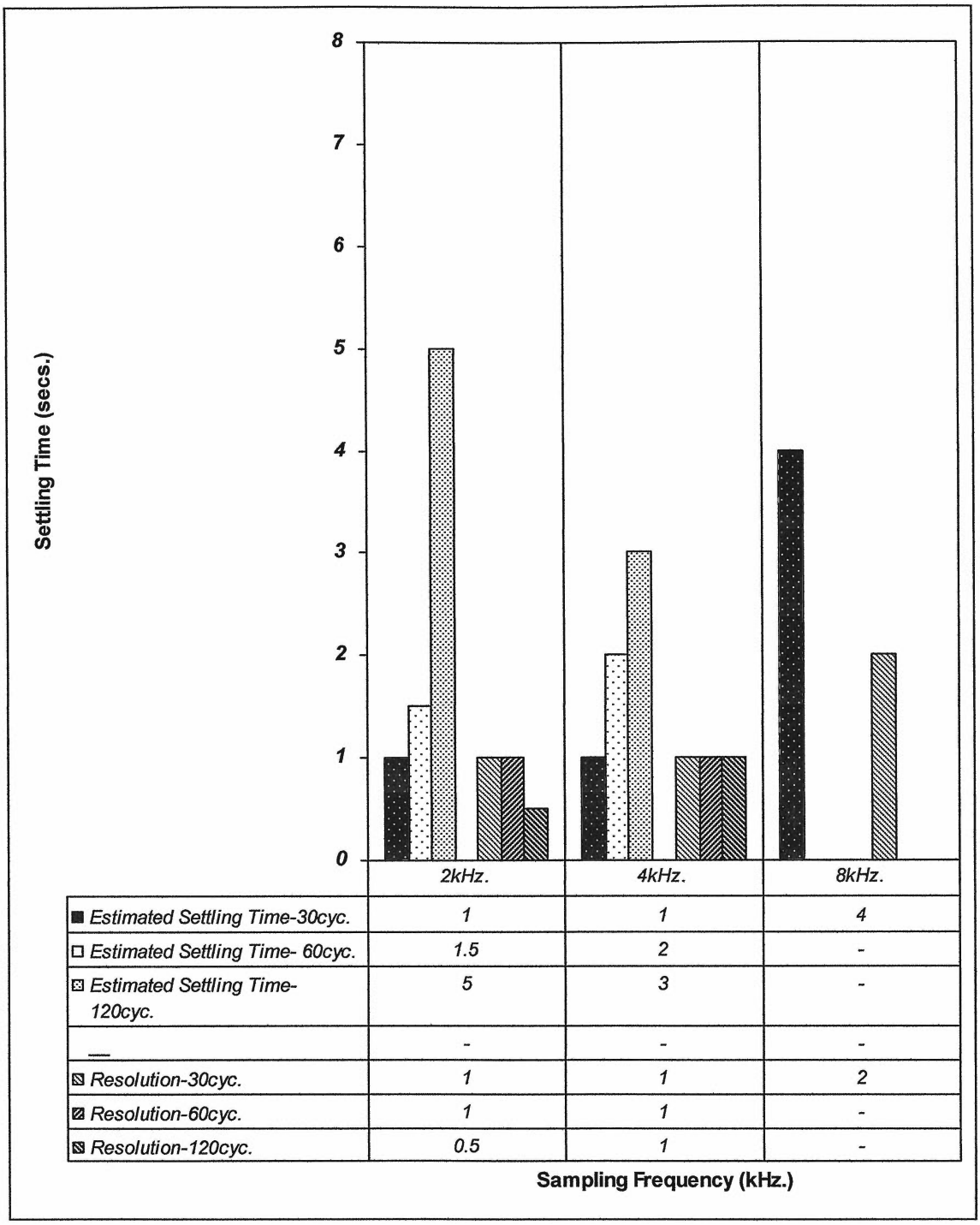

	2kHz.	4kHz.	8kHz.
■ *Estimated Settling Time-30cyc.*	1	1	4
□ *Estimated Settling Time- 60cyc.*	1.5	2	-
▨ *Estimated Settling Time-120cyc.*	5	3	-
—	-	-	-
▧ *Resolution-30cyc.*	1	1	2
▨ *Resolution-60cyc.*	1	1	-
▧ *Resolution-120cyc.*	0.5	1	-

Figure 5.18: On-line results and plots of settling-time in seconds and resolution in Hz. for 30, 60 and 120 cycles of current data at sampling frequencies of 2, 4, and 8 kHz. – Gabor Transform, order = 2.

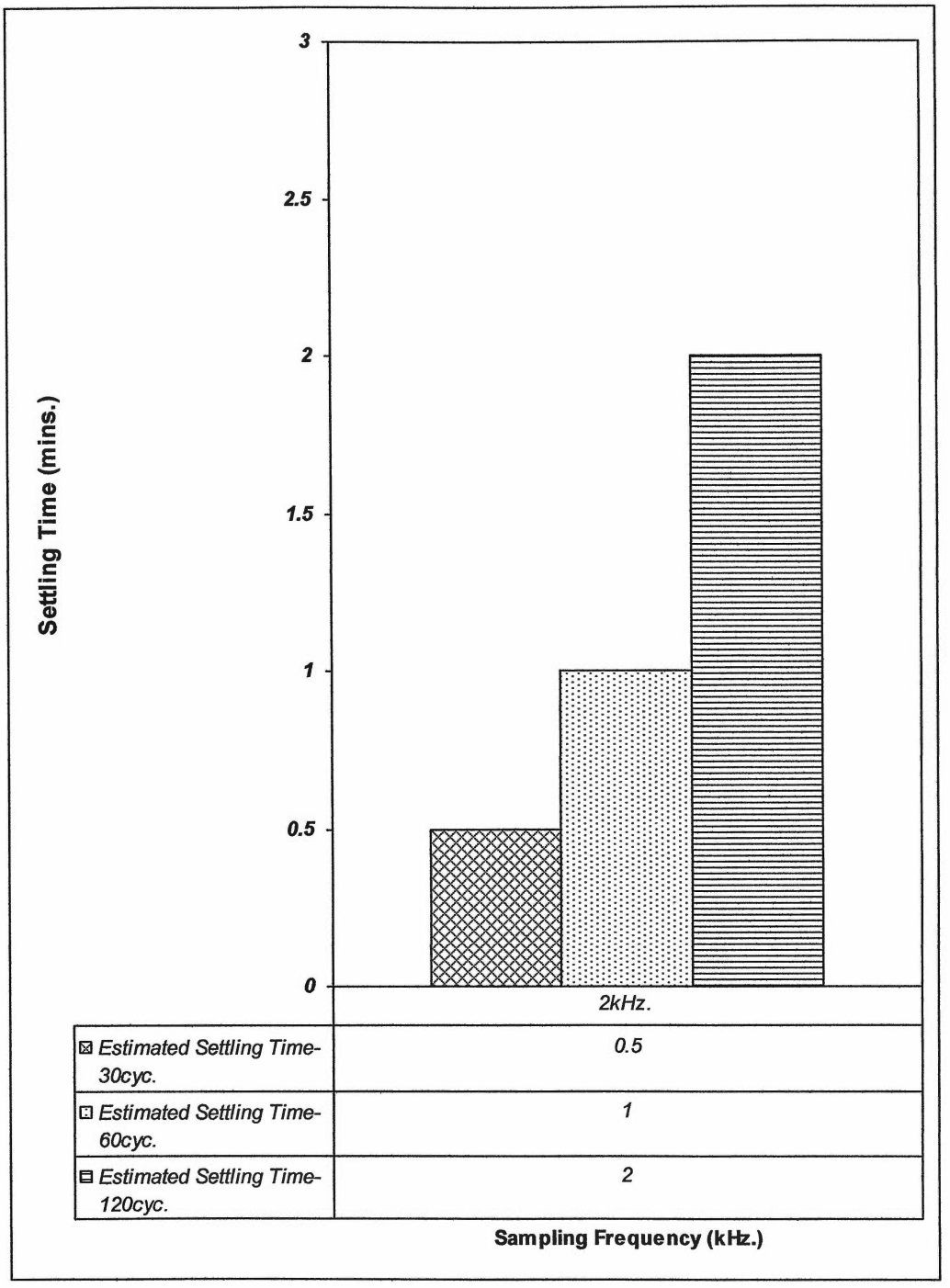

Figure 5.19: On-line results and plots of settling-time in minutes for 30, 60 and 120 cycles of current data at a sampling frequency of 2 kHz. – Gabor Transform, order = 10.

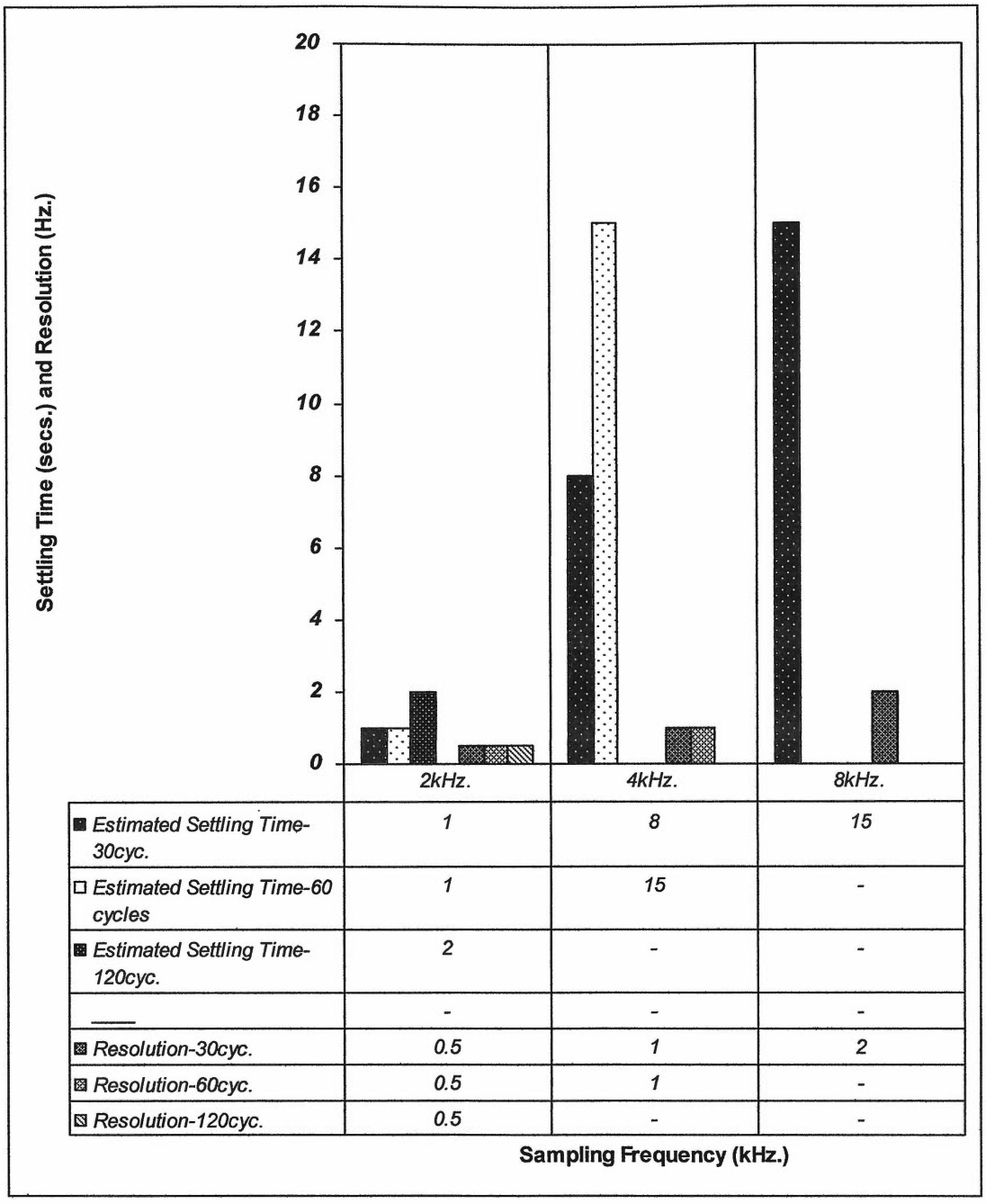

	2kHz.	4kHz.	8kHz.
■ *Estimated Settling Time-30cyc.*	*1*	*8*	*15*
□ *Estimated Settling Time-60 cycles*	*1*	*15*	-
▩ *Estimated Settling Time-120cyc.*	*2*	-	-
___	-	-	-
▩ *Resolution-30cyc.*	*0.5*	*1*	*2*
▩ *Resolution-60cyc.*	*0.5*	*1*	-
▧ *Resolution-120cyc.*	*0.5*	-	-

Figure 5.20: On-line results and plots of settling-time in seconds and resolution in Hz. for 30, 60 and 120 cycles of current data at sampling frequencies of 2, 4, and 8 kHz. – Cone-shaped Distribution, alpha = 1E-6.

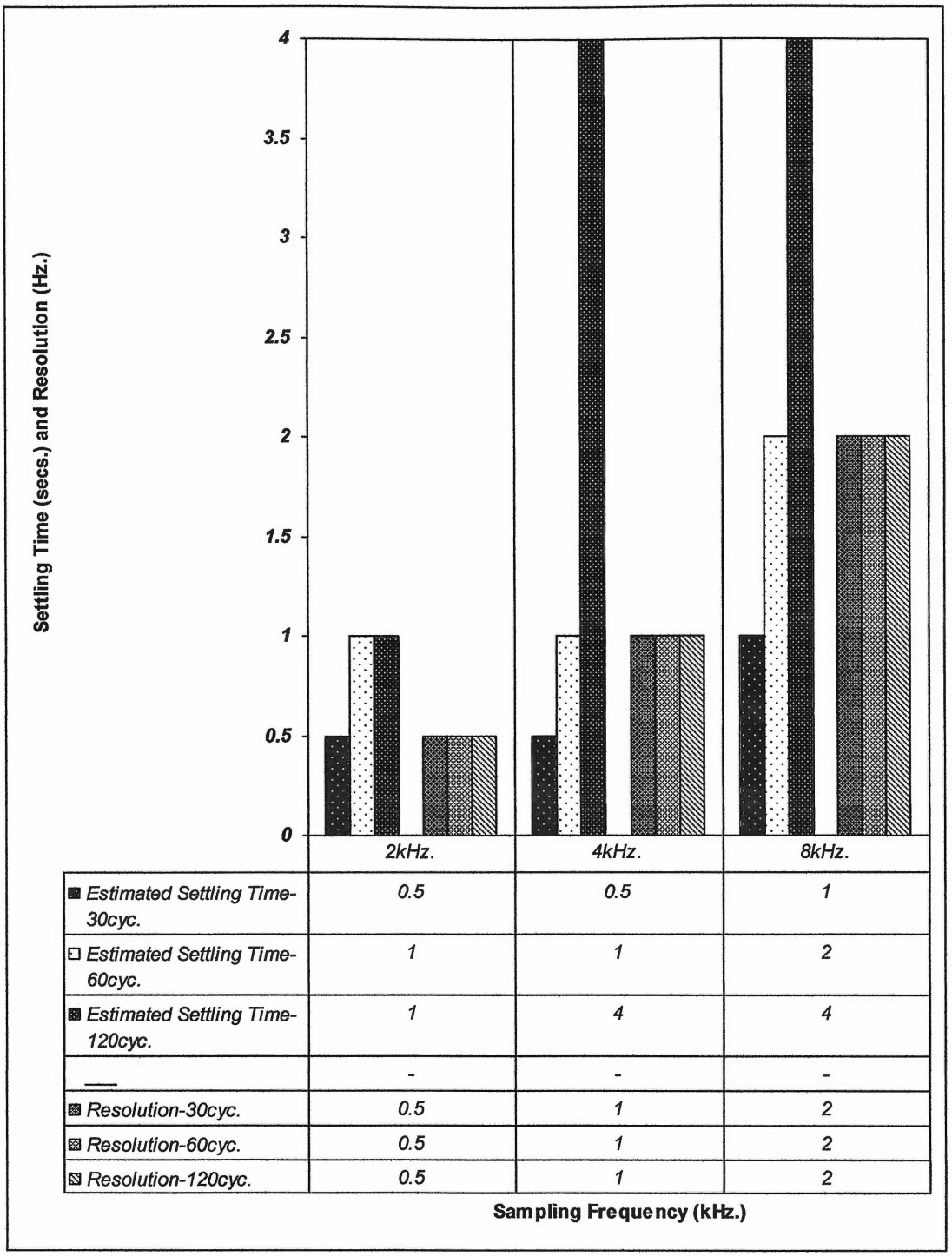

	2kHz.	4kHz.	8kHz.
Estimated Settling Time-30cyc.	0.5	0.5	1
Estimated Settling Time-60cyc.	1	1	2
Estimated Settling Time-120cyc.	1	4	4
___	-	-	-
Resolution-30cyc.	0.5	1	2
Resolution-60cyc.	0.5	1	2
Resolution-120cyc.	0.5	1	2

Figure 5.21: On-line results and plots of settling-time in seconds and resolution in Hz. for 30, 60 and 120 cycles of current data at sampling frequencies of 2, 4, and 8 kHz. – Adaptive Spectrogram, term = 2 and window length = 500.

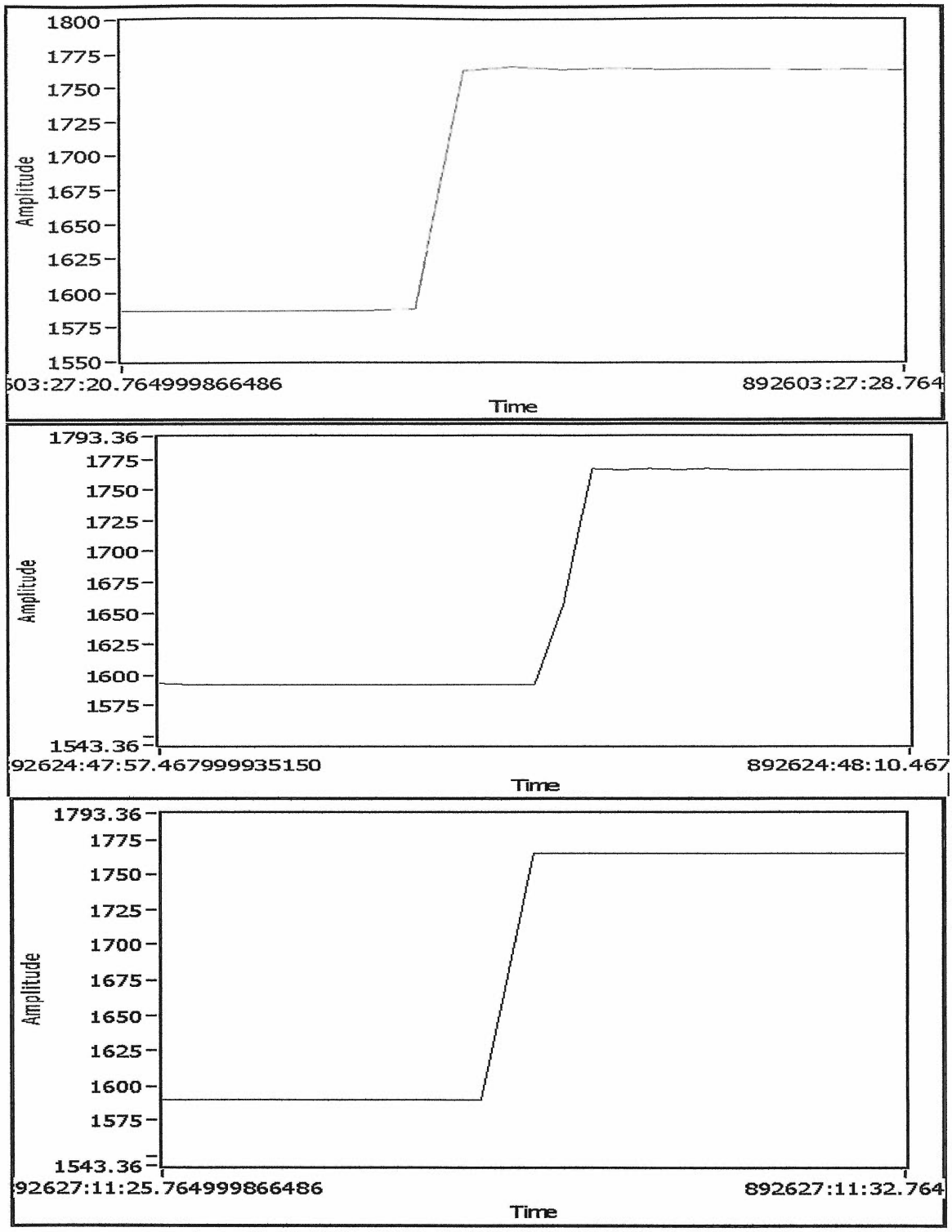

Figure 5.22: Settling-Time response for sudden rise in speed (rpm) from full load to no-load: MP, PCAR, and Covariance methods (top to bottom), 30 cycles data at 2 kHz sampling frequency.

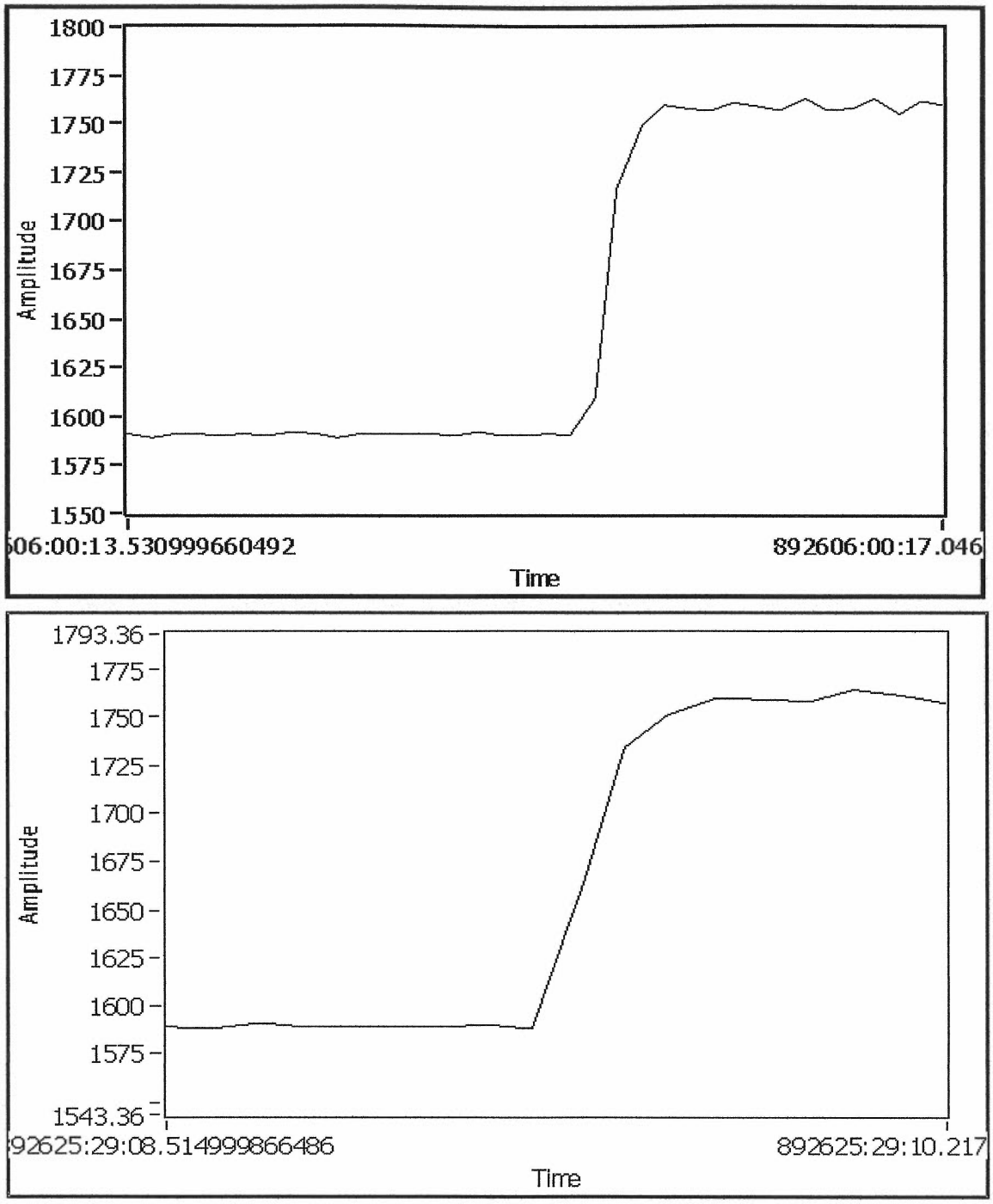

Figure 5.23: Settling-Time response for sudden rise in speed from full-load to no-load: MP and PCAR methods (top to bottom), 6 cycles data at 2 kHz sampling frequency.

5.3 Discussion

5.3.1 FFT Method

On-line test results were obtained for 30, 60 and 120 cycles of data at various sampling frequencies of 2, 4, and 8 kHz. The results are shown in Figure 5.12. As seen from the plot of Figure 5.12, there is a trade-off between resolution and settling-time as the number of data samples is increased at any given sampling frequency. The resolution of the FFT is limited by the relation, $\Delta f = \frac{Sampling\ Frequency}{Number\ \text{of Samples}}$. As seen in Figure 5.12, the settling-time increases but the resolution is improved with an increase in number of cycles for all of the sampling frequencies. FFT did not perform well for 15 cycles of data at any of the sampling frequencies. Accuracy did not vary much with an increase in the number of cycles or sampling frequencies and is limited to ±1 and ±2 rpm. The minimum value of the resolution achieved by FFT is 0.5 Hz at 120 cycles of data with a settling-time of about 2 seconds. The minimum value of resolution to compare the performances of spectral techniques was restricted to 0.5 Hz due to digits of precision setting in the software.

5.3.2 Model-Based Methods

Experimental results were obtained for 30, 15, 9 and 6 cycles of data for each of the sampling frequencies at 2, 4, and 8 kHz and results and plots are shown in figures 5.13 to 5.15. The Covariance method worked only for 30 cycles of data at a sampling frequency of 2 kHz and for 30 and 15 cycles of data at sampling frequencies of 4 kHz and 8 kHz. It failed for 9 and 6 cycles of data, therefore, results for them are not shown in the figures 5.13 to 5.15. As seen in figure 5.13, under these conditions the accuracy of the Covariance method is ±2 rpm with a relatively poor frequency resolution of 2 Hz for 30 cycles at sampling frequency of 2, 4 and 8 kHz and 4 Hz for 15 cycles at a sampling frequency of 4 and 8 kHz. This method is unstable for fewer numbers of data samples due to the fact that the Covariance method only uses forward or backward prediction to minimize the error between known data and predicted data. Since, the PCAR method uses both forward and backward prediction to minimize the error, thus it has more data

points for even less number of cycles to average out an error and in the case of the M.P. method it has good statistical properties and lower variance of the estimated parameters [28], therefore it is quite accurate to extract data from fewer number of cycles data. Due to these reasons, as seen in Figure 5.14, it was possible to obtain a resolution of 0.5 Hz for both PCAR and M.P. methods, accuracy within the limit of ±1 and ±2 rpm with a settling time of about less than half second under certain conditions as explained below. The M.P. method achieved a frequency resolution of 0.5 Hz, accuracy ±1 rpm and a settling time of about 0.25 seconds for 500 samples of data at a sampling frequency of 2 kHz. With the PCAR method it was possible to obtain the same frequency resolution and accuracy with a settling time of about 0.5 seconds for 500 samples data at a sampling frequency of 2 kHz. To achieve these results, the order number was selected to be 50 for both the M.P. and PCAR methods. The selection of order number for a given number of data-samples is critical for both PCAR and M.P. methods to achieve accuracy, in particular for a smaller number of data samples, at near-zero or light loads. Since, the optimal performance for this application was obtained at a sampling frequency of 2 kHz, further analysis is performed at this particular sampling frequency. As shown in Figure 5.24, selection of order number equal to ten for M.P. method leads to an averaged inaccuracy within 10 to15 rpm near light loads for 200 data samples. The accuracy is improved to the range of 5 to 7 rpm by increasing the order number to 50 and 130. In Figure 5.25, for 300 samples accuracy is within 5- 7 rpm for order number equal to ten which is improved to the range of 1 to 2 rpm by selecting an order number equal to 50. Similarly for 500 samples, as seen in Figure 5.26, accuracy is improved to ±1 rpm with an order number equal to 50. As the number of data samples decreases the order number has to be increased to improve accuracy. Figure 5.27 shows the effect of the number of data samples on the selection of an order number at near-zero or light loads. For 4000 and 2000 samples, the order number equal to two provides speed accuracy within ±1 rpm. By selecting an order number equal to 10 and 50 for 1000 and 500 samples respectively, accuracy is within ±1 rpm and for 300 samples, with an order number equal to 50, accuracy is within 2 to 3 rpm. At 200 data samples, even at higher order number, M.P. method tends to inaccuracies which are more predominant near zero or light loads. Figure 5.28 shows the oscillations for 200 samples at various load levels for an order number

equal to 10 (top) and for an order number equal to 50 (bottom) which are more predominant at light loads.

Similarly, for PCAR method Figures 5.29 to 5.31 shows the effect of order number on the speed accuracy near zero or light load levels for various data samples. As seen in figure 5.29, order number equal to 10 gives averaged accuracy within the range of 10 to 15 rpm for 200 data samples and is improved to the range of 5-7 rpm by increasing an order number to 50 and 100. For 300 samples, in Figure 5.30, by increasing an order number from 10 to 20 improves accuracy within the range of 2 to 3 rpm. For 1000 samples, in Figure 5.31, accuracy is within the range of 10 rpm for an order number 2, 8 to10 rpm for an order number 6, and 3 to 4 rpm and ±1 rpm for an order number equal to 10 and 20 respectively. Similar to M.P. method, for 200 data samples PCAR method tends to inaccuracies which are predominant at near zero or light loads. Figure 5.32 shows how the number of data samples influences the selection of an order number for PCAR method. As seen, order number is 50 for 200, 300, and 500 samples and 10 for 1000, 2000 and 4000 samples. It is seen from Figure 5.31, by increasing the order number to 20, accuracy can be further improved for longer data-sets as compared to that of order number equal to 10. Figure 5.33 shows the oscillations for 200 data samples at order number 50. As seen from the figure, oscillations are more predominant at near zero or light loads. Based on the above analysis, an optimal value of an order number is selected and further comparison of Matrix-Pencil method is performed with FFT, Covariance and PCAR methods for 1000, 2000 and 4000 samples at a sampling frequency of 2 kHz. Figure 5.34 shows the results of the comparison. To obtain these results, an order number equal to 2 was selected for Matrix-Pencil method for 2000 and 4000 samples and 10 for 1000 samples. Similarly, based on the above analysis, order number equal to 20 was selected in the case of PCAR method for 1000, 2000 and 4000 samples. Figure 5.34 and Figure 5.35 shows the effect of data samples number on averaged accuracy (rpm) at near-zero and medium load for PCAR and MP method respectively. As seen in the figures, accuracy is 6 to 7 rpm at 200 data samples, 2 rpm at 300 data samples and is improved to 1 rpm for 500 and 1000 data samples, for both PCAR and MP method. Accuracy is within the range of 1 rpm at all the data samples at medium load for both PCAR and MP method. Figure 5.36 shows the effect of data samples number on settling-time for PCAR,

MP, Covariance and FFT methods. MP method performs better, in terms of settling time, as compared to PCAR method near longer data-sets.

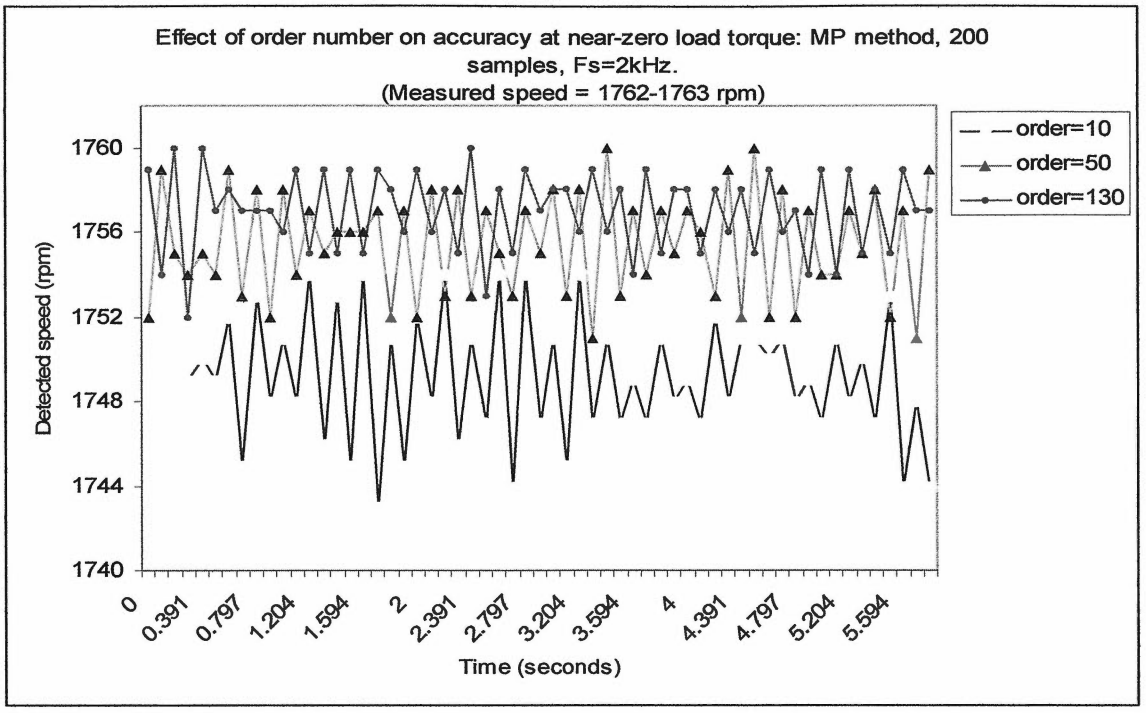

Figure 5.24: Effect of order number on accuracy at near-zero load torque: MP method, 200 samples, Fs = 2 kHz.

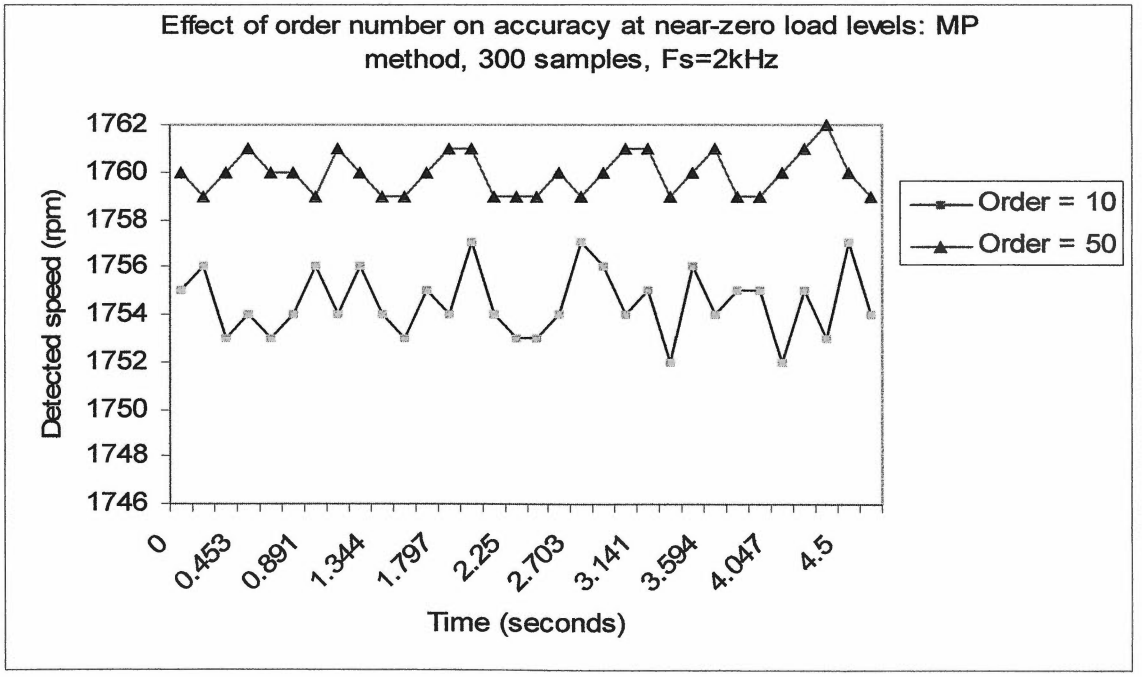

Figure 5.25: Effect of order number on accuracy at near-zero load torque: MP method, 300 samples, Fs = 2 kHz.

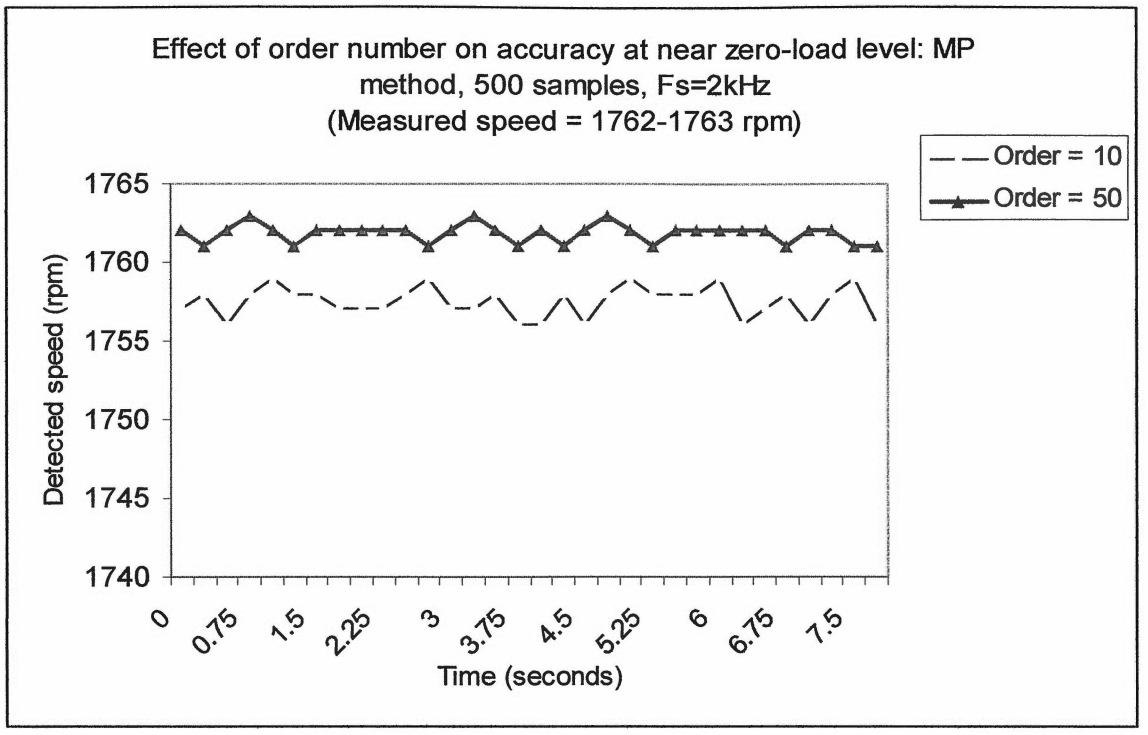

Figure 5.26: Effect of order number on accuracy at near-zero load torque: MP method, 500 samples, Fs = 2 kHz.

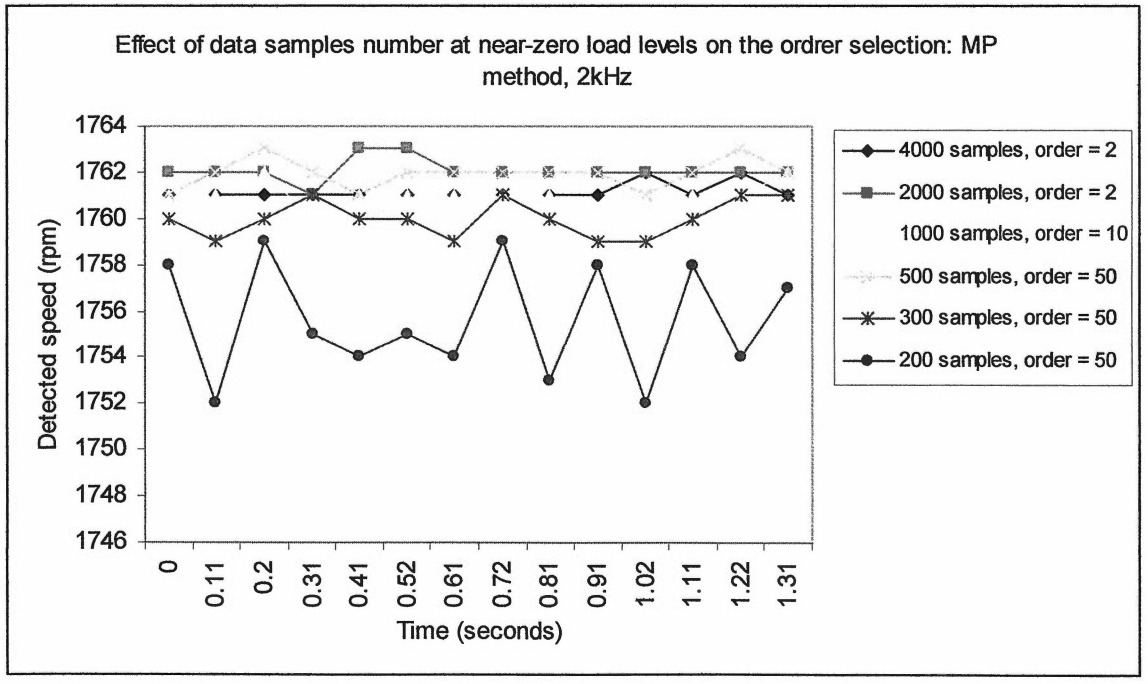

Figure 5.27: Effect of data samples at near-zero load torque on the order selection: MP method, Fs = 2 kHz (Measured speed = 1762-1763 rpm).

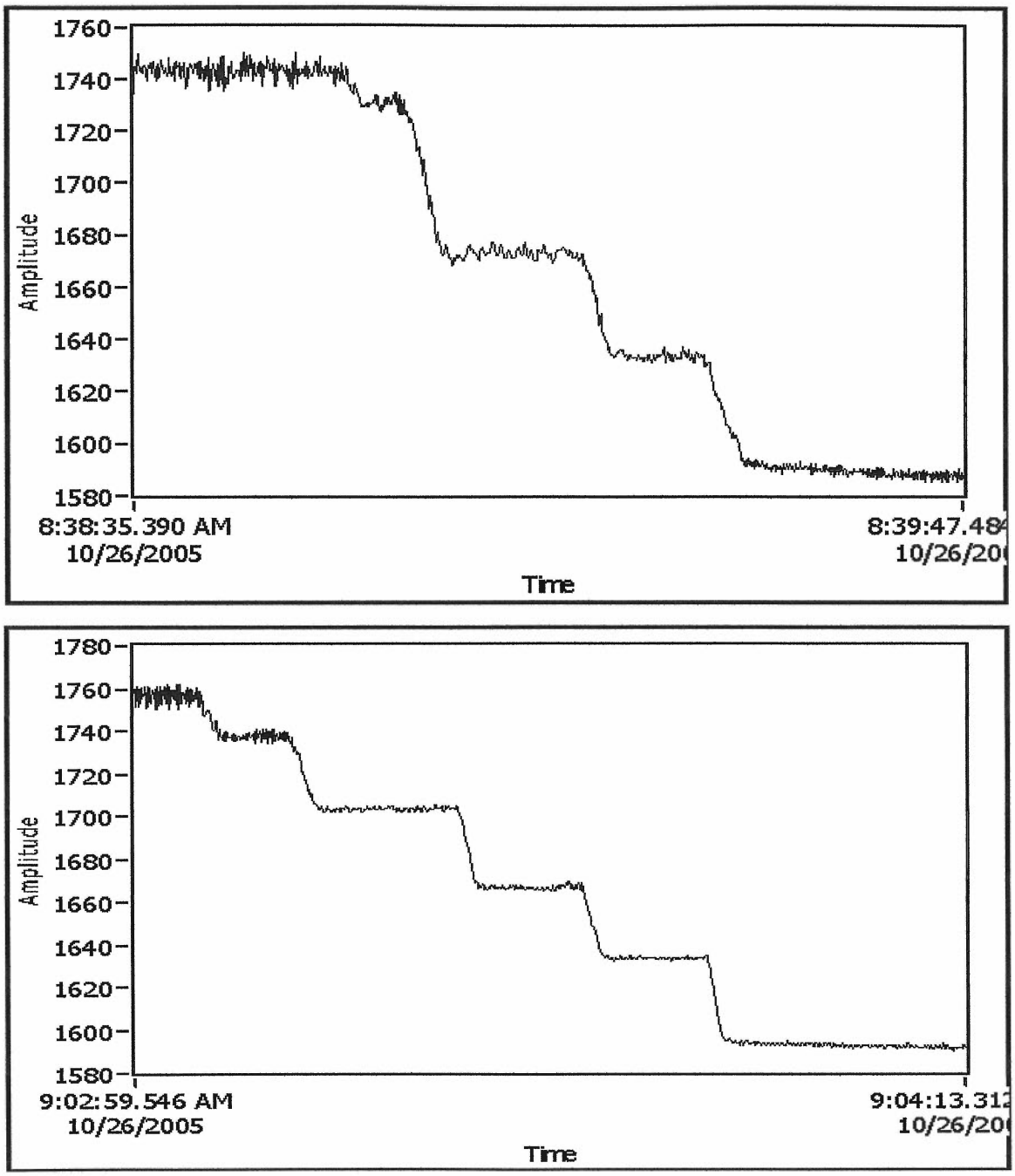

Figure 5.28: Oscillations at 200 data samples near light loads, Fs = 2 kHz: MP method, order number 10 and 50 (top to bottom).

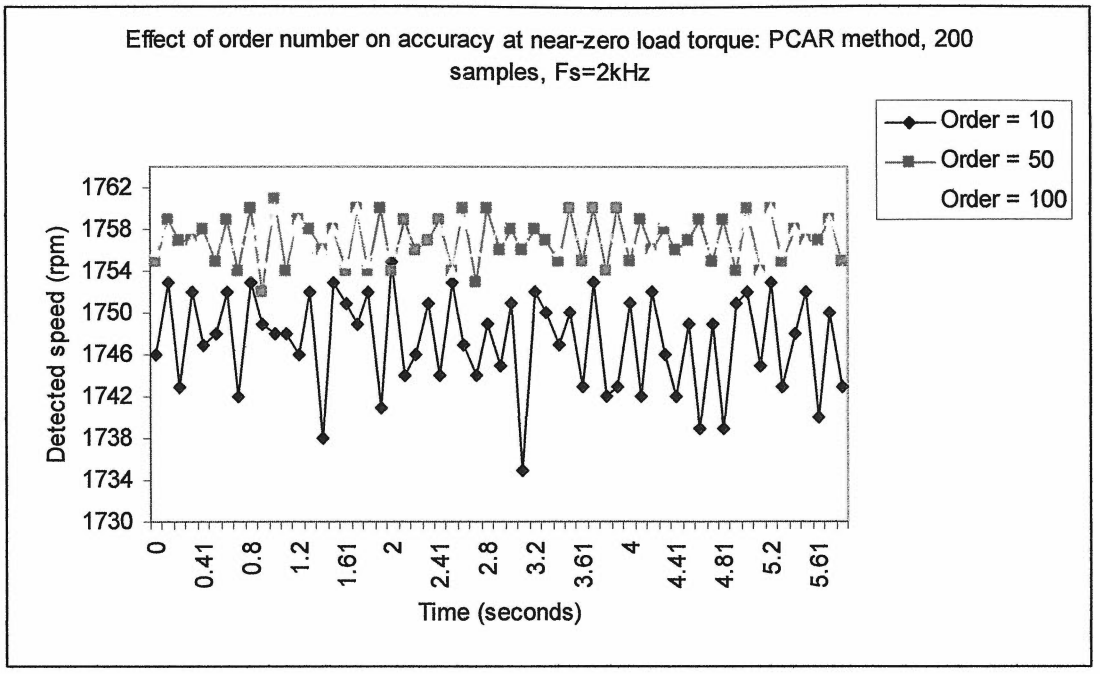

Figure 5.29: Effect of order number on accuracy at near-zero load torque: PCAR method, 200 samples, Fs = 2 kHz (Measured speed = 1762-1763 rpm).

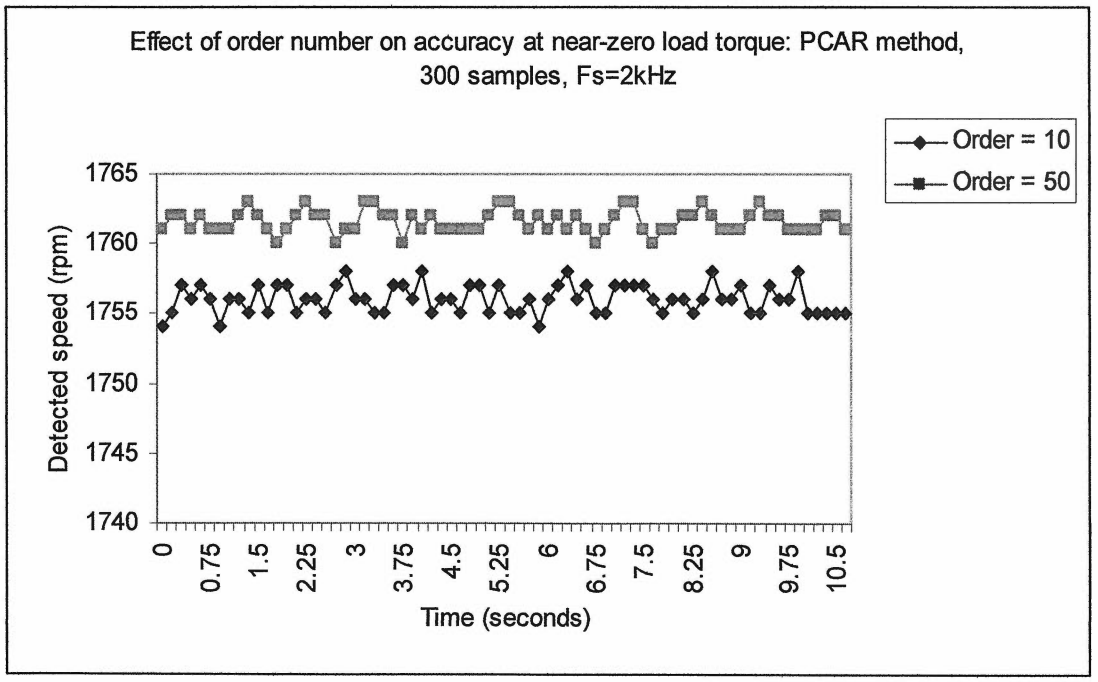

Figure 5.30: Effect of order number on accuracy at near-zero load torque: PCAR method, 300 samples, Fs = 2 kHz (Measured speed = 1762-1763 rpm).

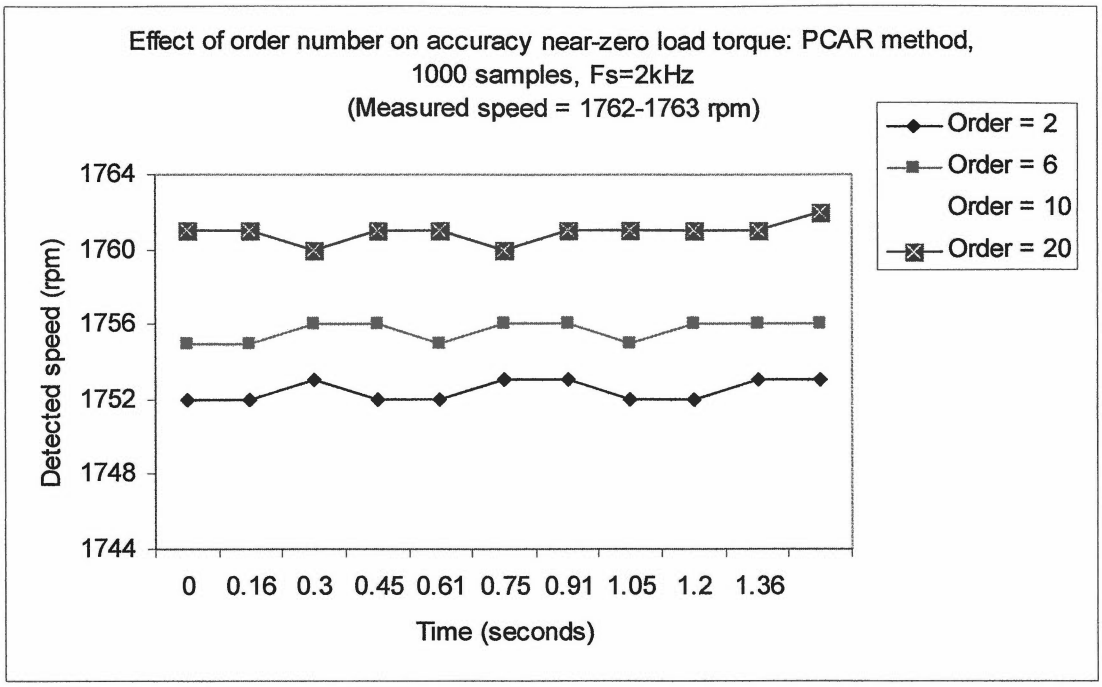

Figure 5.31: Effect of order number on accuracy at near-zero load torque: PCAR method, 1000 samples, Fs = 2 kHz (Measured speed = 1762-1763 rpm).

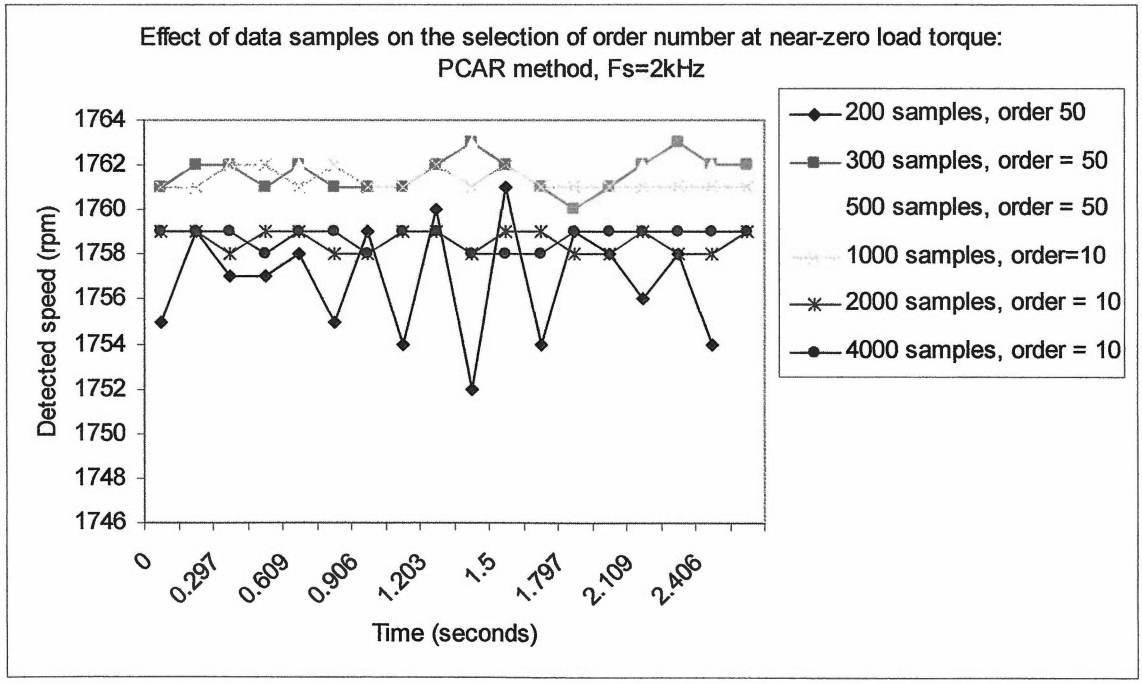

Figure 5.32: Effect of data samples number on the selection of order number at near-zero load torque: PCAR method, Fs = 2 kHz.

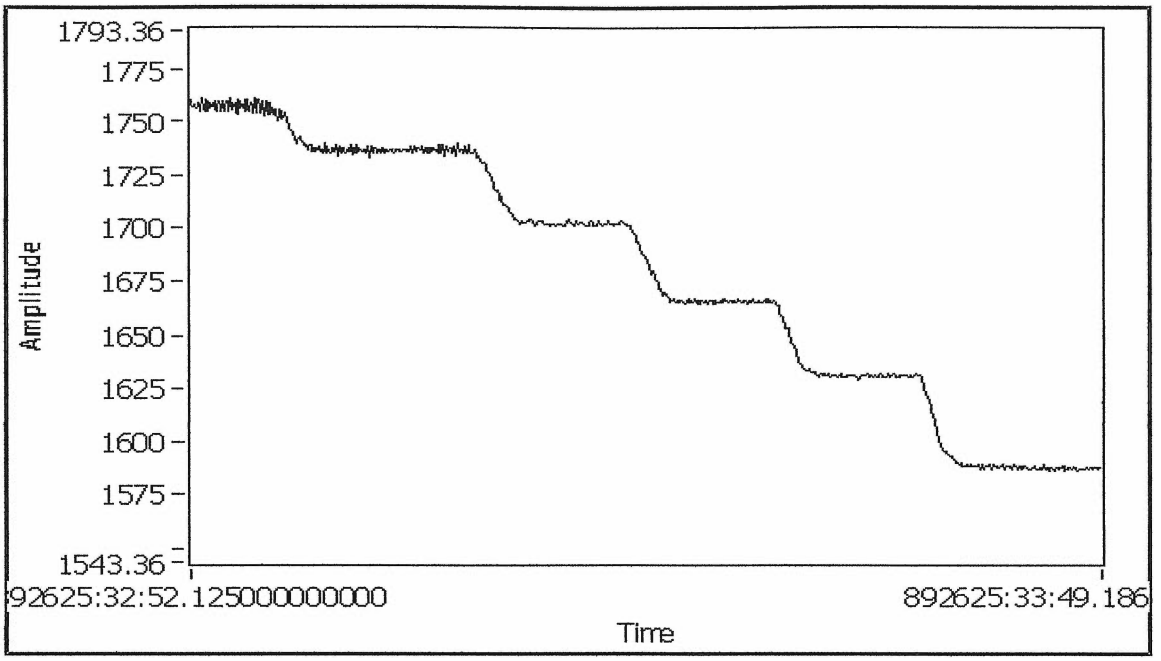

Figure 5.33: Oscillations at 200 data samples near light loads, Fs = 2 kHz: PCAR method, order number 50.

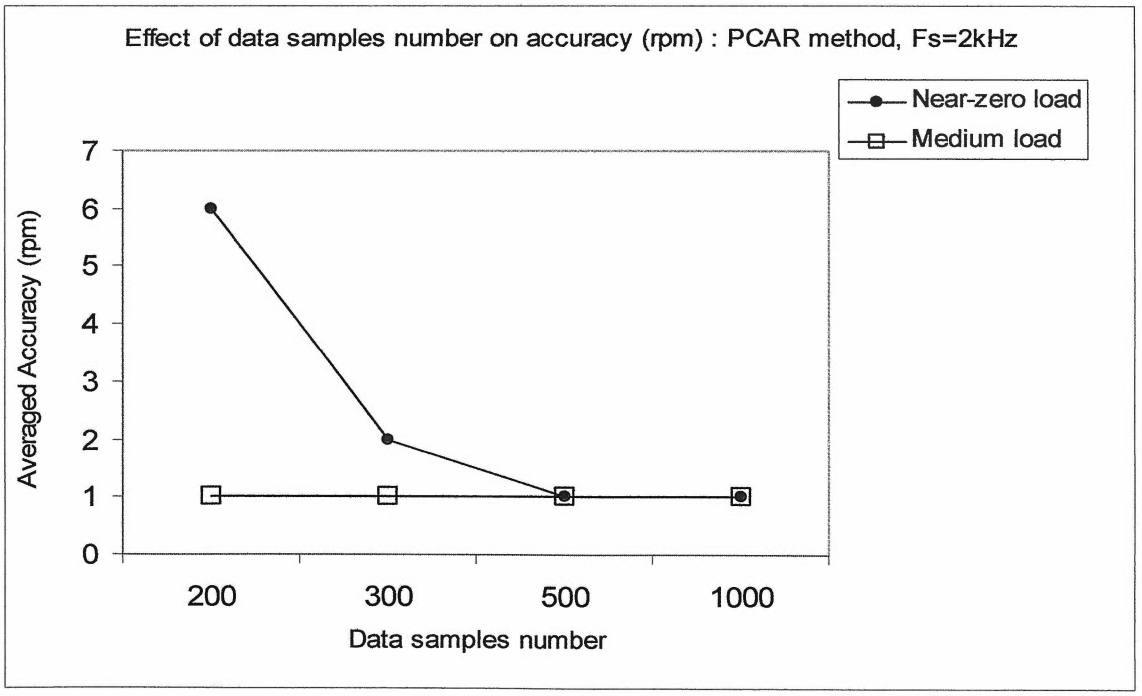

Figure 5.34: Effect of data samples number on accuracy (rpm) with regard to light and medium load: PCAR method, Fs = 2 kHz.

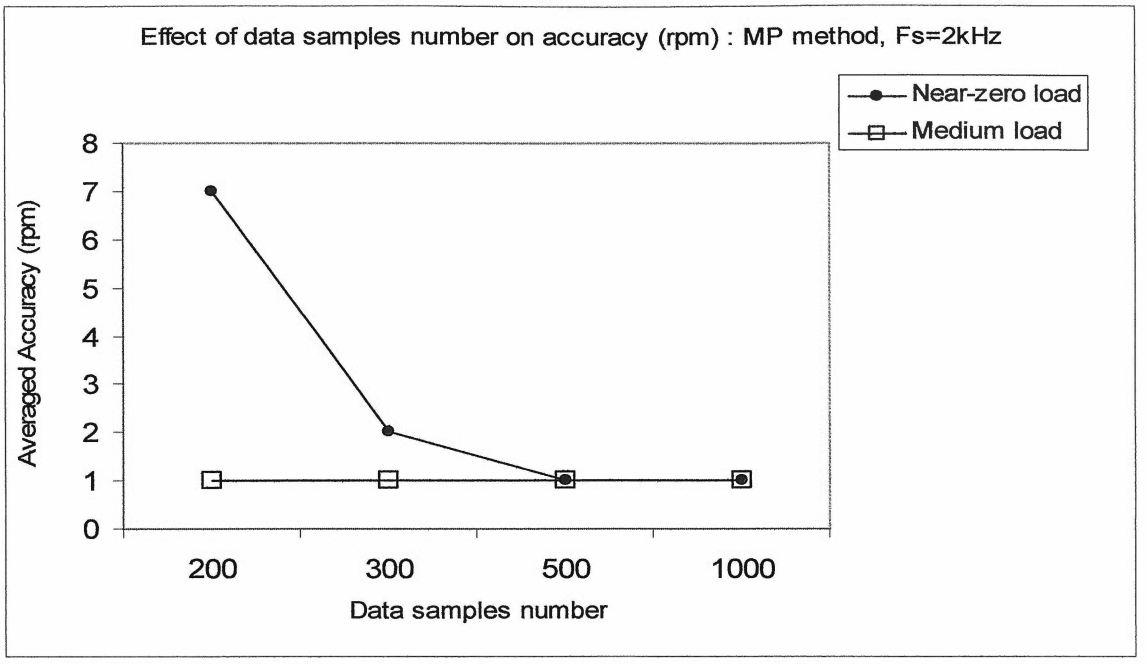

Figure 5.35: Effect of data samples number on accuracy (rpm) with regard to light and medium load: MP method, Fs = 2 kHz.

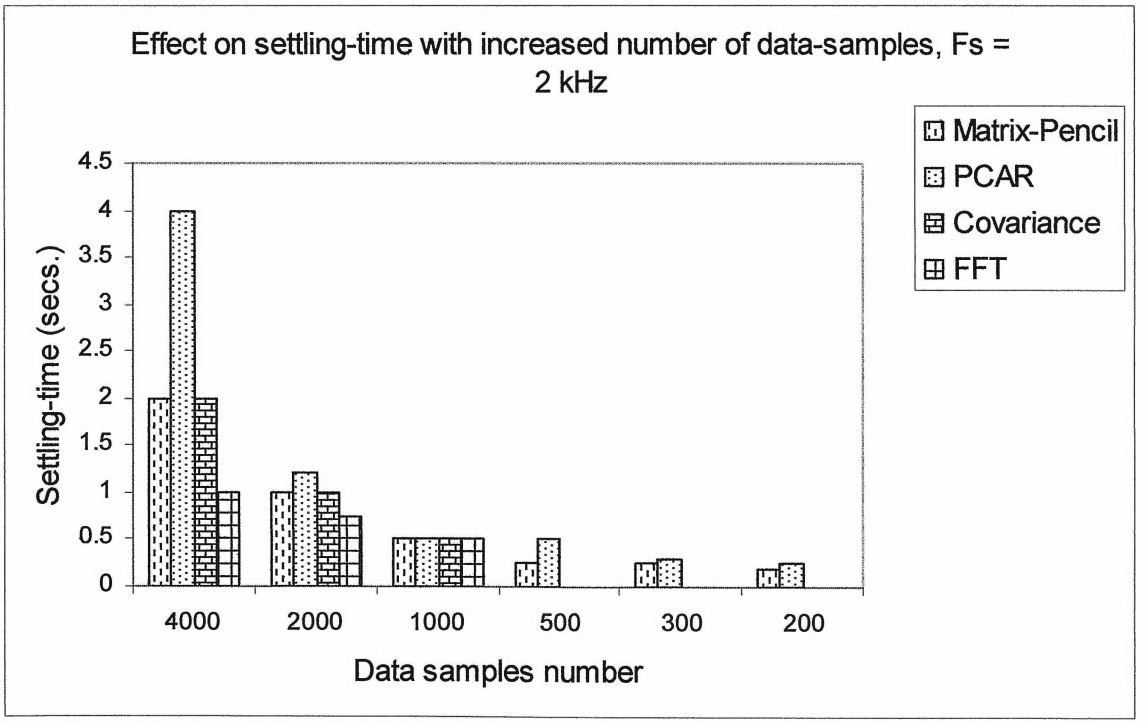

Figure 5.36: Effect of data samples number on settling time, Fs = 2 kHz: MP, PCAR, Covariance and FFT methods.

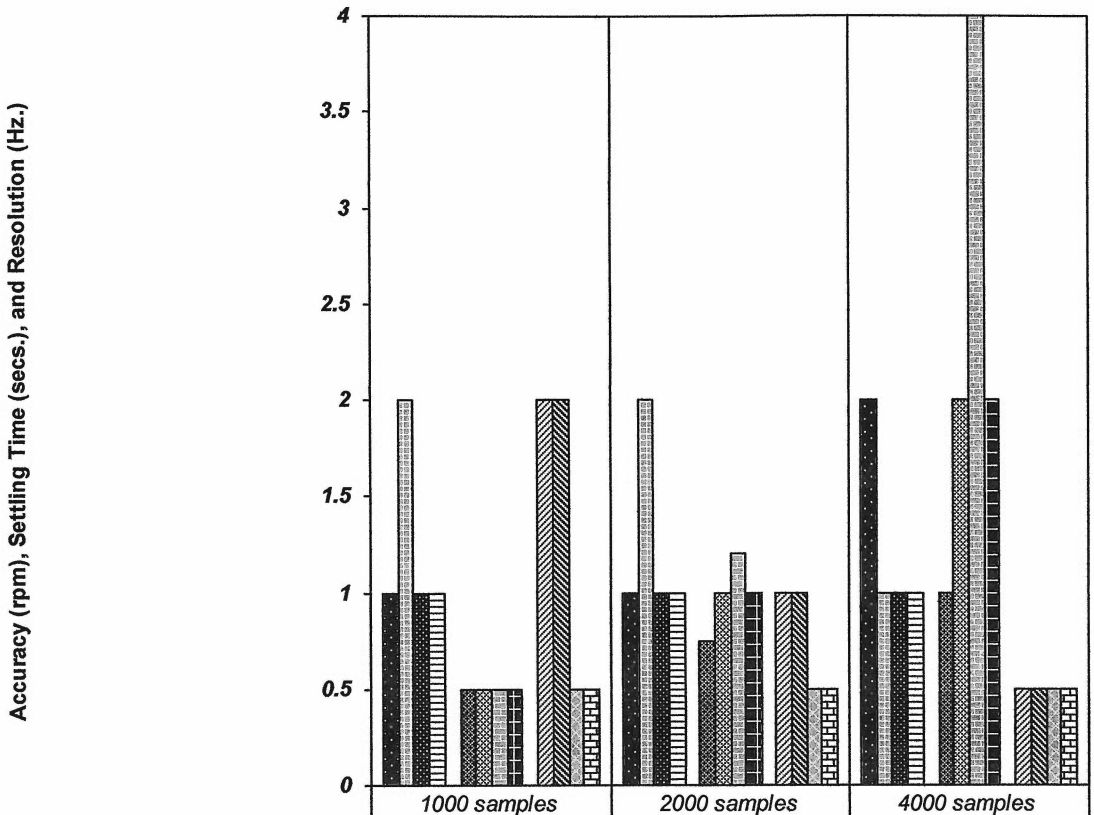

	1000 samples	2000 samples	4000 samples
Accuracy(rpm) - FFT	1	1	2
Accuracy(rpm) - Covariance	2	2	1
Accuracy(rpm) - PCAR	1	1	1
Accuracy(rpm) - MP	1	1	1
-	-	-	-
Settling Time(sec.) - FFT	0.5	0.75	1
Settling Time(sec.) - Cov.	0.5	1	2
Settling Time(sec.) - PCAR	0.5	1.2	4
Settling Time(sec) - MP	0.5	1	2
-	-	-	-
Resolution(Hz.) - FFT	2	1	0.5
Resolution(Hz.) - Covariance	2	1	0.5
Resolution(Hz.) - PCAR	0.5	0.5	0.5
Resolution(Hz) - MP	0.5	0.5	0.5

Number of data samples at a sampling frequency of 2 kHz

Figure 5.37: Comparison of performance for FFT, Covariance, PCAR and MP methods: 30, 60 and 120 cycles of data at Fs = 2 kHz.

5.3.3 JTFA Methods

The literature suggests that for the STFT method, there is a trade-off between time and frequency resolution depending upon the duration of the sliding analysis window. A wider window provides a narrow bandwidth and thus better frequency resolution. There is also a trade-off between the settling-time, resolution and the number of data samples. More data-samples result in higher settling-time. As seen in Figure 5.12, STFT with window length equal to 200 is able to provide a frequency resolution of 0.5 Hz for certain combinations of data cycles and sampling frequencies. At a sampling frequency of 2 kHz, a frequency resolution of 0.5 Hz is achieved for 60 and 120 cycles of data with an estimated settling time of about 1 and 1.5 seconds respectively. The settling time is reduced to about 0.5 seconds for 30 cycles of data but at the expense of frequency resolution which is equal to 1 Hz. By increasing the window length to 800, as shown in Figure 5.17, the frequency resolution is improved to 0.5 Hz for 15, 30, 60 and 120 cycles of data at sampling frequencies of 2 and 4 kHz. Settling-time results were the same as that of with a window length equal to 200. To overcome this window effect, the Gabor spectrogram method can be applied [37]. Gabor spectrogram as seen in Figure 5.5, suffers from cross-term effects. Higher order number increases the settling-time [37]. As seen in Figure 5.18, an estimated settling-time is 5 seconds at a sampling frequency of 2 kHz, for 120 cycles of data with a frequency resolution of 0.5 Hz. Settling-time is also increased as the number of data samples is increased. From Figure 5.19, by increasing the order to be equal to ten, settling time is increased to 1 and 2 minutes for 60 and 120 cycles of data at a sampling frequency of 2 kHz. For CSD with alpha equal to 1E-6, as seen in Figure 5.20, for 30 cycles of data at sampling frequency of 8 kHz settling-time is about 15 seconds respectively. As the number of data samples is increased, the settling-time is increased. In the case of Adaptive spectrogram, term =2 and window = 500, as seen in Figure 5.21, frequency resolution of 0.5 Hz with an estimated settling time within 1 and 2 seconds is achieved for 30, 60 and 120 cycles of data at a sampling frequency of 2 kHz. More experimental tests are needed to fully determine the performance of JTFA methods.

Chapter 6: Conclusions

6.1 Conclusions

In this research experiment, it has been shown that various spectral estimation techniques can be applied to detect speed of the F.H.P. induction motor, with minimum analog circuitry, from RSH using MCSA. Experiment was performed for off-line and on-line analysis of FFT, model-based and JTFA methods. A real-time application was developed in PC-based environment using LabView 7.1 software and its signal processing tool-set. A successful attempt has been made to acquire stator line current using high precision USB-2.0 data-acquisition module and thus avoiding any external analog circuitry required for signal-conditioning and anti-aliasing filtering.

This research work has demonstrated that novel methods such as the Matrix-Pencil and PCAR can be applied in real-time to detect speed of an induction motor. Performance of Matrix-Pencil and PCAR methods was compared with that of the FFT and Covariance methods. Advantages and limitations for both Matrix-Pencil and PCAR methods were outlined.The experimental results obtained indicate that, using both Matrix-Pencil and PCAR methods, it is possible to achieve a frequency resolution of 0.5 Hz, accuracy with in ±1 to ±2 rpm with a settling time of about 0.25 to 0.5 seconds for 500 data samples at a sampling frequency of 2 kHz. Matrix-Pencil performance was similar to that of PCAR method, in terms of accuracy and resolution and it performed better in terms of settling-time. Both MP and PCAR methods performed better than Covariance method in terms of accuracy and resolution. Covariance method was unstable for smaller data-sets.

The Matrix-Pencil method also performed well for longer data sets and a frequency resolution of 0.5 Hz was obtained for 1000 and 2000 samples, at a sampling frequency of 2 kHz, as compared to that of 2 Hz and 1 Hz with FFT method. Settling time for both Matrix-Pencil and FFT methods were about 0.5 second to 1 second with an averaged accuracy of ±1 rpm. The results indicate that, for 300 data samples, both PCAR and Matrix-Pencil method had inaccuracies at near zero or light loads and can be improved by selecting an optimal order number. For 200 data samples inaccuracies predominated at near-zero or light loads. Using PCAR or Matrix-Pencil methods for very small data-sets may lead to speed detection inaccuracies which are more predominant at near-zero or

light loads. Selecting an optimal order number, to achieve desired accuracy, for any given number of data samples is critical for both PCAR and MP methods. There are trade-offs between data samples number, order number and accuracy. These trade-offs are more predominant for smaller data-sets at near-zero or light loads. Table 6.1 outlines the optimal performance obtained, under certain conditions, for Matrix-Pencil, PCAR, Covariance and FFT methods.

Table 6.1: Optimal performance of spectral estimation methods, in terms of accuracy, resolution and settling-time.

Methods	Resolution (Hz.)	Settling-Time (Secs.)	Accuracy (rpm)	Sampling Frequency (kHz.)	Number of Data-Samples.
FFT	0.5	2	±1	2	4000
PCAR (order = 50)	0.5	0.5	±1	2	500
M.P. (order = 50)	0.5	0.25	±1	2	500
Covariance	2	0.5	±1	2	1000

This research work extended the existing knowledgebase in this field with significant contributions as outlined below:

a. Real-time performance analysis of novel signal processing methods including Matrix-Pencil and Principle component auto-regressive algorithms, in terms of accuracy, resolution and dynamic behavior under changing load conditions with regard to different data-record lengths at different sampling frequencies, for sensor-less speed detection of an induction motor using minimum analog circuitry. Strengths and limitations of both methods are outlined. While these algorithms have been used in other areas the author is not aware of them being used in motor applications.

b. PC-based application development, using LabView 7.1 software and its signal processing tool-set, that allows investigating the steady-state and dynamic performance of various spectral estimation techniques in one application, in real-time.

c. This research work contributes in assisting the drive and CBM tool designer formulate important rules for optimizing data-acquisition and signal processing parameters in MCSA applications.

6.2 Implications of an algorithm

The present speed detection algorithm is implemented and tested on the F.H.P. induction motor operating under the following conditions:

I. Fundamental frequency is fixed at 60 Hz.

II. Motor is operating under rated slip range of $0 < s < 14\%$ and is supplied from a three-phase source without using an inverter.

This algorithm operates satisfactorily under the above conditions. By setting threshold levels, the same algorithm can be used to detect motor internal faults such as broken rotor bars and to determine load conditions. It requires only one input i.e. digitized stator line current and a priori knowledge of the number of rotor slots. Presently, fundamental frequency and filter cut-off frequencies are not auto-tunable. Accuracy is not affected under unloaded or light load conditions under certain conditions. In this particular experimental set-up, RSH component does not coincide with any harmonic component. While using certain drives or an inverter it may coincide depending upon the switching strategy of an inverter. In a speed control application such as vector control, the minimum frequency of an inverter can be as low as 2 Hz. This algorithm is yet to be tested for its ability to operate at low frequencies and thus to track small slip changes with a narrow bandwidth or in the presence of narrowband noise.

6.3 Future Work

The present research work can be further extended to test the performance of the applied spectral estimation methods across a wide range of inverter frequencies. This algorithm can be modified to determine machine specific parameters and auto tuning of filter cut-off frequencies so that it can be applied to virtually any induction motor. Further, this application can be extended, with necessary modifications, to be used as an on-line sensor-less noninvasive CBM tool to diagnose motor faults.

Reference List

[1] Agamloh E., Wallace A., Jouanne A.V., Kenneth J. A., and Rooks J.A., "Assessment of Non-Intrusive Motor Efficiency Estimators," 0-7803-8282-X/04, IEEE 2004, pp. 64-69.

[2] Ye Z., Wu B., and Sadeghian A., "Current Signature Analysis of Induction Motor Mechanical Faults by Wavelet Packet Decomposition," IEEE Transactions on Industrial Electronics, Vol. 50, No. 6, December 2003, pp. 1217-1228.

[3] Grantham C. and McKinnon D.J., "Rapid Parameter Determination for Induction Motor Analysis and Control," IEEE Transactions on Industry Applications, Vol. 39, No. 4, July/August 2003, pp. 1014-1020.

[4] Durocher D.B., Feldmeier G.R., "Future Control Technologies in Motor Diagnostics and System Wellness," 0-7803-7931-4/03, IEEE 2003, pp. 98-106.

[5] Micheletti R., "Sensorless Speed Measurement of Induction Motors," IEEE 2003, WISP 2003, Budapest, Hungary, 4-6 September, 2003, pp. 67-72.

[6] Qin S., Ji Y., and Tang B., "The Design For Signal Processing System of Time-Frequency Analysis," SICE 2002 Aug. 5-7, 2002, Osaka, pp. 2489-2492.

[7] Nutt K., Tarbouchi M., McGaughey D. and Chikhani A., "Current harmonic detection for induction motor speed sensorless control using fast orthogonal search," Proceedings of the American Control Conference, Anchorage, AK May 8-10, 2002.

[8]Aller J.M., Habetler T.G., Harley R.G., Tallam R.M. and Lee S.B., "Sensorless Speed Measurement of AC Machines Using Analytic Wavelet Transform," IEEE Transactions on Industry Applications, Vol. 38, No. 5, September/October 2002, pp. 1344-1350.

[9] Ye Z., Wu B., and Sadeghian A.R., "Signature Analysis of Induction Motor Mechanical Faults by Wavelet Packet Decomposition," 0-7803-6618-2/01, IEEE 2001, pp. 1022-1029.

[10] Thomson W.T. and Fenger M., "Current Signature Analysis to Detect Induction Motor Faults," IEEE Industry Applications Magazine, July/August 2001, pp. 26-34.

[11] Sin M.L., Soong W.L. and Ertugrul N., "Induction Machine On-Line Condition Monitoring and Fault Diagnosis – A Survey," University of Adelaide, Singapore.

[12] Benbouzid M.E., "A Review of Induction Motors Signature Analysis as a Medium for Faults Detection," IEEE Transactions on Industrial Electronics, Vol. 47, No. 5, October 2000, pp. 984-93.

[13] A. Ben Sasi, B. Payne, A. York, F. Gu, A. Ball, "Condition Monitoring of Electric Motors Using Instantaneous Angular Speed," Maintenance Engineering Research Group, The University of Manchester, 2000.

[14] Bašic'I., "Automated Testing of Basic Characteristics of Induction Motors," Faculty of Electrical Engineering and Computing, Unska bb, Zagreb, 2000.

[15] Djurovic I., and Stankovic L., "A Virtual Instrument for Time-Frequency Analysis," IEEE Transactions on Instrumentation and Measurement, Vol. 48, No. 6, December 1999, pp. 1086-1092.

[16] Qian S. and Chen D., "Understanding the Nature of Signals Whose Power Spectrum Change with Time-Joint Analysis," IEEE Signal Processing Magazine, March 1999, pp. 52-67.

[17] Marple S.L. Jr., "Time-Frequency Signal Analysis: Issues and Alternative Methods, 0-7803-5073-1/98, IEEE 1998, pp. 329-332.

[18] Restrepo J.A., Gimenez M.I., Guzman V.M., Aller J.M. and Bueno A., "TF-Representation Kernel Selection for Sensorless Speed Measurement of AC Machines," Power Electronics and Variable Speed Drives, 21-23 September 1998, Conference Publication No. 456, IEE 1998, pp. 324-328.

[19] Thomson W.T., "A Review of On-Line Condition Monitoring Techniques for Three-Phase Squirrel-Cage Induction Motors-Past, Present and Future," The Robert Gordon University, Schoolhill, Aberdeen, Scotland.

[20] Filippetti F., Pirani S., Tommasini L., Franceschini G., "LabView Implementation of Speed Detection for Mains-Fed Motors Using Motor Current Signature Analysis," IEEE Power Engineering Review, June 1998, pp. 47-48.

[21] Kliman G.B., Premerlani W.J., Yazici B., Koegl R.A., Mazereeuw J., "Senorless Online Motor Diagnostics," ISSN 0895-0156/97, IEEE 1997, pp. 39-43.

[22] Nash J.N., "Direct Torque Control, Induction Motor Vector Control without an Encoder," IEEE Transactions on Industry Applications," Vol. 33, No. 2, March/April 1997, pp. 333-341.

[23] Hurst K.D. and Habetler T.G., "A Comparison of Spectrum Estimation Techniques for Sensorless Speed Detection in Induction Machines," IEEE Transactions on Industry Applications, Vol. 33, No. 4, July/August 1997, pp. 898-905.

[24] Gray G.G., Martiny W.J., "Efficiency Testing of Medium Induction Motors A Comment on IEEE Std 112-1991," IEEE Transactions on Energy Conversion, Vol. 11, No. 3, September 1996, pp. 495-499.

[25] Pillay P., Xu Z., "Motor Current Signature Analysis," 0-7803-3544-9/96, IEEE 1996, pp. 587-594.

[26] Blasco-Gimenez R., Asher G.M., Sumner M., Bradley K.J., "Performance of FFT-Rotor Slot Harmonic Speed Detector for Sensorless Induction Motor Drives," IEE Proc.-Electr. Power Appl., Vol. 143, No. 3, May 1996, pp. 258-268.

[27] Hurst K.D., Habetler T.G., "Sensorless Speed Measurement Using Current Harmonic Spectral Estimation in Induction Machine Drives," IEEE Transactions on Power Electronics, Vol. 11, No. 1, January 1996, pp. 66-73.

[28] Sarkar T.K. and Pereira O., "Using the Matrix Pencil Method to Estimate the Parameters of a Sum of Complex Exponentials," IEEE Antennas and Propagation Magazine, Vol. 37, No. 1, February 1995, pp. 48-55.

[29] Hurst K.D., Habetler T.G., Griva G., Profumo F., "Speed Sensorless Field-Oriented Control of Induction Machines Using Current Harmonic Spectral Estimation," 0-7803-1993-1/94, IEEE 1994, pp. 601-607.

[30] Beguenane R., Ghyseleen C., Schoorens H., "A Proposed Induction Motor Speed Sensor without Contact Slots Harmonics. Application to Rotoric Time Constant Identification," Power Electronics and Variable-Speed Drives, 26-28 October 1994, Conference Publication No. 399, IEE. 1994, pp. 90-95.

[31] Blasco R., Sumner M. and Asher G.M., "Speed Measurement of Inverter Fed Induction Motors Using the FFT and the Rotor Slot Harmonics," Power Electronics and Variable-Speed Drives, 26-28 October 1994, Conference Publication No. 399, IEE 1994, pp. 470-475.

[32] Ferrah A., Bradley K.J., and Asher G.M., "Application of the FFT to the Speed Measurement of Inverter Fed Induction Motors," 0-7803-0640-6/92, IEEE 1992, pp. 647-652.

[33] Ferrah A., Bradley K.G., and Asher G.M., "Sensorless Speed Detection of Inverter Fed Induction Motors Using Rotor Slot Harmonics and Fast Fourier Transform," 0-7803-0695-3/92, IEEE 1992, pp. 279-286.

[34] Ferrah A., Bradley K.J., and Asher G.M., "An FFT-Based Novel Approach to Noninvasive Speed Measurement in Induction Motor Drives," IEEE Transactions on Instrumentation and Measurement, Vol. 41, No. 6, December 1992, pp. 797-802.

[35] Ferrah A., Bradley K.J., Asher G.M., and Woolfson M.S., "An Investigation into Speed Measurement of Induction Motor Drives Using Rotor Slot Harmonics and Spectral Estimation Techniques," University of Nottingham, UK, IEEE 1992, pp. 185-189.

[36] LabView 7 Express User Manual. (April 2003). Ireland, National Instruments Corporation.

[37] LabView and LabWindows/CVI Signal Processing Toolset User Manual. (December 2002). Ireland, National Instruments Corporation.

[38] Operating Instructions USB-9215. (July 2004). Ireland, National Instruments Corporation.

[39] Data Acquisition Fundamentals-Application Note 007. (April 2002). Ireland, National Instruments Corporation.

[40] Signal Conditioning Fundamentals for Computer-Based Measurement Systems-Application Note 048. (March 2001). Ireland, National Instruments Corporation.

[41] The Fundamentals of FFT-Based Signal Analysis and Measurement-Application Note 041. (July 2000). Ireland, National Instruments Corporation.

[42] Data Acquisition Specifications – A Glossary-Application Note 092. (February 1997). Ireland, National Instruments Corporation.

[43] Fast Fourier Transforms and Power Spectra in LabView-Application Note 040. (February 1993). Ireland, National Instruments Corporation.

[44] Boldea I. and Nasar S.A., Induction Machines Handbook. (2002). Florida, CRC Press LLC.

[45] Vas P., Parameter Estimation, Condition Monitoring, and Diagnosis of Electrical Machines-Monographs in Electrical and Electronic Engineering–27. (2001). New York, Oxford University Press Inc.

[46] Sarma, M.S., Electric Machines, Steady-State Theory and Dynamic Performance, Second Edition. (1996). Boston, PWS Publishing Company.

[47] Lyons R.G., Understanding Digital Signal Processing. (2001). New Jersey, A Prentice Hall PTR Publication.

[48] Semmlow J., Biosignal and Biomedical Image Processing. (2004). Florida, CRC Press LLC.